Three-Dimensional Design Methods for Turbomachinery Applications

G. N. Shrinivas

St. Catherine's College

Trinity 1996

Thesis submitted for the degree of
Doctor of Philosophy
at the
University of Oxford

Oxford University Computing Laboratory

Numerical Analysis Group

Abstract

This thesis studies the application of sensitivity analysis and optimization methods to the design of turbomachinery components. Basic design issues and a survey of current design trends are presented. The redesign of outlet guide vanes (OGV's) in an aircraft high bypass turbofan engine is attempted. The redesign is necessitated by the interaction of the pylon induced static pressure field with the OGV's and the fan, leading to reduced OGV efficiency and shortened fan life. The concept of cyclically varying camber is used to redesign the OGV row to achieve suppression of the downstream disturbance in the domain upstream of the OGV row. The redesign is performed using (a) a linear perturbation CFD analysis and (b) a minimisation of the pressure mismatch integral by using a Newton method. In method (a) the sensitivity of the upstream flow field to changes in blade geometry is acquired from the linear perturbation CFD analysis, while in method (b) it is calculated by perturbing the blade geometry and differencing the resulting flow fields. Method (a) leads to a reduction in the pylon induced pressure variation at the fan by more than 70% while method (b) achieves upto 86%. An OGV row with only 3 different blade shapes is designed using the above method and is found to suppress the pressure perturbation by more than 73%. Results from these calculations are presented and discussed. The quasi-Newton design method is also used to redesign a three dimensional OGV row and achieves considerable reduction of upstream pressure variation. A concluding discussion summarises the experiences and suggests possible avenues for further work.

Acknowledgements

I would like to thank my supervisor Dr. Mike Giles, who has been a constant source of guidance, inspiration and encouragement through out the course of this project. I would also like to thank Dr Paul Crumpton for the assistance/collaboration, coffee breaks and reminding me (regularly) that I should submit my thesis.

I would also like to thank Rolls-Royce Plc for their support for this project. Drs. P. Stow, A. Suddhoo (ex of RR), R. Bailey and A. Parry have been most helpful and have provided considerable insight into industrial methods and preferences. The lunches at St Hugh's were great.

Acknowledgements are also due to:

- Dr Nick Birkett and Dr Dave Burgess for the words of encouragement, discussions and being brilliant office mates.
- Pierre Moinier and Matt Leatham – "The New Generation" for the coffee breaks, great discussions and of course networked "bz".
- Antoine for bz, java, coffee breaks and being my french censor (with Pierre as a tutor, one needs a censor!).
- Bette for patiently listening to my whining and remembering to get great cakes for us starved souls!
- Anne, Ian, Joe, JohnW, Lyon, PaulH, Niles, Mike and others in the lab.
- Dr Dr Abbey John for words of wisdom(?) and lunches at BNC!
- Tunku Don, Jules, Scotty, Ramesh, Johannes, Peter Koo, David Yung, Nils, Carsten, Nihar, Saurabh and many others for being great company and generally tolerating me!
- IIT-Bombay, OUCL and St Catherine's College.
- guru KS, GRS, AKN, JD, MaheshV, Raka, H9 junta and many others from IIT-B.
- Raj and Garuth.

My parents and sister for everything! Where would I be without you?

G. N. Shrinivas

To

Amma, Anna and Akka

Contents

List of Figures

Chapter 1

Introduction

Advances in Computational Fluid Dynamics (CFD) have enabled accurate prediction of flow fields about complex three dimensional geometries in the order of minutes rather than days or months. This can be attributed to (a) advances in computing technology and (b) improved numerical techniques. The level of approximation of the physical process is a compromise between the accuracy of the mathematical model and its computational cost. High computing costs during the early years of numerical methods necessitated the use of simple flow models (neglecting or approximating several complex flow features). Potential flow models such as *panel methods* were used to make fairly accurate predictions about incompressible inviscid flow fields. As a result of low computer requirements, panel methods are still in use as a preliminary design tool. The advances in silicon technology and rapid increase in CPU & memory speeds have cut costs of computing so sharply that it is no more the primary factor in the selection of a mathematical model. Numerical solutions to compressible flows have been obtained by solving (a) the inviscid Euler equations and (b) the viscous Navier-Stokes equations. At Reynolds numbers encountered in flight, onset of turbulence is inevitable thus viscous flow solutions, for practical applications, must include turbulence modeling. The scale of turbulent structures is much smaller than the overall configuration, thus ab initio calculations are not feasible with current computing resources. Turbulence models involve statistical averaging of turbulence. This affects the overall accuracy of any viscous method presently available, so that accurate drag prediction is still not possible in most cases. Many years ago Prandtl showed that viscous effects dominate in a narrow region close to the body surface (the boundary layer) while the flow beyond this layer is essentially inviscid (in the absence of separation). Thus, solutions of the inviscid (Euler)

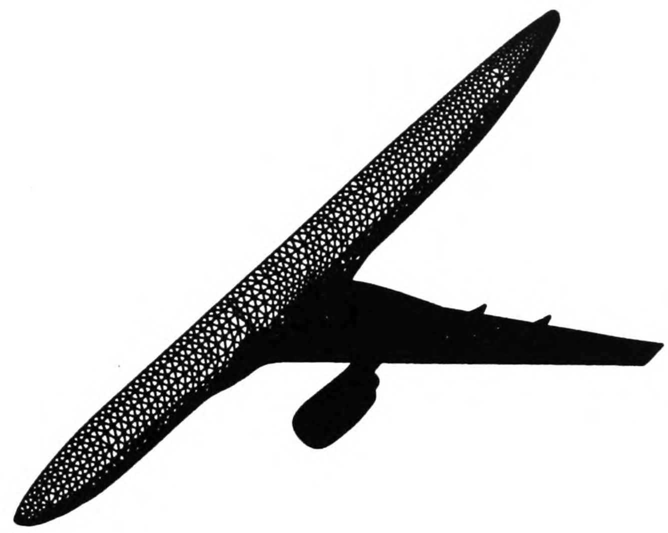

Figure 1.1: A wing-body-engine configuration.

equations can be used to obtain an understanding of important inviscid flow features.

Several factors have contributed to the advancement of CFD, the key factors include:

Computing Technology Advances in CFD are tied to the quality and cost of computing resources available. Key issues are:

- Tremendous increase in price performance of computers. Computer performance that would cost the order of \$100M in 1960 cost only about \$100 in 1993! Faster microprocessors, faster RAM and reliable hard disks have contributed to better price performance. Availability of cheap and powerful workstations (and PCs) has made CFD research feasible to many more research groups.
- Use of parallel processing! Interest in parallel processing has spawned research aimed at creating "virtual" parallel machine by linking several workstations using software directives embedded in user programs. Libraries based on message passing (parallel virtual machine PVM) [20] MPI (message passing interface) [19] and bulk synchronous processing (BSP) [56] are freely available. The use of such portable libraries has made it possible to develop parallel software in an inexpensive workstation environment, a possibility that has been explored by many research groups. Relatively powerful

parallel computers can now be acquired on university computing budgets and has contributed to increased interest in parallel processing. In an attempt to hide the parallelisation aspects from the average CFD researcher, several research groups have developed libraries that perform parallelisation of standard CFD operations and act as an interface between the CFD code and PVM/BSP like libraries (ex: OPLUS [6]). CFD methods based on Euler equations have been applied to wide variety of problems [59], [37], [3], [55] and [50]. As a demonstration of the robustness of numerical methods and parallel computing when applied to large problems Crumpton [12] has solved the Euler equations for the flow past a wing-body-engine configuration (fig 1.1, pg 2) with 6M tetrahedra (1M nodes) in 6 hours (wall clock time) on an eight processor IBM SP1 (residual down by 5 orders of magnitude).

- Visualisation Technology. A considerable part of CFD time is spent in postprocessing, ie. in visualising the results. Advances in visualisation technology [27] has made it possible to interactively view data from CFD codes. Such methods aid the CFD programmer in debugging algorithms and computer programs. Visualisation methods such as Visual3 [36] provide the user with a suite of probes to study the flow field and its salient features (such as vortex interaction with downstream components etc). Such a perspective of the flow field is afforded only by CFD based visualisation techniques and is very hard to acquire using experimental methods (wind or water tunnels). With the advent of parallel processing, problem sizes have seen a quantum jump which has outshot the capabilities of all desktop graphics workstations thus necessitating a fresh approach to visualisation. Some developers have attempted the use of parallel processing concepts by distributing datasets among many computers and handling only a reduced set of information on the graphics frontend. One such distributed visualisation tool is pV3 [34] which is based on a client-server model. The client is a user written program with appropriate pV3 calls, the server is a pV3 executable provided with the library. The client can run on any machine while the server is executed on a graphics frontend. Due to the modularity of pV3 it is possible to regard a CFD code as the client (by embedding pV3 library calls at the end of each iteration) with negligible computational overheads. This feature can be used to monitor the progress of the flow code and in debugging. Solution steering has also been attempted in a CFD-pV3 coupled solver [35].

Improved mathematical modeling. Modeling the time dependent Navier-

Stokes equations to include turbulent fluctuations is still beyond the capability of modern computers. However, it is possible to make various simplifying assumptions to reduce the complexity of the mathematical model, thus making it tractable with current technology. In Reynolds averaged Navier-Stokes equations the Reynolds stresses are modelled by methods such as eddy viscosity, the k, ϵ equations and Reynolds stress averaging. Additional assumptions regarding the direction of flow and the absence of separation leads us to the thin shear layer approximation. This assumption reduces the number of stress terms to be calculated. In cases of unseparated flow with a thin viscous layer it is possible to separate the flow solution into the viscous and the inviscid domains. The inviscid solution is obtained by solving the Euler equations while a simplified boundary layer approximation can be used to determine the viscous effects. Such calculations are carried out iteratively with exchange of data at the inviscid-viscous boundary to reflect the influence each has on the other. The inviscid approximation provides sufficient valuable information like pressure distributions and lift for unseparated flows. Besides choosing a model, the numerical analyst also has to select a *spatial discretization* and an *equation discretization.* Choices of spatial discretization include structured and unstructured grids. Equation discretization includes methods such as finite element (FEM) and finite volume methods (FVM). The accuracy and robustness of FVM coupled with the flexibility of unstructured grids have resulted in some very efficient numerical techniques including the method, reported by Crumpton [12], which will be used in this thesis.

Unstructured grids Methods based on unstructured meshes for complex three dimensional geometries have become popular for various reasons. They include: (a) relative ease in grid generation, (b) ease in grid adaptation and (c) ability to increase grid density only in region of interest. With Delaunay based tetrahedral grid generators [75] it is now possible to create a million tetrahedral elements in a few minutes on a desktop workstation. An unstructured grid for an aircraft can be generated within an hour. In an attempt to reduce the memory overheads of the computational method, researchers have made innovative use of data structures [55].

Numerical acceleration schemes Iterative solvers are used to solve the algebraic system of equations that results from the numerical discretization. Techniques to accelerate convergence for such solvers have led to drastic reductions in CPU time. Acceleration schemes such as multigrid [57] are known to reduce CPU times by an order of magnitude. Preconditioning methods also provide considerable reductions in CPU time, especially when coupled to conjugate gradient methods.

The repercussions of such advances in the industrial environment are many. CFD, which was long regarded an irritant, has emerged an integral part of the design process. However, the current role of CFD in the design process is not a dominant one for the want of accuracy. Inviscid calculations can be performed accurately, but as the name suggests it is only an approximation to the viscous flow field. Viscous solutions are extremely sensitive to turbulence models and their accuracy is suspect. Thus, designers prefer to use CFD solutions in conjunction with wind tunnel and flight test data as inputs to the design process. The primary advantage gained by incorporating CFD into a design loop is the consequent decrease in design time. In comparison to experimental methods, it is trivial to reevaluate the flowfield for (a) a different set of free stream conditions, and (b) minor modifications to the geometry, once the basic grid has been acquired. With the use of unstructured grids even grid generation time can be reduced. This inherent flexibility of CFD has prompted its use as a design tool to quickly evaluate prospective configurations and select the most feasible ones. An additional advantage of CFD is its viability in a global optimisation system. Since structural analysis, weight estimation, electromagnetics and other fields also use computational models to perform their analyses, it is possible to develop an interdisciplinary optimisation study to analyze configurations that may not be ideal from an individual perspective but may be excellent from a global standpoint. Winglets are one such configuration. Their inclusion purely based on aerodynamic considerations is not ideal. However, when an optimisation based on aerodynamics, structures and weight estimation is performed it becomes a worthwhile concept and has been included in many aircraft. The present thrust of CFD is primarily directed towards analysis ie. predicting the flow field around a given geometry. While this has many applications, designers often want the opposite ie. to determine the shape that will produce a chosen flow field. This occurs because designers can often specify good pressure / lift / velocity distributions based on the performance required from the geometry.

A word of caution for the "CFD in design" enthusiast is given by designers at Boeing [39] "*A key CFD judgement that the design engineer is constantly facing is when to leave the CFD world and go to the wind tunnel. There comes a point in every design exercise where the codes are no longer the proper evaluation arena, and then testing is warranted.*"

Computational methods to compute a shape from a target (pressure / velocity / lift) distribution exist and are broadly categorised as (a) *Inverse* methods and (b) *Direct* methods. Inverse methods solve a modified set of governing equations so that the solution determined also includes the geometry influencing the flow. These methods require only one solution of the governing equation and thus are computationally cheap (of the order of one analysis run). Inverse methods are used in airfoil design [44],[43],[63]. Direct methods, on the other hand, use normal CFD codes controlled by an optimisation routine that attempts to minimise a cost function. These methods are invoked with a datum geometry and they progressively alter the geometry to achieve the target [7]. Direct methods are computationally intensive and have been used in wing [9],[51],[68] and airfoil [8] design.

The question that arises is, if there is a way to specify a target distribution around the whole aircraft, is there a design method that can determine the shape of the aircraft? The answer is *No*. The final design is testimony to a very large number of trade-offs and multidisciplinary issues which cannot be represented suitably in a target distribution or a simple optimisation cost function. In an optimization based system, each objective function evaluation involves a full CFD solution, thus current computational resources impose restrictions on the number of design variables in each optimisation problem. However, computational optimal design methods (CODM) have a role to play in a large design exercise by (a) accelerating the design of components and (b) contributing to interdisciplinary design. These aims can be achieved by providing a comprehensive tool to the designer that provides access to CFD technology through a design oriented interface. Such an interface should permit the specification of any design problem as an optimization problem where the designer can change the cost function, design variables and constraints at will. This will enable the designer to gain a complete understanding of the design space and also experiment with new concepts and trade-offs not tried before.

To be able to identify a framework for such optimisation methods in an aeronautical design process, we need an understanding of the design process itself.

Section 1.1 introduces the aeronautical design process,

Section 1.2 describes the current role of CFD in the design process and then attempts to predict the impact of optimization based computational methods in the aeronautical design process.

Section 1.3 presents some of the typical problems encountered in turbomachinery design, which will influence our approach to design.

Section 1.4 The test problem and design method followed in this thesis is presented along with arguments that influence this choice.

1.1 A Brief Introduction to Aeronautical Design Philosophy

Project Evaluation and Feasibility Studies During this stage, prospective customers are approached for information on the kind of engine that they need to fill existing or anticipated vacancies in the fleet. The design and feasibility groups evaluate the user needs with respect to available technology and expected technological developments. They also review the existing product line to find cost effective solutions, such as modifications to existing products. Empirical or semi-empirical formulae and statistical analysis of existing engines coupled with CFD forms the basis of decision making at this stage.

Preliminary Design After having decided that there is sufficient justification for producing a new engine, basic issues of design are tackled, such as (a) aerodynamic design, including selection of blade sectional and planform features, number of compressor and turbine stages, (b)installation and air-intake design, and (c) weight estimation. The preliminary design phase ends with the creation of a development schedule including detailed specifications of engine configuration, performance and control systems.

Detailed Design In the detailed design stage each part is individually designed and located within the global scheme of affairs. During this phase, various participating departments communicate extensively to ensure that each part is built to its specifications, and in cases where the specifications are unobtainable the departments advise a rewrite of the relevant specification. Such shortfall can often delay projects by upsetting design objectives.

Flight Tests A prototype is made and is subjected to ground tests and flight tests to ensure that all system perform as required. During the two testing phases, there is extensive feedback to the design and manufacturing groups to ensure smooth integration of systems. Many changes resulting from these tests are incorporated into the final product. The flight test stage is also a major point of learning for the company as a whole. Initial specifications and flight test data are meticulously documented to assist future design exercises.

Safety tests are conducted after flight tests to demonstrate compliance with safety requirements imposed by regulatory agencies. Following successful completion of tests the production process is developed (or refined), and the engine is manufactured. Often each customer might require additional alterations to meet their specific requirement.

While the above description is about an engine, a very similar schedule can be drawn up for airplanes. Our study (in the next section) of the above scheme yields some very interesting pointers to the kind of computational tools required in the aircraft/engine design process. See also [18], [62], [61] and [73] for more information on the design process.

1.2 CFD and Optimization in the Design Cycle

CFD is used extensively in both the preliminary and detailed design phases. During project evaluation, CFD is coupled with empirical/statistical formulae that lets the design committee evaluate the probability of a project reaching a successful conclusion. Possible configurations are selected and analyzed using CFD, the solution is then used to determine the structural, material and onboard system requirements and to evaluate the feasibility of such a project. Wing, horizontal tail, vertical tail, fuselage and airframe-engine integration are all simulated on the computer to permit a quick evaluation of performance that can be expected from such a configuration. Once agreement is reached by the design committee that the project is feasible, the preliminary design is initiated.

CFD is used extensively in the preliminary design phase and in internal company exercises to identify new concepts and perform feasibility studies. Airfoil design is almost entirely performed using inverse design methods. It is in this design phase that an optimisation driven CFD method will make the maximum contribution. The designer needs to be able to pursue several options and find the best match between various design parameters. The relation between these parameters is not always obvious and currently much of the design is based on designer "intuition", experience and some optimisation based methods. It should be emphasised here that the thrust of this argument is not aimed at proving optimisation based methods to be superior to the skills of a good designer, but to state that these methods will enhance a designer's ability to explore more possibilities within the time constraints of a design exercise (or to reduce the time taken for a specific modification) and to reduce reliance on "hunches". As stated earlier, design is a very complex optimisation exercise and it is not possible to easily frame a cost function for a global optimisation problem that will result in the "optimal" configuration. However, it is possible to design components and subsystems with optimisation based methods whose cost functions can be specified by designers. Responsibility for ensuring that a local minimisation will not run contrary to global system requirements lies with the designer and will influence the formulation of the optimisation problem. Restrictions imposed due to other disciplines (ex. manufacturability) can be introduced as constraints in the design space. Such techniques can be used in the integration of various subsystems. Also, since most manufacturing now involves the use of Computer and Numerically Controlled (CNC) machines, the use of a computerised shape database for computational methods (in fluids, structures etc) leads to easy transition from shape design to manufacturing.

Industries have pursued such ideas internally, but due to the commercial nature of these issues very few publications are available to the general reader and therefore have not been subjected to greater scrutiny by the academic community. It is only now that industries are beginning to publish more [69],[63],[39],[79],[28] with the hope that greater research interest will benefit them.

1.3 Typical Problems Encountered in Turbomachinery Design

In the above section general design principles related to aircraft and turbomachinery have been discussed. However, in this thesis we will be interested in application of design algorithms specifically to turbomachinery components. This section briefly introduces the kind of problems encountered in turbomachinery design that can be targeted by computational design methods.

The design of a gas turbine greatly reflects the projected use for the engine. Optimisation aimed at minimisation of weight will be a key priority in aeronautical applications. If the objective is to design an engine for a missile then the engine will be required (a) to be light (b) to start in the most adverse conditions and do so quickly. The life of components for such engines will not be important. However, if the engine is for military aircraft applications, besides minimisation of weight, design objectives will include good off-design performance and engine slam (combat maneuvers require fast variation of engine thrust). The choice of turbofan or a turbojet configuration depends on the combat role envisaged for the aircraft. Aircraft with deep penetration or close air support roles prefer turbofans (for lower fuel consumption) but this results in greater engine size which contributes not only an additional weight but also profile drag. The trade off between excess drag, weight of engine versus the lower fuel consumption rate is the design problem that has to be carefully resolved. In civil aircraft applications, the choice of turbofans has been a long proven one. The primary design objectives here include increasing component efficiency, life and decreasing weight. These objectives reflect advances in both aerodynamics (CFD) and metallurgical engineering. Described below are some of the primary problems faced in design/development of civil turbofan engines (the choice of the term "civil turbofan" reflects our concern with large bypass engines).

Compressors All modern compressors used in jet engines are axial flow compressors. However, radial compressors are still in use in APUs (auxiliary power unit) and in industrial gas turbines. Radial compressors give better compression ratios per stage resulting in reduced compressor size but are unwieldy in multiple stage compressors. Primary goals of compressor design include (a) increased efficiency and (b) increased pressure rise per stage. These goals lead to the following design concerns. Higher compressor flows can be achieved by increasing rotational velocities, but it can result in supersonic tip Mach numbers leading to shock losses. Lowering hub diameters to offset supersonic tip Mach numbers results in thicker blades at the root (for structural reasons) and heavier disks to support these thicker blades. Tip clearance is another issue of considerable interest. Besides aerodynamic issues the designer has to consider the manufacturability and associated costs of manufacturing. The wide variety of tradeoffs open to the designer are evident. While, such issues pertain to per stage performance, the compressor as a whole must also have some "well behaved" characteristics. It is highly undesirable to have a compressor where a number of stages stall or unstall together. Further, the compressor should not possess flow asymmetries at compressor outflow, as it leads to reduced combustor efficiencies and "hot spots" in the turbine first stage. The prediction of off-design performance of the compressor based on stage parameters is nearly impossible. A local minimisation to obtain excellent stage performance may be detrimental when viewed from a global perspective.

Turbines The burning of fuel in the engine signifies the addition of energy to the system. The maximum possible fuel/air ratio is used to determine the working temperature of the turbine blades. This is the turbine entry temperature (TET), temperatures up to 1850K have been reported. TET is primarily limited by the metallurgical technology available. Aerodynamic design of the turbine is critical. As opposed to about 15 compressor stages, there are only 2-4 turbine stages. The low number of stages is due to cost reasons. Cooling of HP turbine blades is critical, while it is important to maintain low losses in the LP turbine. Exit area of the turbine is very important and larger areas are preferred. Larger area results in lower flow velocity past the blade and lower blade losses. It is also easier to mix the bypass and the core flows if the core flow is slower (thus reducing noise and increasing engine efficiency). Minimisation of the swirl leaving the turbine is also important.

Pylon-OGV-Fan The pylon (the structure that links the engine to the aircraft, see fig 1.2, pg 12) is a large obstruction to the flow in the bypass duct. Figure 1.3 (pg 12), presents a 2D cylinderical slice through the bypass duct, with the "inlet" at the fan trailing edge (TE). The pressure field induced by the pylon has been observed to extend upstream through the bypass duct to interact with the fan. Such an interaction results in reduced fan blade life and in higher noise levels. The flow leaves the fan with a non-zero swirl angle and this flow is straightened in the bypass duct by a set of outlet guide vanes (OGV's). The OGV's are designed carefully to match the incidence of the flow. As a result of the pylon-pressure perturbation, a reduction in outlet guide vane (OGV) efficiency has also been observed. This problem is used as the test problem in this thesis and is discussed further in Chapter 5 . Redesign based on techniques discussed in Chapters 3 and 4 is presented in Chapter 5. A redesign of a three dimensional pylon-OGV-fan interaction problem in presented in Chapter 6.

Nacelle design The move towards two engine long range aircraft (such as the Boeing 777) has prompted engine manufacturers to produce turbofans with very large fan diameters. Consequently, the vertical displacement between the engine nacelle and the wing has been reduced (to meet ground clearance requirements). Such a narrowing creates a converging-diverging nozzle between the nacelle and the wing lower surface. At cruise velocities shocks appear here resulting in increased drag. To alleviate this, engine and aircraft manufacturers are being forced to look

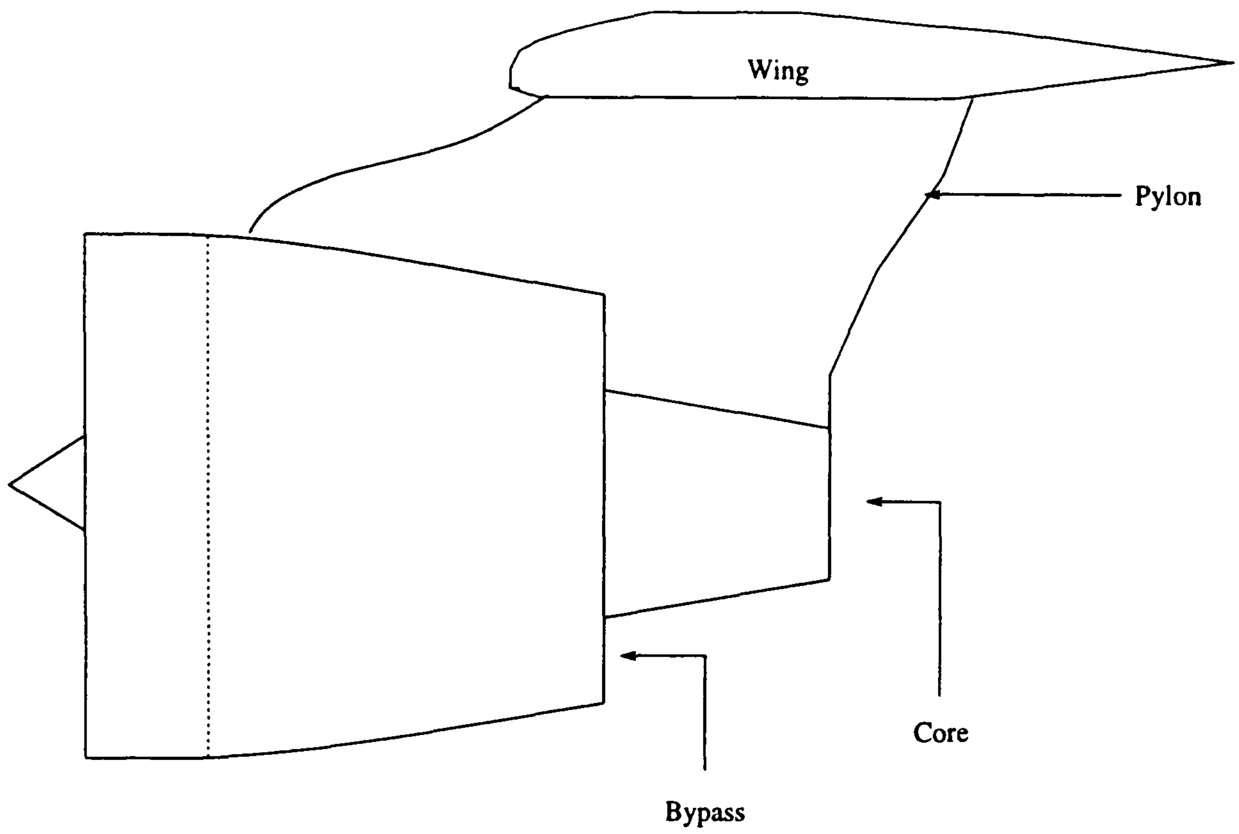

Figure 1.2: An illustration of a wing-pylon-engine connectivity.

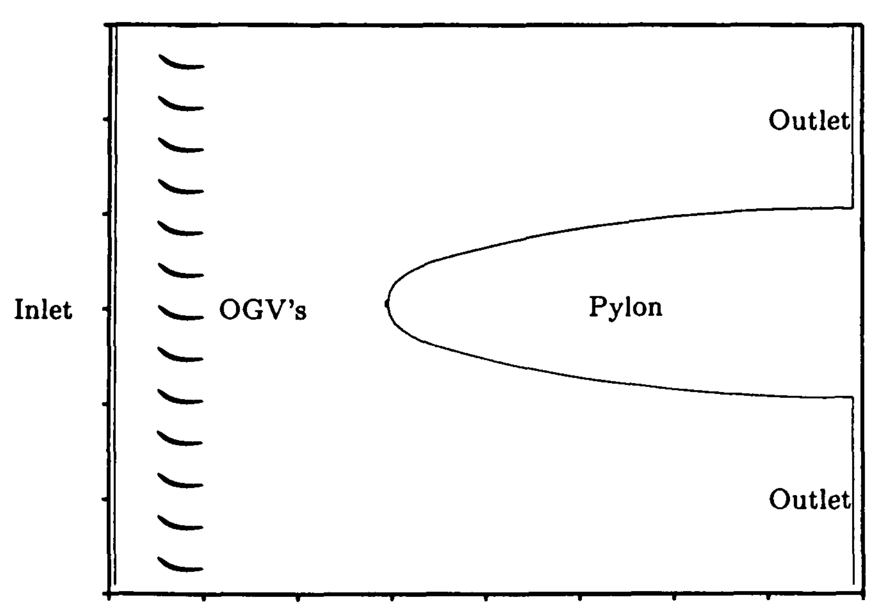

Figure 1.3: A 2D cylinderical slice through the bypass duct.

closely at nacelle design. CFD based methods to predict and optimise shock losses have been attempted [59] and [31].

See also [18], [11] and [62] for more details on issues related to gas turbine design.

1.4 Design Approach Attempted in this Thesis

The range of problems that need to be tackled in a turbomachinery design loop are enormous. Thus, any design method being developed needs to retain a clear sense of direction and ensure that any design method developed is not too specific to the test cases used. The choice of a design approach for this thesis will be based on (a) computational methods available and (b) type of design problems that we wish to attempt.

The computational methods available are:

Linear Perturbation Analysis Giles has developed a linear perturbation analysis method called SLiQ [24]. This method first solves the nonlinear steady Euler equations on a 3D structured grid. It then uses a linear perturbation approach to obtain the sensitivity of the flow field parameters to geometric perturbations (see Chapter 3).

2D/3D Unstructured Euler Analysis Crumpton has developed two and three dimensional Euler solvers based on unstructured grids [12],[13]. These solvers use acceleration tools such as parallel processing and multi-grids to decrease the time required for a solution.

The aim of the current exercise is to develop a framework for design based on a suite of tools to meet the needs of the designer subject to the time and computing constraints. It is essential that quick, simple and robust tools be available in conjunction with more complex, but time consuming, methods. The local availability of inviscid computational codes limits the class of problems that can be targeted for developing such a framework. One important design problem is the alleviation of pylon-OGV-fan interaction. The pylon induced pressure wave is an inviscid phenomenon. This problem is known to designers and is usually tackled using analytical techniques. Thus, any CFD-based design method evolved to alleviate this would be a worthy contribution to the design process and also a powerful tool to understand and develop design methods.

Therefore, this thesis will attempt to develop a set of design approaches aimed at the pylon-OGV-fan interaction problem involving sensitivities obtained from (a) a linear perturbation method and (b) an Euler code. Non-gradient based optimization methods will also be investigated.

The redesign will be aimed at altering the shape of the OGV's using the concept of cyclically varying camber (further discussed in sections 5.1-5.2, pages 84-86). In keeping with the above strategy, the scheme of the thesis will be as follows:

Chapter 2 introduces the formulation of the design problem as an optimisation problem and reviews several currently used and researched techniques.

Chapter 3 A design method based on linear perturbations and actuator disc method is discussed.

Chapter 4 A quasi-newton design method based on sensitivities obtained by finite differencing is developed. A grid movement method used to perturb the geometry is also presented.

Chapter 5 Methods introduced in Chapters 3 & 4 are applied to the test problem in Chapter 5.

Chapter 6 The quasi-Newton method is applied to a three dimensional blade row.

Chapter 7 concludes with a discussion and suggestions for future research.

Figure 1.4 (pg 15) presents the structure of the thesis as a flow chart.

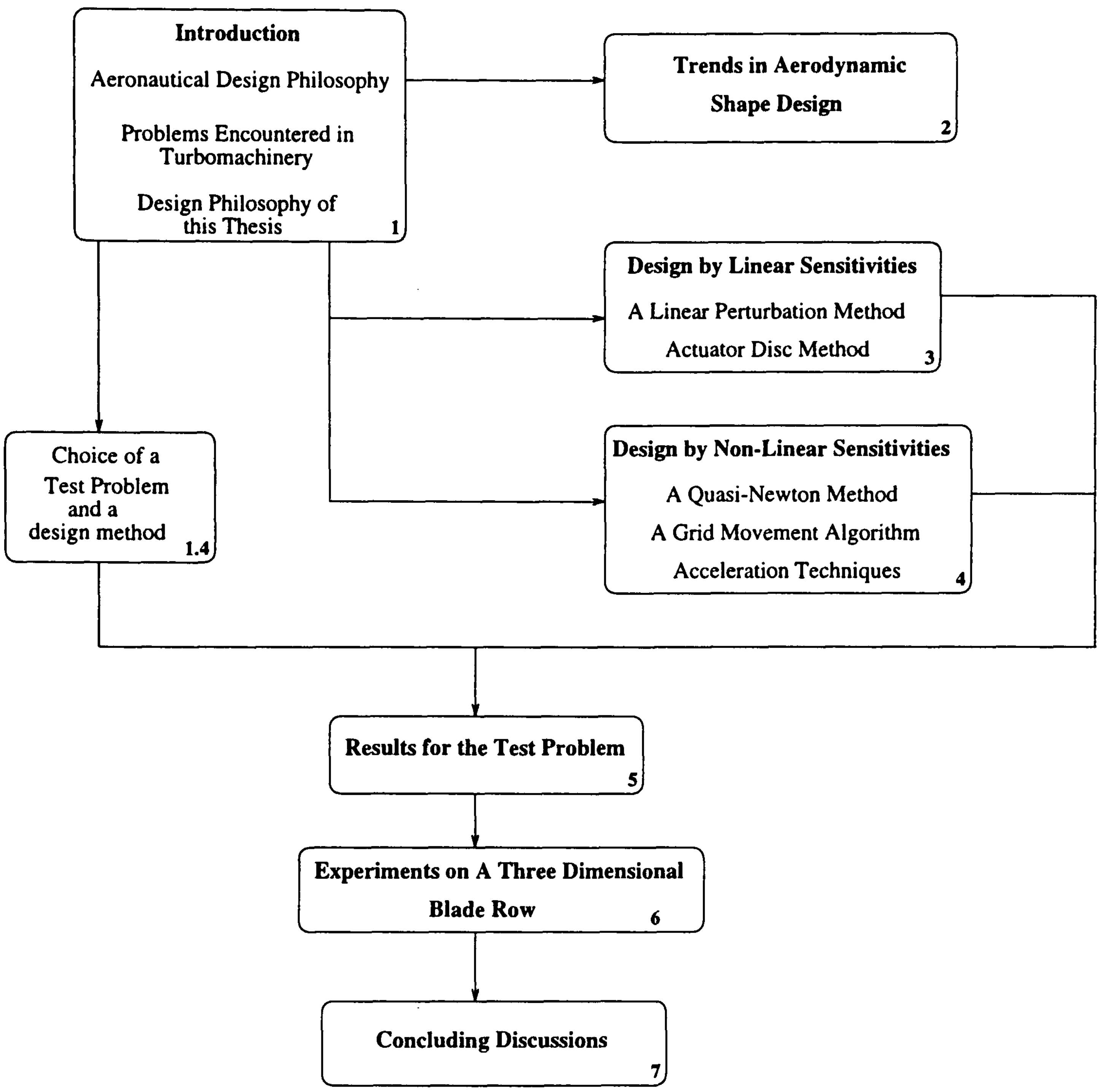

Figure 1.4: Flow Chart of the Project.

Chapter 2

Developments in Aerodynamic Design and Optimization

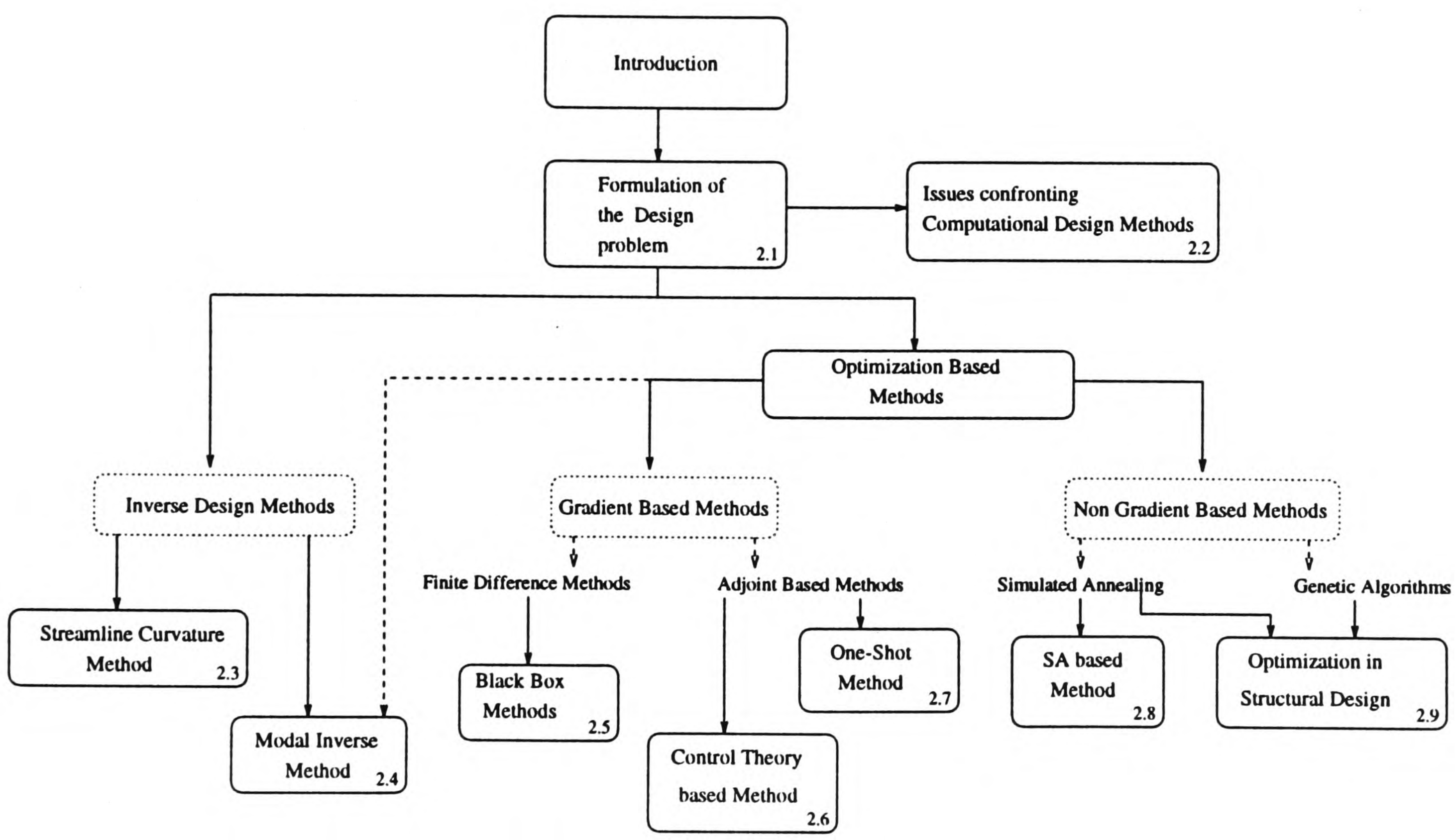

Figure 2.1: Flow chart of Chapter 2.

Aerodynamic design techniques have traditionally been categorised as: *Inverse methods* which utilise an inverse solver in at least a part of the computational domain, and *Direct methods* which employ a direct analysis solver in an iterative manner. Inverse methods attempt to compute a shape that will generate the user specified pressure distribution. This approach has an advantage in that only one solution of the governing equations is necessary (as opposed to the iterative scheme of Direct design) and so it is computationally cheap. However, a physically realisable shape may not exist for the specified pressure distribution. Thus, inverse methods require the target distribution to be very carefully formulated to achieve a feasible shape. Inverse methods are still used as a preliminary design tool for the design of airfoils. Two such method are reviewed in sections 2.3 and 2.4.

The problems encountered with specifying target pressure distributions can be circumvented by formulating the design problem as one of minimising the difference between the current and target pressure distributions. Such an approach will always result in a physically realisable shape, thus recasting a possibly ill posed problem as a well posed problem. The disadvantages of this approach are (a) each objective function evaluation involves at least one CFD solution, and (b) added computational expense due to the optimization procedure. Minimisation methods blur the line between inverse and direct design philosophies. As a result, such classifications are rarely used anymore.

Since modern design methods employ concepts of optimization, a study of the underlying mathematics is essential. The following section introduces the theory (see also [71]) and uses it to classify methods that will be reviewed in subsequent sections.

2.1 An Introduction to the Underlying Mathematics

The aerodynamic design optimization problem can be expressed as

$$\begin{aligned} \text{minimise} \quad & I(\alpha, \mathcal{F}) & & & (2.1)\\ \text{subject to} \quad & U(\alpha, \mathcal{F}) = 0 & & & (2.2)\\ & G_i(\alpha, \mathcal{F}) = 0 & & i = 1, \ldots, NeqCons \\ & H_j(\alpha, \mathcal{F}) \leq 0 & & j = 1, \ldots, NneqCons \end{aligned}$$

where α is the vector of design variables and $\mathcal{F}(\alpha)$ is the vector of flowfield variables. $I(\alpha, \mathcal{F})$ is the user specified cost function that is to be minimised. $U(\alpha, \mathcal{F})$ represents the governing equations of the fluid flow and relates $\mathcal{F}$ to α. G and H are the equality and inequality constraints imposed on the system. Various optimization methods can be used to solve this problem. These techniques can be broadly categorised into (a) *Gradient* based (GB) methods and (b) *non-gradient* based (NGB) methods.

2.1.1 Gradient Based Methods

GB methods determine the gradient vector at the current point in the design space and then make a step in the negative gradient direction. Thus, evaluation of the gradient vector is crucial to such methods. Convergence can be speeded up by using sophisticated descent methods such as quasi-newton or conjugate gradient methods.

A change $\delta\alpha$ in α influences the following change in I

$$\delta I = \delta\alpha^T \frac{\partial I}{\partial \alpha} + \delta\alpha^T \left(\frac{\partial \mathcal{F}}{\partial \alpha}\right)^T \frac{\partial I}{\partial \mathcal{F}} \tag{2.3}$$

The corresponding gradient vector can be expressed as:

$$\nabla_\alpha I = \frac{\partial I}{\partial \alpha} + \left(\frac{\partial \mathcal{F}}{\partial \alpha}\right)^T \frac{\partial I}{\partial \mathcal{F}} \tag{2.4}$$

All terms in this expression are easy to evaluate except $\frac{\partial \mathcal{F}}{\partial \alpha}$. This term represents the sensitivity of flow field parameters to changes in design variables. The various approaches to GB aerodynamic design differ essentially in the way they compute this term and they are as follows:

Finite Difference Methods

Here the term is evaluated by finite differences. If β represents the unit vectors that span the design space and m is the dimension of this space, the design vector can be expressed as $\alpha = \sum_{j=1}^{m} \alpha_j \beta_j$. If ϵ is a perturbation, then the sensitivities are calculated as

$$\frac{\partial I}{\partial \alpha_j} = \frac{I(\alpha + \epsilon\beta_j) - I(\alpha)}{\epsilon} \tag{2.5}$$

and collated as

$$\left(\frac{\partial I}{\partial \alpha}\right)^T = \left\{\frac{\partial I}{\partial \alpha_1}, \frac{\partial I}{\partial \alpha_2}, \ldots, \frac{\partial I}{\partial \alpha_m}\right\} \tag{2.6}$$

It is obvious that there have to be at least $m + 1$ evaluations of the flow field to evaluate $\nabla_\alpha I$. The finite difference approach is feasible in cases where the number of design variables is small. The size of ϵ and its effect on the accuracy of the computed gradient is a concern for such methods. Most black-box direct design methods use finite difference methods to evaluate sensitivities.

Adjoint Based Methods

These methods are very efficient in calculating the gradients for constrained optimization problems, even when the dimension of the design space is large. This approach involves the use of Lagrangian multipliers and solving a set of co-state equations. The term $\frac{\partial \mathcal{F}}{\partial \alpha}$ in equation (2.4) can be replaced by using

$$\frac{\partial U}{\partial \alpha} + \left(\frac{\partial \mathcal{F}}{\partial \alpha}\right)^T \frac{\partial U}{\partial \mathcal{F}} = 0 \tag{2.7}$$

which is obtained from equation (2.2). We get

$$\nabla_\alpha I = \frac{\partial I}{\partial \alpha} - \frac{\partial U}{\partial \alpha}\left(\left(\frac{\partial U}{\partial \mathcal{F}}\right)^T\right)^{-1} \frac{\partial I}{\partial \mathcal{F}} \tag{2.8}$$

Introducing the vector

$$\left(\frac{\partial U}{\partial \mathcal{F}}\right)^T \lambda + \frac{\partial I}{\partial \mathcal{F}} = 0 \tag{2.9}$$

we can express the gradient as

$$\nabla_\alpha I = \frac{\partial I}{\partial \alpha} + \frac{\partial U}{\partial \alpha}\lambda \tag{2.10}$$

where λ is the Lagrangian multiplier (also referred to as the costate variable). The minimisation is performed by repeated application of the following steps:

(i) Solve $U(\alpha, \mathcal{F}) = 0$ using the current α, thus determining $\mathcal{F}$

(ii) Using α and $\mathcal{F}$ determine λ from equation (2.9)

(iii) Update α by taking a step in the direction of the negative gradient (evaluated from equation (2.10)).

Methods described in sections 2.6 and 2.7 are adjoint based methods. Application of adjoint methods to design problems was pioneered by Pironneau [60] and Jameson [40]. This closely resembles the method for calculating transonic potential flow proposed by Bristeau et al [5]. Adjoint methods are also used by Baysal et al [4], Agarwal et al [50] and at Boeing [79].

2.1.2 Non-Gradient Based Methods

NGB techniques are a recent development in optimization techniques and rely on the availability of cheap and fast computing power. NGB methods rely on randomised searches to determine the minima. It must be emphasised that randomised searches do not mean random searches. There is an overall method to the search, but they rely on probabilistic as opposed to deterministic traversal of the parameter space. Since they do not use gradient information, they avoid the pitfalls associated with local minima and noisy cost functions. NGB methods include:

Simulated Annealing (SA) results from the application of principles of statistical mechanics to multivariate or combinatorial optimization. It was first proposed by Kirkpatrick [64] in 1983. It is based on the physical process of cooling of materials where minimum energy states are reached for sufficiently slow cooling. Each state can be defined by the set of atomic states (or positions) which is identical to the design vector. The state itself can be described by (a) an average due to the combination of the atomic states and (b) small fluctuations about this average. In a CFD optimization process, (a) is similar to the value of the objective function at the current point in the design space and (b) represents noise in the objective function. The lowest and stablest ground states of materials are obtained by careful annealing. In practical cases the temperatures of the liquid form is reduced slowly; the cooling rate is further decreased in the vicinity of the freezing point. Such a cooling schedule avoids the formation of defects in the resulting crystals. In optimization terms this translates to identification of the absolute minima. SA has an "effective temperature" for each system that is used to determine the rate of cooling. In the optimization process small random changes to the design are made and accepted under certain conditions. Accepting only changes that result in reduction of cost function is similar to quenching and thus results in metastable states; instead some changes that worsen the design are accepted. The decision to accept a change that results in a worsening of the cost function is based on a Boltzmann distribution linked to the effective temperature. SA can be described as a sequence in which at each step of the Markov chain a design parameter is perturbed and a decision is made on whether to accept this change or not (based on the resulting change of the cost function and the temperature).

Genetic Algorithms (GA) simulate the natural process of genetic selection (survival of the fittest) by maintaining a set of competing designs and manipulating the design parameters of the pool to identify new promising generations while discarding dead-ends (see [29]). Developed by Holland et al [38], GA's seek to introduce robustness to artificial optimization system by mimicking biological processes such as self-repair, self-guidance. GA's work with a coded form of the design vector and not the vector itself. The coding of the vector space results in a finite length string over some finite alphabet. The search is coordinated by the GA from a population of points and not from a single point (as a deterministic method would). The objective function is the only measure used by the GA, similar to "quality of life" in a natural system. The better the quality, the higher the chance of survival. A randomised initial population is first created and then the GA creates successive generations by introducing mutations, crossovers and reproduction in the current population.

NGB methods are very compute intensive and need to evaluate the cost function many many times, making them prohibitive for some CFD applications. Recent publications have indicated that with modifications methods such as SA can be used in conjunction with GB methods to quickly determine the global minimum. One such method is reviewed in section 2.8.

2.2 Issues Confronting Aerodynamic Design

Some prominent issues that confront computational aerodynamic shape design are:

(i) Choice of optimization procedure The success of an aerodynamic shape design depends on the optimization method selected. As indicated in the preceding section, the two fundamentally different approaches are the GB and NGB methods. GB methods can be easily linked to an interactive system which allows the designer to explore the design space. Since they depend on gradients, such an interactive system allows the designer to acquire an intuitive feel for the design space. However, initial conditions and the quality of the flow solution are major influences in the performance of a GB method; in the worst case it is possible for numerical errors to direct a GB scheme towards a local or a spurious minimum. In comparison NGB schemes are immune to such pitfalls and will find the global minimum (subject to minimum quality of flow solutions). The disadvantage is the compute intensive nature of such methods. Also, since NGB methods are stochastic and do not have any obvious route while reaching the minimum, any interactive scheme based on them is highly unlikely to give the designer a "feel" for the design space. It is our opinion that a suite of NGB and GB schemes will possibly be the best alternative placed at the designer's disposal, allowing him to determine which scheme to use under the given circumstances.

(ii) Use of discrete or continuous sensitivities This problem arises with the use of GB methods. Sensitivities can be computed using the continuous adjoint problem (eqns (2.7-2.10) applied to the governing flow equations) or alternatively using the adjoint equations obtained from the discrete flow equations. This discrete adjoint equation is a particular discretization of the continuous form. Issues at hand include the computational expense in discretising the continuous form of the adjoint equation. This is a current area of research. The continuous form is used by Jameson et al [42] while the discrete method has been adopted by Baysal et al [4].

(iii) Coupling of Aerodynamic and Optimization methods The inclusion of a computational method into an industry is a long and expensive process. They are subjected to rigorous tests on a suite of problems including comparisons to available experimental and flight test data. Design methods that closely couple flow codes and optimization methods (such as the *one-shot* method, section 2.7) create codes that will need to undergo the complete validation exercise. Additionally, since these are essentially design codes, new techniques of validation will have to be developed. Design methods which adopt a loose coupling of optimization and (verified) flow codes have a considerably shorter validation cycle. In the current short and medium term context it appears that a loosely coupled setup will yield maximum benefit.

(iv) Choice of cost function and design parameters The choice of the cost function is as crucial as the choice of an optimiser in the overall design process. Many design parameters (such as structural strength) cannot be included in aerodynamic shape design as a variable and need to be introduced as geometric constraints. It is often the case that such extraneous influences result in an overconstrained problem rendering it intractable. Thus the cost function should be malleable and be specified by the designer for each optimization run. Similarly, it should be possible to specify some constraints as "weak". Such flexibility will allow the designer to pose the problem in many ways and assist in identifying bottle-necks and routes to achieving design goals.

(v) Shape Definition Another very important issue facing aerodynamic design is shape definition. Currently, shapes are developed by design methods in complete isolation from manufacturing systems (with some input on manufacturability). The shapes are then input to a centralised CAD database from where the manufacuring instructions are determined. Such an approach that involves explicit conversion from aerodynamic shapes to CAD shapes often slows down the process of design evaluation (by structural and other groups). A centralised CAD shape database that has real time access to the latest aerodynamic shape will make it possible to have real time analysis of the component from several other stand points. Several industries are already pursuing such standardisations internally.

(vi) User interface Visualising CFD results has become common place. Besides being a tool for viewing the flow solution, it is also used to identify flow features that influence the flow field. The way CFD results are presented on a computer is straightforward (while its implementation is not). It is based on a planar representation with additional probes like stream-tubes, ribbons and other visualisation techniques borrowed from experimental aerodynamics. The scheme for presenting design results is not so obvious. The options available include:

- presenting only the final result
- presenting a convergence plot of the objective function
- at each point(in the design space), presenting various sensitivities available with the decision taken by the optimiser

Some of the above methods are suitable for an interactive approach while others are not. Using an interactive approach allows the designer to progressively change the objective function to incorporate issues not directly related to aerodynamics (ex. manufacturing costs) at an appropriate stage of the design. However, excessive reliance on sensitivity based design interfaces might lead to a highly localised design that can result in an overall deterioration. There must be some mechanism whereby the designer realises that a seemingly harmless change in a parameter drastically affects the flow elsewhere.

2.3 Streamline Curvature Method

Mean streamline curvature method (MSLM) was first proposed by Wu [77] in 1952 as a general theory of three-dimensional flow in turbomachines. The main concepts of MSLM are as follows. If the shape of a certain stream line and the variation of a physical quantity along this stream line is known, then it is possible to arrive at expressions for the first and higher partial derivatives of velocity V and density ρ from the steady inviscid isentropic two-dimensional flow equations. The fields are expressed as a Taylor series expansion and it has been observed that the first three terms of the expansion are sufficient for most engineering calculations. In practice, the mean streamline (MSL), which divides the channel into two equal parts, and the axial specific mass flow along the MSL are selected as input.

In the earlier days, the inverse design was performed as a direct problem with the cascade shape decided by "experience". Recent MSLM based methods involve an iteration between the mean S_2 streamsurface (S_{2m}) and several S_1 streamsurfaces of revolution. The S_1 streamsurface can be visualised as those perpendicular to the blade span, while S_2 can be visualised as being parallel to the blade camber line (see fig2.2). The first S_{2m} computation provides the shape and stream filament thickness of S_1. The blade profile on S_1 is determined with information from S_{2m} using a Taylor series expansion on the mean streamline. With the blade profile and thickness available, the flowfield on S_1 is computed, this is similar to conservation of angular momentum $V_\theta r$ applied on S_{2m}. This is incorporated into S_{2m} as a modification. With the modified S_{2m} the loop is repeated. This continues until there is no further modification.

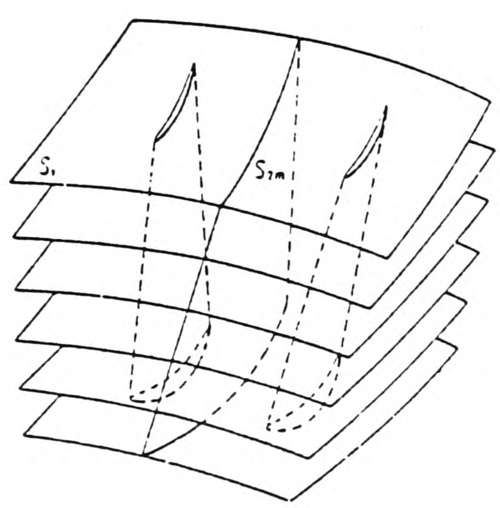

Figure 2.2: A mean S_2 streamsurface(S_{2m}) and several S_1 streamsurfaces of revolution. Figure from [80].

MSLM has been actively pursued in China [80], [78], [30] and is still used as a preliminary design tool to design airfoils for turbomachinery applications [69].

2.4 Modal-Inverse Method

When presented with pressure distributions containing shock discontinuities, inverse methods often produce airfoils with surface slope discontinuity at the foot of the shock. The modal inverse method proposed by Drela [15], which is reviewed in this section, overcomes this problem by limiting the changes proposed by the inverse code to a small number of smooth geometric modes (≤ 10). This is similar to optimization based inverse design methods (discussed in section 2.5). The use of smooth geometric modes ensures that the final geometry is smooth. In this method, the design problem is specified as either a

full-inverse problem where the pressure is prescribed over the entire airfoil surface,

or a

mixed-inverse problem where the pressure is prescribed over only a part of the airfoil surface and the geometry is prescribed over the remainder.

The geometric design modes are used to represent changes to a surface of the airfoil or to the camber line. The capability to perform changes based on the camber line are required in turbomachinery applications where the thickness of the airfoil has to remain constant due to structural reasons. Changes implemented as variations to the camber line retain the initial thickness while varying the airfoil geometry.

The underlying code in the inverse scheme is the ISES code [17], [25]. The code has a streamline based discretization of the steady two dimensional Euler equations in conservative form with capability to handle transonic flows, inverse or direct boundary conditions with or without boundary layers included. Here, a cell is defined by two streamlines and two quasi-normals (lines that need not be normals). The variables of density ρ, pressure p, velocities u, v, are located at the center of the quasi-normal cell face. There is no convection across the streamline face, so that only pressure p and the streamline

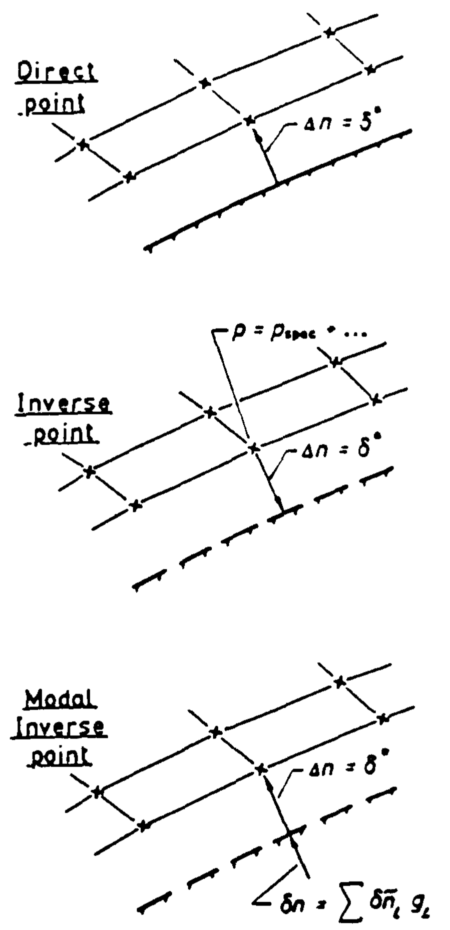

Figure 2.3: Grid node and variable locations. FIgure from [15].

node position x, y are needed as unknowns. The lack of convection across the streamline face leads to the substitution of continuity and energy equations by simple algebraic statements of constant mass flux and stagnation enthalpy in each streamtube. This reduces the number of unknowns to two ρ, n, where n is the normal position of the grid node (see figure 2.3, pg 26). The streamline grid is determined as a part of the solution.

The system of equations is solved using a Newton solver. For the initial guess, a streamline grid similar to the incompressible flow grid and a uniform density equal to the freestream value is chosen. The variables determined at the end of each Newton iteration are the streamline node movement δn and the density change $\delta\rho$ at each quasi-normal face. The linear system that is solved has the form

$$\left[\quad \mathbf{J} \quad \right] \left\{ \begin{array}{c} \delta n \\ \delta\rho \\ \delta \mathrm{G} \end{array} \right\} = \left\{ -\mathbf{R} \right\} \tag{2.11}$$

where $\mathbf{J}$ is the Jacobian matrix and $\mathbf{R}$ is the vector of all residuals. δG represents changes to global variables.

In the inverse form of the current method, the airfoil being designed is determined by the calculated shape of the two bounding streamlines. In the modal-inverse approach the boundary condition applied at a surface node is modified to

$$\delta n_i = \sum_{l=1}^{L} \delta\tilde{n}_l g_l(s_i) \tag{2.12}$$

where $\delta\tilde{n}_l$ is the mode amplitude, $g_l(s_i)$ is the geometric mode and s_i is the arc length position of surface node i. This is equivalent to perturbing the airfoil contour by the L geometric modes. If the same perturbation is applied to opposing points on the lower and upper surface it will result in the thickness being preserved and is equivalent to perturbing the airfoil camber line. The mode shapes used are smooth so the perturbed geometry is guaranteed to be smooth. The Newton method can be modified to give "free" sensitivities by including the modal inverse terms to the rhs of eqn (2.11), thus giving

$$\left[\; \mathbf{J} \; \right] \left\{ \begin{array}{c} \delta n \\ \delta \rho \\ \delta \mathrm{G} \end{array} \right\} = \left\{ \; -\mathbf{R} \; \right\} + \delta\tilde{n}_1 \left\{ \; -\mathbf{g}_1 \; \right\} \ldots + \delta\tilde{n}_L \left\{ \; -\mathbf{g}_L \; \right\} \tag{2.13}$$

This modified Newton solution does not constitute a "proper" Newton method because the modal constraints are not exact linearised forms of the least-squares constraint. The overall convergence rate is linear and not quadratic. However, in practice the discarded terms are so small that an order of magnitude decrease in residual per iteration is obtained.

2.4.1 Design of an Inviscid Transonic Airfoil

The redesign of a NASA supercritical airfoil is presented in [15]. The initial airfoil had a fairly strong shock on the suction side at $M_\infty = 0.75$ and $C_L = 0.8$ with $C_D = 0.01095$. The direct solution required ten Newton iterations which amounted to 12 CPU minutes on a VaxStation 3200 for a typical 132×32 grid.

In the redesign process the problem was specified as a mixed-inverse problem aimed at weakening the shock. Weakening of the shock was preferred to total elimination to prevent deterioration of off design performance. The angle of attack α was left as a free variable so that the design $C_L = 0.8$ was strictly observed. Four additional Newton iteration were needed to converge the redesign starting from the direct solution.

The redesigned airfoil has a slope discontinuity at the location of the shock (see fig 2.4, pg 28). This occurs because the specified values of C_p within the smeared shock being inconsistent with the values which would occur on a smooth surface. The modal-inverse method was used to modify the design to eliminate slope discontinuities(see fig 2.5, pg 29). The calculation uses five geometric perturbation modes The angle of attack α is left as a free variable (as before) to allow a design $C_L = 0.8$. Five Newton iterations were required to converge, starting from the converged airfoil case. As required, the new airfoil geometry is smooth.

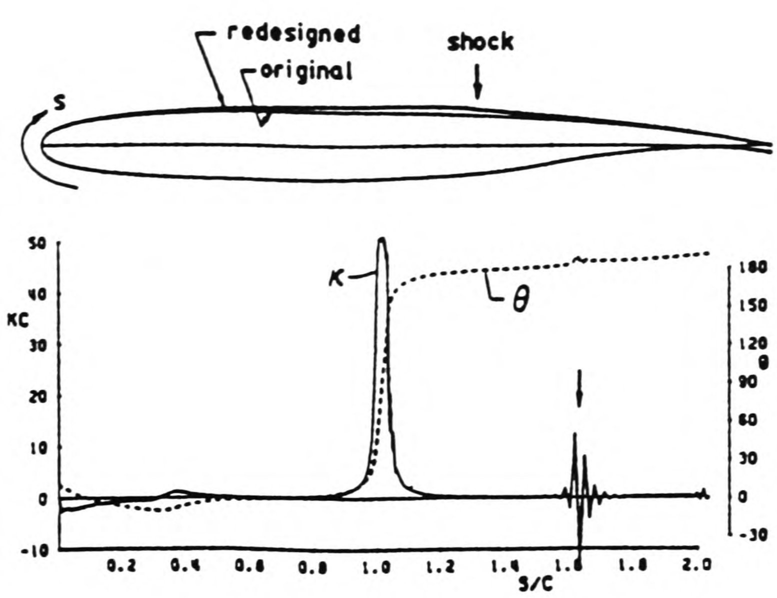

Figure 2.4: Comparison of original and mixed-inverse redesigned airfoil. Surface angle and curvature distributions on redesigned airfoils. Note: presence of shock and discontinuities. Figure from [15]

The computational expense for each geometric mode is about 3% of an analysis run. This low cost per mode is because each mode basically adds to the right hand side of the Newton system. The present method has been implemented by Drela in a design system called LINDOP [16]. In LINDOP a clever graphical interface coupled with the fact that sensitivities are available for all geometric modes allows the designer to interactively investigate various options available to him while the screen is updated to show the characteristics of the modified airfoil. After a set of design maneuvers, the geometric changes are implemented and the flow field is recomputed.

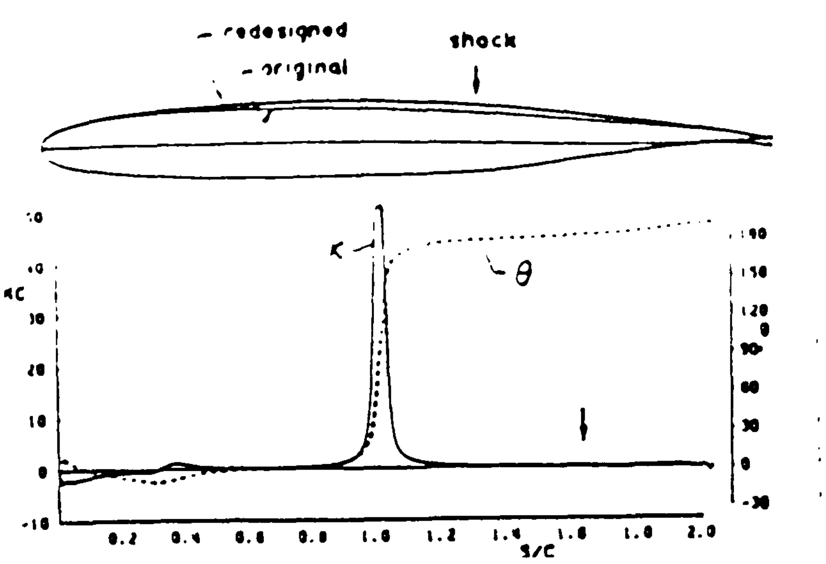

Figure 2.5: Comparison of original and modal-inverse redesigned airfoil. Surface angle and curvature distributions on redesigned airfoils. Note: how shock and discontinuities have been eliminated. Figure from [15]

2.5 Direct Design Methods

Direct design methods, as discussed in the introduction, involves the repeated application of an aerodynamic solver under the control of a black box GB optimization program. One such method is the *direct iterative surface curvature* method (DISC) due to Campbell and Smith [9], [8] which is reviewed in this section. DISC has been extended to include constraints [7] and is called CDISC. DISC has been applied to three-dimensional problems including wing design ([9], [8], [68]), design of winglets ([51]) and nacelle design ([51], [76]). Airfoil design using CDISC is demonstrated in [7].

DISC iteratively modifies the shape to achieve a target surface pressure distribution. An initial geometry is analyzed by the flow solver and the resulting surface pressure distribution is compared with the target distribution. If the two differ then geometric perturbations are calculated from set expressions that relate the local Mach number and pressure deficit to changes in curvature. The changes to the geometry are implemented by a grid movement algorithm and the new geometry is analyzed by the flow solver. This proceeds iteratively till the pressure deficit is minimised.

For subsonic and low supersonic Mach numbers ($M \leq 1.1$) the required change in surface curvature (ΔC) is related to the difference between the local objective and current pressure coefficients (ΔC_p) by the equation

$$\Delta C = \Delta C_p A(1 + C^2)^B \tag{2.14}$$

where A is the relaxation factor, which is positive for the upper surface and negative for the lower surface. Exponent B ($0 \leq B \leq 0.5$) is a control on the convergence rate with higher values enhancing the rate of convergence but with decreased stability in the nose region of the airfoil. The following relation is used when the flow becomes supersonic ($M > 1.1$):

$$\Delta C = \frac{d(\Delta C_p)}{dx} \frac{A\sqrt{M_\infty^2 - 1}}{2} \frac{1}{[1 + (dy/dx)^2]^{1.5}} \tag{2.15}$$

While observing that defining a "good" target distribution based on required aerodynamic performance (C_l, C_m) is possible, it must be noted that such a distribution is not unique. Further, the choice of the target pressure distribution, in the presence of geometric constraints, may make or break the design exercise. Campbell [7] has extended DISC to be capable of modifying the target pressure distribution while trying to achieve the same aerodynamic performance. This is done as the design cycle proceeds and ensures a successful completion of the design loop. The new method is called constrained DISC (CDISC), and consists of:

(i) generating initial target pressure distributions based on the aerodynamic and geometric constraints.

(ii) automated modifications to the target pressures during the design loop.

To facilitate this, the airfoil is divided into regions bounded by by control points as shown in figure 2.6(see page 31). This is similar to the method used by Malone et al [54] and Van Egmond [74]. The control points are determined by the following "rules".

Point 1 on each surface corresponds to the stagnation point.

Point 2 marks the end of the leading edge acceleration zone.

Point 3 terminates segment 2-3, the region of fairly mild pressure gradients.

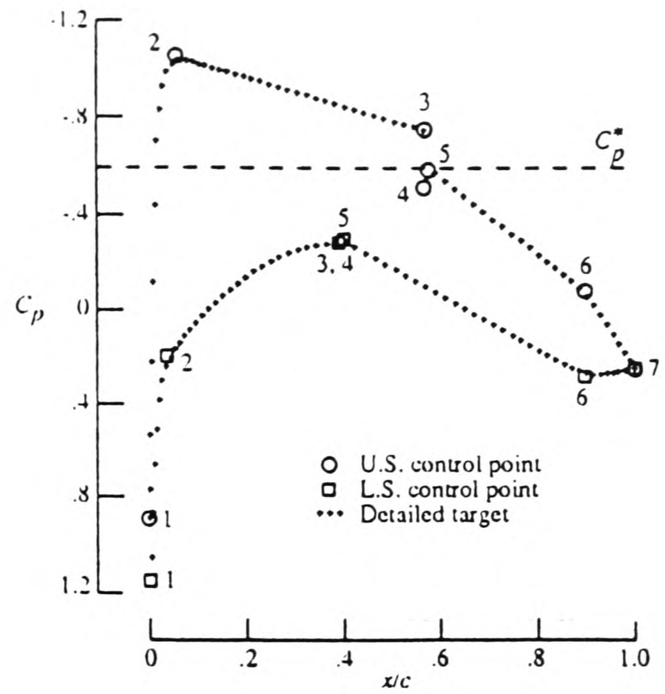

Figure 2.6: Control Points used to develop target pressure distribution. Figure from [7].

Point 4 represents the jump across the shock when a shock is present, else it is coincident with Point 3.

Point 5 is chosen to correspond to the point of maximum thickness of the airfoil.

Point 6 is placed between the point of maximum thickness (5) and the trailing edge (7). It represents the beginning of the final pressure recovery region.

Point 7 is the trailing edge point.

As the first step of computing a target pressure distribution from aerodynamic objectives, pressure levels associated with each control point needs to be computed. This is done by one of the following methods:

(a) determine initial values from empirical pressure-geometry relationships and characteristics observed for existing airfoils

(b) fit an existing pressure distribution to the control points.

Once the initial control point pressure values are known a detailed pressure distribution is developed by connecting the control points with simple analytic functions and then computing the pressure levels at points corresponding to the initial airfoil surface grid. The functions are either straight lines or parabola except at the leading edge where fourth-order and third-order polynomials are used for the upper and lower surfaces respectively. This becomes the initial target pressure distribution used by the design method.

As the design loop proceeds this target distribution is continuously reviewed and altered to achieve the desired objectives (in terms of C_l, C_m and C_d). This procedure is similar to the above target pressure calculation method in that it uses pressure-geometry relations. However, the perturbation form of these relations are used here. Changes to the target pressure is related to the difference between current and desired geometric parameters. Besides just changing the target pressures, this procedure also moves the location of the control points to meet geometric constraints. The changes are computed using relations between current and desired flow features and perturbations to control points.

It must be noted here that much of the above approach depends on empirical formulae and relations that have been arrived at by statistical and other methods. But the DISC typically represents several black box approaches, which rely heavily on existing design knowledge.

2.6 Application of Control Theory

The application of control theory based optimization techniques to airfoil and wing design has been pioneered by Jameson et al [40],[42]. Here the Frechet derivative of the cost function is evaluated by solving an adjoint partial differential equation (a technique borrowed from control theory) as described in section 2.1 (under "Adjoint Based Methods") and is governed by expressions (2.1–2.4) and (2.7–2.10). The boundary shape which serves as the control is then modified in the direction of descent. Control theory based methods are currently available for flows modelled by potential and Euler equations and have been applied to

(a) blade design for turbomachinery applications by Gu et al [33], [32],

(b) airfoil and wing design by Jameson [42],[40],[41].

The computational cost of solving the adjoint equation is comparable to that of solving the flow equations. Thus the gradient is obtained with the computational cost of roughly two flow solutions. Further, since the adjoint equation is a partial differential equation very similar to the governing flow equations, it is possible to use a typical numerical discretization and acceleration schemes. To avoid violating constraints the gradient is projected into the allowable subspace. The current implementation is similar to recasting an inverse method as an optimization problem. In this particular reference every node on the boundary surface is considered a design variable (subject to certain smoothness criteria) and the gradient evaluated measures the sensitivity of the cost function to perturbation of each node. However, maximising L/D for a given L can also be specified as the target and not necessarily a pressure or velocity distribution.

This scheme has been employed to design airfoils and wings. In [41], a swept wing is designed by using the above technique. During design the wing planform was fixed and the wing itself was divided into 33 spanwise sections which were open to arbitrary changes subject to a minimum thickness criterion. Each section had 128 points, thus resulting in 4224 design variables. An initial wing section was designed using the two dimensional design method [42] to give a shock free flow at $M = 0.78$ with $C_L = 0.6$. Modified versions (in t/C) of this section were stacked to get the initial wing. The two-dimensional pressure distribution of the datum wing section was introduced as the target distribution uniformly over the span. The total inviscid drag was also included in the cost function. A multigrid based solver (FLO87) was used to solve the three dimensional Euler and costate equations. For computational efficiency only 15 multigrid iterations were used. Although the flow solution isn't fully converged, sufficiently accurate gradients can be obtained. At $M = 0.85$ and C_L close to 0.5 the inviscid C_D of the wing was reduced from 0.0207 to 0.0113. The shock present in the initial configuration was eliminated leaving a weak shock wave in the outboard region. The final configuration was analyzed by another code (FLO67), which was run to full convergence. This run predicted the C_D to be 0.0094 at $M = 0.85$ with $C_L = 0.5$, the L/D was 53. A typical design run required 10-20 design cycles (ie equivalent to 20-40 analysis runs).

A wing design can be performed overnight on a workstation. Current research topics include extension of the current method to include arbitrary meshes and to viscous flows.

2.7 The *One-Shot* Method

The one-shot method uses the Lagrangian multiplier with the introduction of a co-state equation. In that, the approach is identical to that discussed in section 2.1 (under "Adjoint Based Methods") and is governed by expressions (2.1–2.4) and (2.7–2.10). However, it differs from standard adjoint based methods in the way it uses acceleration schemes. Control theory based methods (section 2.6) use the simplest form of multigrid acceleration by treating the co-state equation like an additional flow equation but the *one-shot* method goes further by embedding the design process within the multigrid cycle and trying to accelerate gradient descent concurrent to the solution of the governing PDEs. This can be viewed as:

- Shape changes are carried out in a hierarchical manner such that smooth changes are performed on coarse grids while the high frequency changes are implemented on finer grids.
- Since different length scales are involved in these changes, for computational efficiency the governing equations can be solved on grids of appropriate resolution.

This leads to a series of optimization subproblems each on a given length scale. Such an approach circumvents the possible ill conditioning arising from optimizing on many scales simultaneously. The *One-Shot* method employs a full approximation scheme (FAS) full multigrid (FMG) algorithm. The prolongation is such that low frequency changes are updated in coarse grids and high frequency modes are updated in finer grids. The restriction ensures the optimization problem at each grid level is driven by the fine grid residual. This is schematically presented in fig 2.7 (pg 35).

The *One-Shot* method is computationally inexpensive, requiring a CPU time of about two analysis runs for each design cyle. As a part of the basic *One-Shot* design strategy, none of the design variables are updated on the finest grid. Additionally, because of the use of perturbation only on levels where they generate high frequency errors, a local relaxation around the airfoil is sufficient to damp out errors thus reducing computational costs. The *One-Shot* method has been applied to various airfoil design problems in [49].

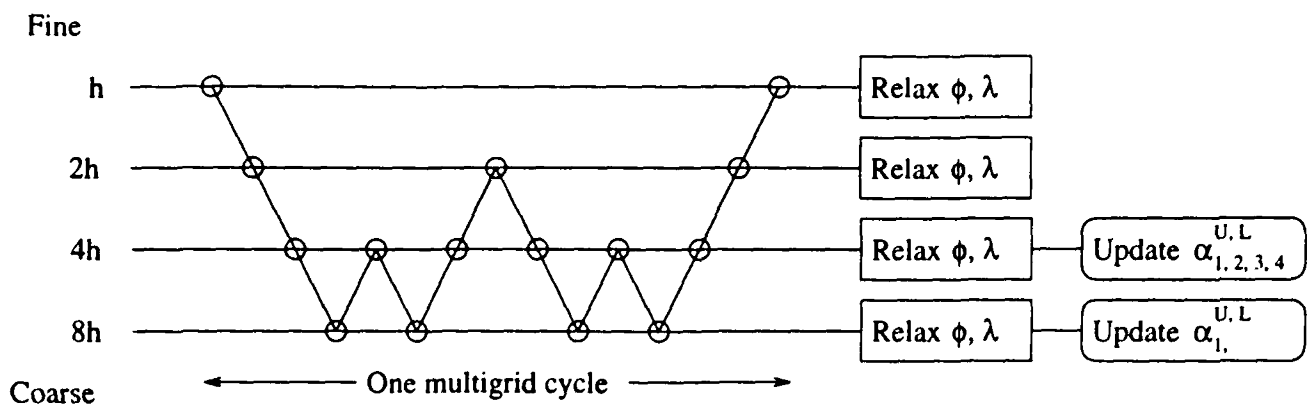

Figure 2.7: The *One-Shot* strategy.

2.8 Application of SA to CFD Shape Design

Concern that gradient based methods often get stuck in local minima and are not robust when discrete variables (such as material strength, or cost of manufacturing) are included has persuaded some research groups to investigate stochastic methods such as simulated annealing.

Aly et al [1] have studied the application of SA to CFD shape design with applications including minimisation of drag on airfoils and bodies of revolution in supersonic flow. Modifications to SA were included to reduce the number of objective function evaluations to levels similar to GB methods. They include:

- switching to an iterative improvement algorithm based on a normal distribution when the control parameter (annealing "temperature") becomes low
- using parallel SA when the temperature is high
- less stringent convergence criterion on flow solvers
- final convergence achieved by a GB method.

Typically SA has been applied to discrete problems (like the traveling salesman problem) and has been found to require many objective function evaluations (OFEs) to achieve a minimisation. By coupling a GB method to the

SA Aly et al wish to reduce the number of OFEs. The idea is quite simple. Once the metal being annealed becomes cool the actual changes to the crystal structure are quite small; in optimization terms this translates to an inability of the method to home into the minimum once it has reached its vicinity. However, GB methods are very good at doing this and a coupling of the two makes it possible for the SA to determine the region of interest while the GB method performs the final descent.

The parallelisation of SA was based on the idea that, if the metal started from reasonably high temperature nearly all crystals in the metal respond to the annealing process but in many different ways. As the system cools these many different states tend towards a common steady state dependent on the rate of cooling. By parallelising the SA design process, it is possible to vary the sequence of parameter changes thus calculating the cost functions and design variables simultaneously. This goes on till a transition point after which serial SA is pursued. The determination of the transition point is critical and is a current research topic. The communication overheads for the parallelisation involves only the evaluation of costs and design vectors and is negligible.

The current method has been applied to three different problems in [1]. One of them is to design an airfoil optimised for two different cruise Mach numbers ($M_\infty = 0.75$ and $M_\infty = 1.3$). To reflect the compromises, the objective was to minimise the average of the supersonic and subsonic drag. The dimension of the design vector was reduced to one by studying airfoils that were a linear combination of two base airfoils. The base airfoils may be referred to as the blunt and the sharp airfoils for ease. The design variable, called shape factor, controlled the combination of the two base airfoils. Having only one design variable makes the problem trivially parallelisable.

The minimum was obtained in 23 SA function evaluations performed over 4 computers. At the end of each design loop, the computers exchanged cost function values and design variables before each deciding to continue or stop (due to convergence).

It is also interesting to note that the authors have experimented with a drag based convergence criterion for flow solvers ie terminating the flow code when the mean deviation in average drag was below 10^{-5} over ten steps. Figure 2.8 (page 37) presents a comparison of drag computed with this criterion and from a fully converged (to machine precision) flow solution. The abscissa plots the difference in drag (in drag points) computed at the current shape factor (the ordinate) and shape factor = 0. There is a sufficient difference in the two

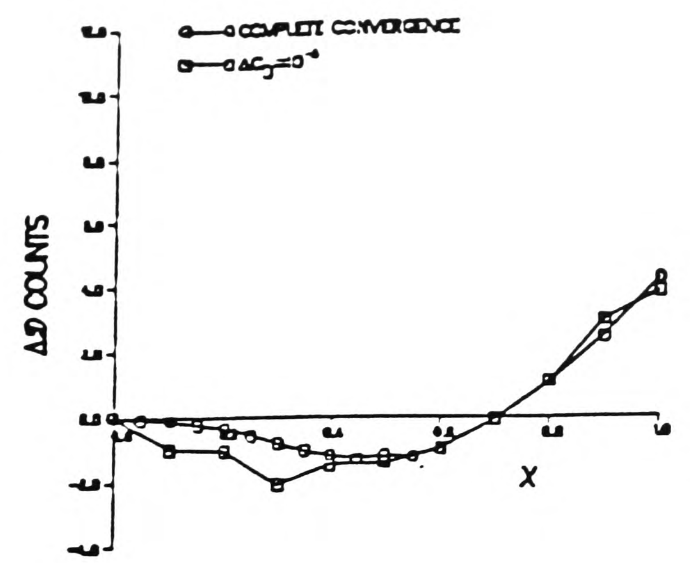

Figure 2.8: Average Drag vs Shape Factor, for convergence based on (a) drag and (b) residual at machine precision. Figure from [1].

curves to merit concern especially as the airfoil becomes sharper.

The gradient method used for comparison was likely to get stuck in any of the 3 local minima (depending on the initial conditions), while the SA method always found the global minimum.

Chapter 3

Design by Linear Sensitivities

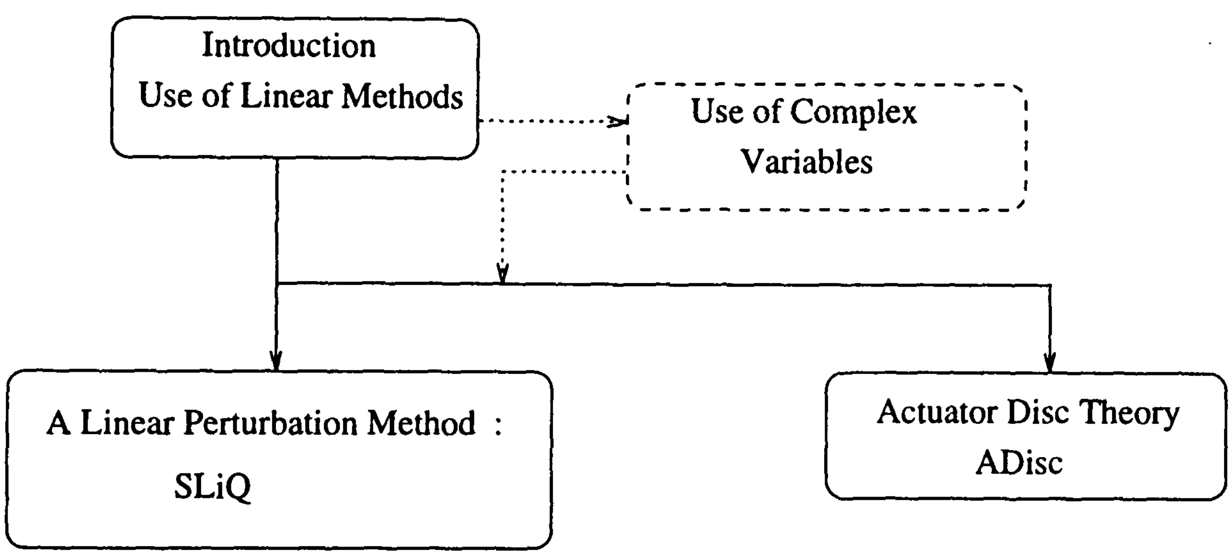

Figure 3.1: Flow chart of Chapter 3.

A mechanism to evaluate sensitivities from a linear perturbation method will be presented in this chapter. This is followed by a section on the application of actuator disc theory.

Numerical solution of linearized Euler equations was first discussed by Ni [58] in 1974 and a FEM was developed by Hall [37] in 1987. He demonstrated the validity of the linear approximation to substantial levels of unsteadiness. This, coupled with work on shock capturing by Lindquist and Giles [53], led to the development of SLiQ, the linear perturbation method used here.

In linear perturbation analysis for unsteady motion in cascades, the unsteady part of the flow solution can be expressed as the real part of a complex quantity of the form

$$\tilde{U}(x, y)\exp(i\omega t). \tag{3.1}$$

It is well-known that in linear unsteady analysis, the general solution can be decomposed into a sum of particular solutions satisfying the periodicity condition

$$\tilde{U}(x, y + P) = e^{i\phi}\tilde{U}(x, y), \tag{3.2}$$

where ϕ is known as the inter-blade phase angle and P is the blade pitch. The use of this equation as a periodic boundary condition allows the computation to be performed on a single blade passage, and then the solution in other passages can be reconstructed from

$$\tilde{U}(x, y + nP) = e^{in\phi}\tilde{U}(x, y). \tag{3.3}$$

This leads to considerable savings in computer time required. Linear methods are mainly used to study effects of flow unsteadiness on bending and torsional flutter. However, flutter analysis at zero frequency represents the linear sensitivity of the flow to changes in boundary conditions or blade geometry. It is this feature that we will utilise in this chapter. The accuracy of linear methods coupled with "cheap" sensitivities that can be output makes them very useful tools in a designers repertoire. They also serve as a good testbed for ideas that will later lead to a more complex design process. This chapter attempts to develop a system for redesign using sensitivities computed by a linear perturbation method.

3.1 A Linear Perturbation Analysis – SLiQ

SLiQ is a numerical method for the calculation of flows in multi-stage turbomachinery, developed by Giles [24] at MIT. SLiQ is an acronym for Steady/ Linear/ Quadratic, which refer to the first three terms of the asymptotic expansion that are computed in this method. In this code the unsteady, three dimensional Euler's equations are solved on a structured grid. The unsteady solution is assumed to have an asymptotic form. The first term of this expansion represents the nonlinear steady-state base flow. The second term is the linear perturbation to the base flow, in unsteady computations it has a zero time average, but in this work it gives the linear sensitivity of the steady flow to grid perturbations due to design changes. The third term, the quadratic term, reveals the change to the mean flow due to the time averaged effect of unsteadiness; it is not used in the current work. In the current work, SLiQ is executed in a 2D mode where the OGV row is modelled as a linear cascade.

It is assumed that there is no variation in either the geometry or the flow in the third dimension.

This approach is best demonstrated by considering the two dimensional Euler equations:

$$\frac{\partial U}{\partial t} + \frac{\partial F}{\partial x} + \frac{\partial G}{\partial y} = 0 \tag{3.4}$$

where the vectors U, F, G are

$$U = \begin{pmatrix} \rho \\ \rho u \\ \rho v \\ e \end{pmatrix}, \quad F = \begin{pmatrix} \rho u \\ \rho u^2 + p \\ \rho v u \\ \rho u h_0 \end{pmatrix}, \quad G = \begin{pmatrix} \rho u \\ \rho u v \\ \rho v^2 + p \\ \rho v h_0 \end{pmatrix} \tag{3.5}$$

and ρ, u, v, h_0 are the density, x component of velocity, y component of velocity and total enthalpy respectively. For an ideal gas with constant specific heats, the total enthalpy is:

$$h_0 = \frac{e+p}{\rho} = \frac{\gamma}{\gamma - 1}\frac{p}{\rho} + \frac{1}{2}(u^2 + v^2) \tag{3.6}$$

In SLiQ, the first step of the solution is to assume that there exists an unsteady solution $U(x,t)$ of the form

$$U(x,y,t) = U^{(0)}(x,y) + \epsilon U^{(1)}(x,y,t) + \epsilon^2 U^{(2)}(x,y,t) + \cdots \tag{3.7}$$

ϵ is some measure of the level of unsteadiness. The first term is the steady term, representing a nonlinear steady-state base flow. The second term is the linear term that represents the leading order nature of the unsteady solution, and has zero time average. The third term is the quadratic term whose time-average reveals the change to the mean flow due to the unsteadiness. In our present application, the third term is zero and so we shall use only the first two terms of the approximation:

$$U(x,y,t) = U^{(0)}(x,y) + \epsilon U^{(1)}(x,y,t) \tag{3.8}$$

In the next step, Taylor series expansions are used to express F and G as asymptotic functions. The basic Taylor series expansion is:

$$F(U^{(0)} + \delta U) \approx F(U^{(0)}) + \frac{\partial F^{(0)}}{\partial U_j}\delta U_j + \frac{1}{2}\frac{\partial^2 F^{(0)}}{\partial U_j \partial U_k}\delta U_j \delta U_k + \cdots \tag{3.9}$$

Using the above expansion $F(U)$ and $G(U)$ can be expressed as:

$$F\left(U^{(0)} + \epsilon U^{(1)} + \cdots\right) \approx \quad F(U^{(0)}) + \epsilon \frac{\partial F^{(0)}}{\partial U_j} U_j^{(1)} + \cdots \tag{3.10}$$

$$G\left(U^{(0)} + \epsilon U^{(1)} + \cdots\right) \approx \quad G(U^{(0)}) + \epsilon \frac{\partial G^{(0)}}{\partial U_j} U_j^{(1)} + \cdots \tag{3.11}$$

The above expressions are substituted back into the equations of motion and terms with the same power of ϵ are collected to form a set of asymptotic equations. The $O(1)$ terms give the standard, nonlinear, steady state equation.

$$\frac{\partial}{\partial x}\left(F(U^{(0)})\right) + \frac{\partial}{\partial y}\left(G(U^{(0)})\right) = 0 \tag{3.12}$$

The $O(\epsilon)$ terms produce an equation which is linear and homogeneous in $U^{(1)}$.

$$\frac{\partial U_i^{(1)}}{\partial t} + \frac{\partial}{\partial x}\left(\frac{\partial F^{(0)}}{\partial U_j} U_j^{(1)}\right) + \frac{\partial}{\partial x}\left(\frac{\partial G^{(0)}}{\partial U_j} U_j^{(1)}\right) = 0 \tag{3.13}$$

Because this is a linear equation with coefficients that are not time varying, $U^{(1)}$ can be expressed as a sum of components of the form $\hat{U}(x)\exp(-i\omega t)$. Thus different frequency components are mutually independent and satisfy the equation:

$$-i\omega\hat{U} + \frac{\partial}{\partial x}\left(\frac{\partial F^{(0)}}{\partial U_j}\hat{U}_j\right) + \frac{\partial}{\partial y}\left(\frac{\partial G^{(0)}}{\partial U_j}\hat{U}_j\right) = 0 \tag{3.14}$$

The $\frac{\partial}{\partial U_j}$ terms in the above equation represent linear sensitivities. In SLiQ, the linear equations are constructed on a deforming grid. These are derived from the nonlinear, unsteady Euler equations for a deforming control volume.

$$\begin{aligned} \frac{d}{dt}\iiint_V U dV &= \iint_{\partial V} U\dot{\vec{x}} \cdot d\vec{A} + \iiint_V \frac{\partial U}{\partial t} dV \\ &= -\iint_{\partial V}\left(\vec{F} - U\dot{\vec{x}}\right) \cdot d\vec{A} \end{aligned} \tag{3.15}$$

Here $\dot{\vec{x}}$ is the velocity of the deforming grid so the $\dot{\vec{x}} \cdot d\vec{A}$ is the rate at which new volume is being added to the control volume due to motion of the bounding surface. Following the SLiQ approach described earlier, it is assumed that the grid coordinates and the flow variables can be expressed as a sum of steady-state part plus a small amplitude unsteady perturbation.

$$\begin{aligned} \vec{x}(t) &= \vec{x}^{(0)} + \epsilon\vec{x}^{(1)}(\vec{x}^{(0)}, t), \\ U(\vec{x}(t), t) &= U^{(0)}(\vec{x}^{(0)}) + \epsilon U^{(1)}(\vec{x}^{(0)}, t). \end{aligned} \tag{3.16}$$

For convenience, the three coordinates of $\vec{x}$ and the five components of U can be expressed as a single eight-component entity called W. Thus the previous two equations can be expressed as

$$W(\vec{x}(t),t) = W^{(0)}(\vec{x}^{(0)}) + \epsilon W^{(1)}(\vec{x}^{(0)},t) \tag{3.17}$$

The superscript $^{(0)}$ can be dropped and the superscript $^{(1)}$ can be replaced with $\tilde{}$ for convenience. It is evident that perturbations to W will result in perturbation to all other terms. These perturbations can be expressed as

$$\tilde{\vec{F}} = \frac{\partial \vec{F}}{\partial W}\tilde{W} \tag{3.18}$$

and

$$\tilde{S} = \frac{\partial S}{\partial W}\tilde{W} \tag{3.19}$$

Where $\vec{F}$ and S are the flux and source terms respectively. The linear perturbation equations of unsteady integral equation of motion is

$$\frac{d}{dt}\iiint_V \tilde{U}dV + Ud\tilde{V} = -\iint_{\partial V}\left(\tilde{\vec{F}} - U\tilde{\dot{\vec{x}}}\right)\cdot d\vec{A} + \vec{F}\cdot d\tilde{\vec{A}} + \iiint_V \tilde{S}dV + Sd\tilde{V} \tag{3.20}$$

The terms $d\tilde{\vec{A}}$ and $d\tilde{V}$ represent the unsteady perturbations to the infinitesimal surface area vector and volume element. Since this equation is linear and all the coefficients depend on U and geometric terms, which do not vary in time, means that there are harmonic solutions of the form $U(x)\exp(-i\omega t)$. The most general periodic solution can be expressed as the real part of a linear superposition of such solutions for a number of different real frequencies ω, all satisfying the necessary periodicity constraints:

$$\tilde{U} = \mathcal{R}\left(\sum_{\omega} U_\omega \exp(-i\omega t)\right) \tag{3.21}$$

This was introduced in the beginning of this chapter. (equation 3.1).

3.1.1 Implementation

SLiQ as implemented by Giles [24] can operate in two different modes: the analysis and the design modes. In the analysis mode, the perturbation pressure field (the downstream disturbance) due to the pylon is specified through the exit boundary conditions. The discrete linear equations for the interior of the domain come from a natural linearisation of the nonlinear discrete equations coming from a standard finite volume discretization. This includes the linearisation of the solid wall boundary conditions on the OGV's. The inter-blade phase angle is specified, the complex flow solution is computed for the single passage, and then the real perturbation quantities can be reconstructed for any blade passage in a post-processing step.

In the design mode (see secn 5.5 for further details), the geometric perturbations of the OGV's define a consistent linear perturbation of the body-fitted computational grid. This introduces a source term into the discrete linear equations throughout the grid. Because the camber perturbation has cyclic periodicity, it is again possible to perform the calculation on a single blade passage by imposing the complex periodic boundary condition with the appropriate inter-blade phase angle. The design mode is executed without the downstream boundary condition imposing the pressure perturbation of the pylon. Instead, the goal is to determine the camber perturbation which generates an upstream flow perturbation equal in magnitude and opposite in sign to that produced by the pylon's interaction with the OGV's. Then, by linearity, the sum of the two solutions will give a combined flow solution corresponds to the presence of the pylon and the cyclically cambered OGV's and giving no flow perturbation upstream of the OGV's, (except for the very local pressure field associated with each OGV).

3.2 Actuator Disc Theory – ADisc

Actuator disc theory (ADisc) applies the small perturbation theory to the analysis of circumferential distortions in a cascade. It uses a wave form solution with a prescribed circumferential variation to evaluate the transmission of disturbances through the cascade. It has been used to design rotors subjected to circumferential flow distortions by Savell and Wells [65] and to design stators in the presence of an exit pressure distortion due to a downstream strut by Kodama and Nogano [48]. Additionally, there have been attempts to link ADisc and conventional CFD codes to study rotor-stator interaction [46] and [45]. In the current work, ADisc theory is used as an alternative to the linear perturbation code to examine the differences in the solutions due to the differing modeling assumptions. (see also, [72],[66],[67],[47])

In the actuator disc model we assume ...

1 Blade spacing is very small in comparison to the wavelength of the circumferential disturbance.

2 The cascade is assumed to consist of flat plate airfoils.

3 Flow deviation in the cascades is neglected.

4 Kutta Condition is assumed.

Because of assumption 1 it becomes possible to treat the flow in the cascade as a one-dimensional channel flow. Assumptions 2 and 4 result in sudden flow turning at the leading edge of the cascade. Streamline contraction also occurs at the leading edge of the cascade.

The flow field on either side of the cascade is governed by the linearised ideal, inviscid, isentropic compressible flow equation. The linearisation is based on the assumption that the perturbation quantities (denoted with a ˜ accent above the variable, as in $\tilde{p}$; mean quantities have a subscript 0 as in a_0) are small in comparison to the mean quantities. The equations are

Continuity

$$\frac{\partial \tilde{\rho}}{\partial t} + U\frac{\partial \tilde{\rho}}{\partial x} + V\frac{\partial \tilde{\rho}}{\partial y} + \rho_0\left(\frac{\partial \tilde{u}}{\partial x} + \frac{\partial \tilde{v}}{\partial y}\right) = 0 \tag{3.22}$$

Momentum

$$\rho_0\frac{\partial \tilde{u}}{\partial t} + \rho_0 U\frac{\partial \tilde{u}}{\partial x} + \rho_0 V\frac{\partial \tilde{u}}{\partial y} = -\frac{\partial \tilde{p}}{\partial x} \tag{3.23}$$

$$\rho_0\frac{\partial \tilde{v}}{\partial t} + \rho_0 U\frac{\partial \tilde{v}}{\partial x} + \rho_0 V\frac{\partial \tilde{v}}{\partial y} = -\frac{\partial \tilde{p}}{\partial y} \tag{3.24}$$

Energy

$$\frac{\partial}{\partial t}\left(\frac{\tilde{p}}{p_0} - \gamma\frac{\tilde{\rho}}{\rho_0}\right) + U\frac{\partial}{\partial x}\left(\frac{\tilde{p}}{p_0} - \gamma\frac{\tilde{\rho}}{\rho_0}\right) + V\frac{\partial}{\partial y}\left(\frac{\tilde{p}}{p_0} - \gamma\frac{\tilde{\rho}}{\rho_0}\right) = 0 \tag{3.25}$$

Where γ is $\frac{C_p}{C_v}$, U, V are the mean velocities in the x, y directions repspectively, ρ denotes the density and p is the pressure. The perturbations in pressure, density and velocity are assumed to be of the form

$$f = F_n \exp(\lambda x)\exp(i\omega t + iky) \tag{3.26}$$

where $\omega = -kV_s$, $k = \frac{2\pi}{L}$, L is the pitch of the disturbance (pylon), $a_0 = \sqrt{\frac{\gamma p_0}{\rho_0}}$ and λ = decay constant in X direction. V_s is the velocity of rotor rotation.

Since we are only concerned with OGVs (stators), $V_s = 0$. Eqn (3.26) can be written as

$$f = F_n \exp(\lambda x)\exp(iky) \tag{3.27}$$

At this point it is necessary to note that the disturbances are sinusoidal along the annulus. Therefore, it is possible to rewrite the wave form of the disturbance (eqn(3.27)) as

$$f = \hat{f}\exp(iky) \tag{3.28}$$

The $\exp(iky)$ term in the above equation simulates the sinusoidal nature of the disturbance along the annulus. Further algebra can be performed without the $\exp(iky)$ term (ie. using $\hat{f}$ instead of f) for simplicity. The two values of λ for which such solutions exist are

$$\lambda_1 = \frac{k}{1-M_x^2}\{iM_xM_y + \sqrt{1-M_x^2-M_y^2}\} \tag{3.29}$$

$$\lambda_2 = \frac{k}{1-M_x^2}\{iM_xM_y - \sqrt{1-M_x^2-M_y^2}\} \tag{3.30}$$

where M_x and M_y refer to Mach numbers in the x and y directions respectively. Since the real part of λ_1 is positive, the corresponding flow solution has an exponential increase in the axial direction, whereas the real part of λ_2 is negative and so its corresponding flow solution has an exponential decrease in the axial direction.

A general flow solution with the required circumferential periodicity is a sum of an arbitrary multiple of each of these two flow solutions. Perturbations in the pressure, density and velocity components can be related to the potential solution to obtain the following expressions, in which C_1 and C_2 are complex constants giving the arbitrary amplitudes of the two component modes.

$$\frac{\hat{p}}{p_0} = \{C_1\exp(\lambda_1 x) + C_2\exp(\lambda_2 x)\} \tag{3.31}$$

$$\frac{\hat{\rho}}{\rho_0} = \frac{1}{\gamma}\{C_1\exp(\lambda_1 x) + C_2\exp(\lambda_2 x)\} \tag{3.32}$$

$$\frac{\hat{u}}{a_0} = -\left\{\frac{\frac{\lambda_1}{k}}{M_x\left(\frac{\lambda_1}{k}\right)+iM_y}C_1\exp(\lambda_1 x) + \frac{\frac{\lambda_2}{k}}{M_x\left(\frac{\lambda_2}{k}\right)+iM_y}C_2\exp(\lambda_2 x)\right\}\frac{1}{\gamma} \tag{3.33}$$

$$\begin{aligned}\frac{\hat{v}}{a_0} &= -\left\{\frac{i}{M_x\left(\frac{\lambda_1}{k}\right)+iM_y}C_1\exp(\lambda_1 x)+\right.\\ &\left.\frac{i}{M_x\left(\frac{\lambda_2}{k}\right)+iM_y}C_2\exp(\lambda_2 x)\right\}\frac{1}{\gamma}\end{aligned} \tag{3.34}$$

The actual physical perturbation is always the real part of the complex quantity given in these equations. The complex representation can be viewed here as simply a convenience to simplify the construction of the general solution. It is however a fundamental aspect of the linear perturbation code, SLiQ. To understand this it is helpful at this point to note that one feature of the complex solution to the potential flow equation, and the associated perturbation flow variables is that

$$U(x, y+\Delta y) = e^{i\phi}U(x,y), \qquad \phi = k\,\Delta y \tag{3.35}$$

Here, U can be viewed either as the complex potential Φ, or as the vector of perturbed quantities $(\tilde{p}, \tilde{\rho}, \tilde{u}, \tilde{v})$. Because of this periodicity feature, the same flow solution would have been obtained if the perturbation equations of motion were solved on the strip $0 \leq y \leq \Delta y$ with the periodic boundary condition

$$U(x, \Delta y) = e^{i\phi}U(x,0), \qquad \phi = k\,\Delta y \tag{3.36}$$

This, in essence, is how the linear perturbation code SLiQ operates.

Analysis of λ reveals that C_1 terms decay in the upstream direction while the C_2 terms decay in the downstream direction. (See fig3.2). In the test case adopted for this thesis there is no imposed upstream disturbance that decays downstream towards the actuator disc. Therefore C_{2u}, the value of C_2 upstream of the actuator disc is zero. The expressions for p, ρ, u and v can be written independently for upstream and downstream as follows.

3.2.1 Equations for Flow Upstream of the Disc

If the subscript u is used to denote upstream terms, the expressions (3.31-3.34) can be rewritten as

$$\frac{\hat{p}_u}{p_{0u}} = \{C_{1u}\exp(\lambda_{1u}x)\} \tag{3.37}$$

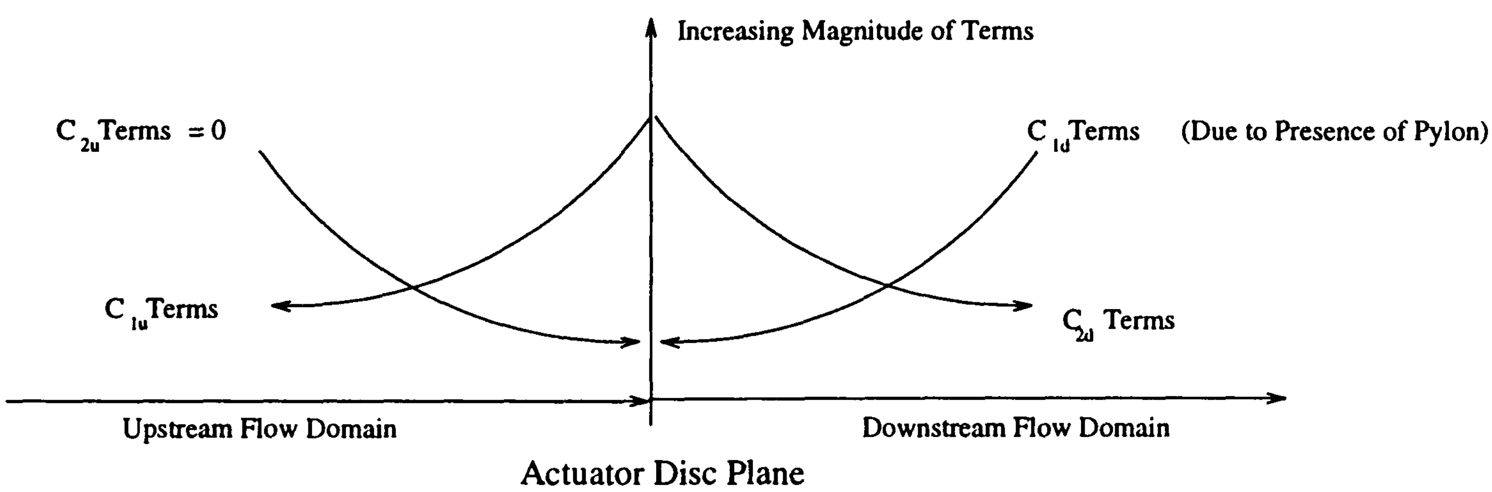

Figure 3.2: Variation of distortion terms upstream and downstream of the Actuator Disc Plane

$$\frac{\hat{\rho}_u}{\rho_{0u}} = \frac{1}{\gamma}\{C_{1u}\exp(\lambda_{1u}x)\} \tag{3.38}$$

$$\frac{\hat{u}_u}{a_{0u}} = \left\{-\frac{1}{\gamma}\frac{\frac{\lambda_{1u}}{k}}{M_{xu}\left(\frac{\lambda_{1u}}{k}\right)+iM_{yu}}C_{1u}\exp(\lambda_{1u}x)\right\} \tag{3.39}$$

$$\frac{\hat{v}_u}{a_{0u}} = \left\{-\frac{1}{\gamma}\frac{i}{M_{xu}\left(\frac{\lambda_{1u}}{k}\right)+iM_{yu}}C_{1u}\exp(\lambda_{1u}x)\right\} \tag{3.40}$$

where

$$\lambda_{1u} = \frac{k}{1-M_{xu}^2}\{iM_{xu}M_{yu}+\sqrt{1-M_{xu}^2-M_{yu}^2}\} \tag{3.41}$$

$$\tag{3.42}$$

3.2.2 Equations for Flow Downstream of the Disc

Similarly, if the subscript d is used to denote downstream terms, the expressions (3.31-3.34) can be rewritten as

$$\frac{\hat{p}_d}{p_{0d}} = \{C_{1d}\exp(\lambda_{1d}x)+C_{2d}\exp(\lambda_{2d}x)\} \tag{3.43}$$

$$\frac{\hat{\rho}_d}{\rho_{0d}} = \frac{1}{\gamma}\{C_{1d}\exp(\lambda_{1d}x)+C_{2d}\exp(\lambda_{2d}x)\} \tag{3.44}$$

$$\frac{\hat{u}_d}{a_{0d}} = \left\{-\frac{1}{\gamma}\frac{\frac{\lambda_{1d}}{k}}{M_{xd}\left(\frac{\lambda_{1d}}{k}\right)+iM_{yd}}C_{1d}\exp(\lambda_{1d}x) -\frac{1}{\gamma}\frac{\frac{\lambda_{2d}}{k}}{M_{xd}\left(\frac{\lambda_{2d}}{k}\right)+iM_{yd}}C_{2d}\exp(\lambda_{2d}x)\right\} \tag{3.45}$$

$$\frac{\hat{v}_d}{a_{0d}} = \left\{-\frac{1}{\gamma}\frac{i}{M_{xd}\left(\frac{\lambda_{1d}}{k}\right)+iM_{yd}}C_{1d}\exp(\lambda_{1d}x) -\frac{1}{\gamma}\frac{i}{M_{xd}\left(\frac{\lambda_{2d}}{k}\right)+iM_{yd}}C_{2d}\exp(\lambda_{2d}x)\right\} \tag{3.46}$$

where

$$\lambda_{1d} = \frac{k}{1-M_{xd}^2}\{iM_{xd}M_{yd}+\sqrt{1-M_{xd}^2-M_{yd}^2}\} \tag{3.47}$$

$$\lambda_{2d} = \frac{k}{1-M_{xd}^2}\{iM_{xd}M_{yd}-\sqrt{1-M_{xd}^2-M_{yd}^2}\} \tag{3.48}$$

3.2.3 Boundary Conditions

The above expressions define the flow fields on either side of the actuator disc. They can be evaluated all over the domain once C_{1u}, C_{1d} and C_{2d} are known. These are determined by introducing the following boundary conditions:

- Pressure wave downstream of actuator disc (due to the Pylon).
- Flow angle at exit of the actuator disc.
- Conservation of mass.

Effect of Downstream Pylon

The downstream disturbance that propagates in the upstream direction is exclusively due the presence of the pylon. If there is no pylon disturbance then C_{1d} is zero. For the cases in this thesis involving a pylon, C_{1d} is calculated from a nonlinear calculation of the steady flow around the pylon alone. This calculation is performed using the program UNSFLO which solves the 2D Euler equations on unstructured grids [21].

From the nonlinear results, a line plot of pressure at $x = X_{te}(\mathrm{OGV})$, the location of the trailing edge of the OGV's, has the form shown in figure 5.6. Using Fourier series, this can be represented as

$$p(y) = p_0 + \mathcal{R}\left(\sum_{n=1}^{\infty} \hat{P}_n \exp(inky)\right) \tag{3.49}$$

Equating the first harmonic to the pressure perturbation due to C_{1d} gives

$$C_{1d} = \frac{\hat{P}_1}{p_{0d}\exp(\lambda_{1d}x)} \tag{3.50}$$

Exit Angle of Flow from the Actuator Disc

C_{2d} can be determined by relating the exit flow angle (at the actuator disc) to $\tilde{u}$ and $\tilde{v}$.

$$\tan(\alpha + \tilde{\alpha}) = \frac{M_{yd} + \frac{\tilde{v}}{a_{0d}}}{M_{xd} + \frac{\tilde{u}}{a_{0d}}} \tag{3.51}$$

where α is the mean flow angle (see figure 3.3), $\tilde{\alpha}$ is the angular perturbation at the exit from the actuator disc. This can be expanded as

$$\left(M_x + \frac{\tilde{u}}{a_{0d}}\right)\left(\tan(\alpha) + \tilde{\alpha}\sec^2(\alpha)\right) = M_y + \frac{\tilde{v}}{a_{0d}} \tag{3.52}$$

Collecting the first order terms gives,

$$\frac{\tilde{u}}{a_{0d}}\tan(\alpha) + M_x\tilde{\alpha}\sec^2(\alpha) = \frac{\tilde{v}}{a_{0d}} \tag{3.53}$$

The $\tilde{\alpha}$ term is determined from the deflection to the blade geometry defined from the SLiQ-aided redesign. This is sinusoidal along the annulus and can be written as

$$\tilde{\alpha} = \hat{\alpha}\exp(iky) \tag{3.54}$$

$\hat{\alpha}$ is the "tailoring" to the trailing edge specified as a result of the redesign. C_{1d} is known therefore, from the above equation C_{2d} can be evaluated as

$$C_{2d} = \frac{M_{xd}\hat{\alpha}\sec(\alpha)^2 + C_{1d}\left(\tan(\alpha)CA - CC\right)\exp(\lambda_{1d}x)}{\left(CD - CB\tan(\alpha)\right)\exp(\lambda_{2d}x)} \tag{3.55}$$

where

$$\begin{aligned}
CA &= -\frac{1}{\gamma}\frac{\frac{\lambda_{1d}}{k}}{M_{xd}\left(\frac{\lambda_{1d}}{k}\right) + iM_{yd}} \\
CB &= -\frac{1}{\gamma}\frac{\frac{\lambda_{2d}}{k}}{M_{xd}\left(\frac{\lambda_{2d}}{k}\right) + iM_{yd}} \\
CC &= -\frac{1}{\gamma}\frac{i}{M_{xd}\left(\frac{\lambda_{1d}}{k}\right) + iM_{yd}} \\
CD &= -\frac{1}{\gamma}\frac{i}{M_{xd}\left(\frac{\lambda_{2d}}{k}\right) + iM_{yd}}
\end{aligned} \tag{3.56}$$

The above expressions are evaluated at $x = 0$, so the $\exp(\lambda x)$ terms are reduced to 1.

Conservation of Mass

C_{1u} can be determined from the conservation of mass.

$$\hat{\rho}_u U_u + \hat{u}_u \rho_u = \hat{u}_d \rho_d + \hat{\rho}_d U_d \tag{3.57}$$

From this equation C_{1u} can be evaluated as

$$C_{1u} = \frac{\hat{u}_d \rho_d + \hat{\rho}_d U_d}{\exp(\lambda_1 x_u)\left(\frac{\rho_{0u} a_{0u}}{\gamma}\right)\left(M_{xu} - \frac{\frac{\lambda_{1u}}{k}}{M_{xu}(\frac{\lambda_{1u}}{k}) + iM_{yu}}\right)} \tag{3.58}$$

This is evaluated at the actuator disc.

3.2.4 Thick Actuator Disc

The preceding sections describe the equations governing a flow around a thin actuator disc (where the actuator disc is a line on which the flow variables suddenly change). In our present study the perturbations upstream and downstream travel only the distance of about 1 chord length of the OGV blade. So consideration must be given towards modeling the distance of decay in relation to thickness of the blade. The thick actuator disc (see fig 3.3) accounts for the decay in the regions outside the trailing and leading edges. There is no decay within the disc. There is a slight phase shift when the disturbance appears on the upstream flow field. This is due to the shape of the blade passages. This is included as a $\exp(ik\ \delta y)$ term. The boundary conditions are, therefore, implemented by substituting $x - x_{te}$ for the downstream components and $x - x_{le}$ in the upstream terms in equations (3.37)-(3.46). For example eqn (3.37) is rewritten as:

$$\frac{\tilde{p}_u}{p_{0u}} = \{C_{1u} \exp(\lambda_{1u} x)\} \exp(iky) \exp(ik\ \delta y) \tag{3.59}$$

The resulting equations (for a thick actuator disc) are used in the following chapter to validate the results obtained from SLiQ and UNSFLO. It is implemented in a computer program which requires as input

(a) the magnitude of the pylon induced pressure perturbation (at $x = 264$)

(b) the variation of trailing edge angle of the OGV's.

The constants C_{1u}, C_{1d} and C_{2d} are computed and the pressure is plotted for any required x coordinate. When used in the inverse mode with the pylon induced pressure field at $x = 264$ the program calculates the necessary variation in the flow exit angle from the OGV's to achieve total suppression of the disturbance upstream of the OGV's. These results are used as comparisons in the runs described in the following sections. In all subsequent sections the term ADisc will refer to the thick actuator disc analysis.

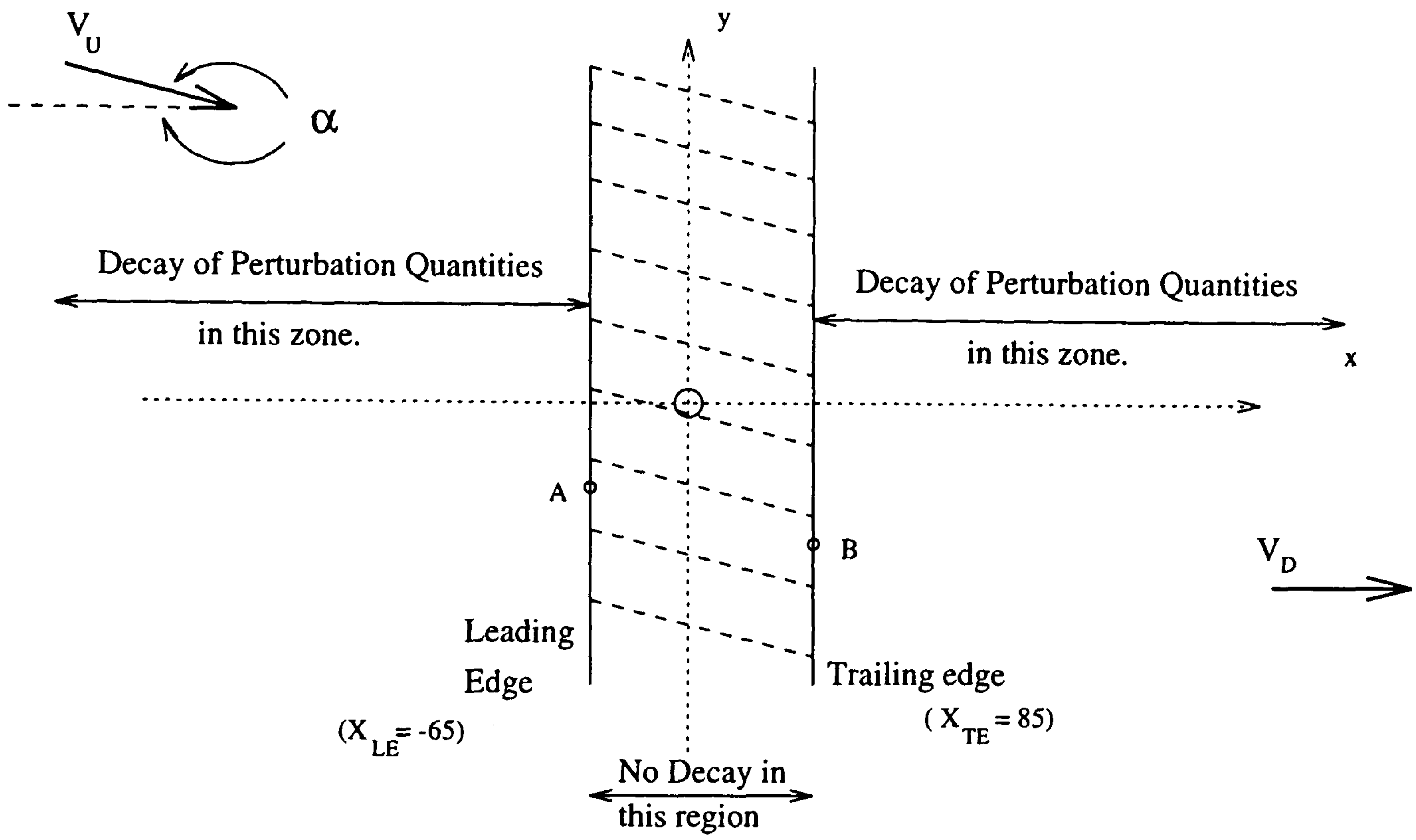

Figure 3.3: Thick Actuator Disc

3.2.5 Special Cases

The above equations and boundary conditions are complete. However, there are two special cases where solutions are required.

a Upstream flow field has no perturbation.

b Upstream influence due to stator tailoring.

Case [a] is evaluated by setting the upstream flow field to have no perturbations, ie. $C_{1u} = 0$. First C_{1d} is determined from the pylon pressure field. Then using the mass conservation equation determine C_{2d}. With this the downstream flow field is fully defined and the trailing edge exit angle perturbation can be determined.

Case [b] can be evaluated by setting $C_{1d} = 0$. The given disc exit angle function is used to determine C_{2d}. With the conservation of mass equation and C_{2d}, C_{1u} is determined.

Chapter 4

Design by Non Linear Sensitivities

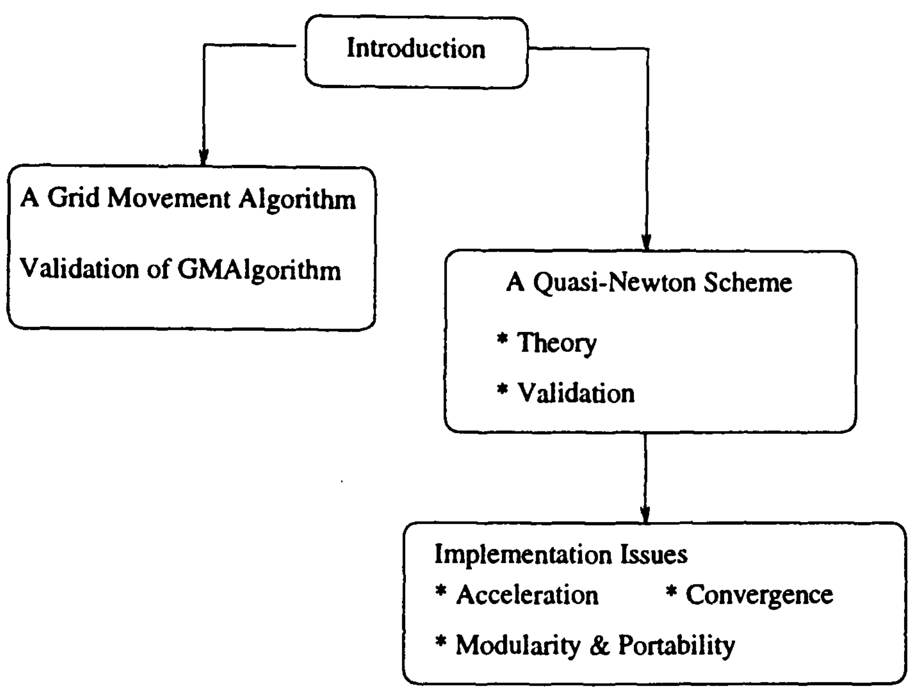

Figure 4.1: Flow chart of Chapter 4.

4.1 Introduction

The test problem in this thesis requires minimisation of pressure variation upstream of the OGV row. This can be expressed as minimisation of the mismatch integral I, where I is:

$$I = \frac{1}{2}\int_Y (p - p_{specified})^2 dy.$$

For the test problem, $p_{specified}$ is replaced by the mean pressure p_{mean}.

Minimisation of I was attempted in the previous chapter using linear sensitivities. However, such methods are useful only for a small class of problems. For a more general design method an optimisation based design approach is needed; this approach can rely on a wide variety of (gradient based) GB or (non-gradient based) NGB optimisers to perform the minimisation. At present we are interested in the minimisation of a quadratic functional, and most gradient based optimisation routines are well suited for this application. We shall use a finite difference method to obtain sensitivities and then use a quasi-Newton based descent technique to determine the new location in design space. The overall approach resembles the method described in section 2.1.1. The validation of this design method will be performed on a simple design problem involving the ONERA M6 wing. In subsequent chapters, this method will used to redesign two and three dimensional blade rows. Further, we will also investigate ways to accelerate the design process by reducing its reliance on well converged flow solutions to calculate sensitivities.

The minimisation of the cost function can be performed using either a GB method or a NGB method (as discussed in Chapter 2). In either case, for a successful design method we need the following:

(a) A robust grid generator to obtain a grid about the datum geometry,

(b) a robust and fast flow solver, and

(c) a robust grid movement algorithm.

As a part of the design process, the geometry has to be altered often and the flow field re-evaluated. However, most changes are minor and do not merit a complete regridding of the geometry; regridding is expensive and often require human interaction to produce a good grid. A better approach is to use a fast and robust grid movement algorithm that can implement geometric perturbations suggested by the design code.

The flow solver is then used to compute the flow field around the new geometry. NGB methods perform a series of such operations to obtain a general idea about the behaviour of the cost function over design space and then seek to determine the minima. In contrast, finite difference based GB methods obtain a flow solution over the present design and then perturb the geometry and obtain a new flow solution. The two solutions are differenced to determine the sensitivity of the cost function to geometric perturbations. Based on this sensitivity a new design point is determined.

The evolution of the design from the datum cannot be predicted and often optimisers may need to evaluate extreme geometries before rejecting them. The flow solver should be capable of tolerating extreme cases and still providing flow solutions, even if this is achieved at the expense of a slight loss in accuracy. While, this need not be critical, the loss of accuracy has to be acknowledged by the designer. During the course of this work we will be using an Euler solver by Crumpton [13],[12].

4.2 A Grid Movement Method

In work initiated in September 1994 a grid movement algorithm was developed. The aim of the grid movement method (GMM) is to perturb the coordinates of the grid nodes of the original configuration to obtain a valid grid for the new configuration. Such methods are required not only in design but also in unsteady flow simulations [14]. It is assumed by these methods that the initial and final geometries are fairly similar and it is easier to modify the original mesh than to generate a new one.

Modifications to the geometry will be specified as a displacement to surface nodes while far field nodes remain unperturbed. The GMM has to preserve the shape and density of the grid close to the body surface while far field cells may undergo distortions. This also assumes that the original grid quality is maintained in the new grid. Further, it will be an added bonus if the same algorithm can be applied in two and three dimensions. The GMM can maintain grid quality if it has good smoothing qualities. It is assumed that the product of the GMM is a grid whose connectivity and boundary information are unchanged and all its cells have positive volumes (such a grid is called a "valid" grid).

Grid movement has been attempted in the past using a spring analogy [3]. This approach can be used in two and three dimensions and involves representing all edges as springs. The stiffness coefficient ($k_{i,j}$) associated with an edge $(i-j)$ is inversely proportional to its length,

$$k_{i,j} = \frac{1}{[(x_i - x_j)^2 + (y_i - y_j)^2 + (z_i - z_j)^2]^{\frac{1}{2}}}. \tag{4.1}$$

This results in small edges being very stiff, ie. more likely to translate rather than undergo compression or expansion. The actual displacement of each node is computed in [3] using a predictor-corrector procedure. During the predictor step displacements of the nodes are computed by extrapolation from grids at previous time levels. In the corrector phase, several Jacobi iterations of the static equilibrium equations (equating the summation of spring forces on a node to be equal to zero) are performed.

Another idea is to use Laplace's equation to define a smooth grid movement function for interior grid nodes given the perturbations to the surface nodes. A merit of this form of grid movement is that Laplace solvers are readily available in 2D, 3D. High performance computing techniques such as multigrid and parallel processing can be easily included to achieve better performance. The grid movement algorithm using Laplace's equation can be written as:

$$\begin{aligned} \nabla^2 \tilde{x} &= 0 \\ \nabla^2 \tilde{y} &= 0 \\ \nabla^2 \tilde{z} &= 0 \end{aligned} \tag{4.2}$$

where $\tilde{x}, \tilde{y}, \tilde{z}$ are the perturbations in the x, y, z directions respectively. $\tilde{x}, \tilde{y}, \tilde{z}$ are specified on the body surface and are zero on the far field boundaries.

However, there are problems associated with using the Laplace equation. It may be recalled that in a scalar field which conforms to the Laplace equation, the gradients are steepest at the boundary.

A point x is perturbed to the new mesh by:

$$x \longrightarrow x + \tilde{x}(x) \tag{4.3}$$

where $\tilde{x}$ is the perturbation computed (and is therefore a function of x). At a neighbouring point:

$$(x + dx) \longrightarrow (x + dx) + \tilde{x}(x + dx) \tag{4.4}$$

which implies:

$$dx \longrightarrow dx\left(1 + \frac{d\tilde{x}}{dx}\right) \tag{4.5}$$

When the above scheme is used with the Laplace equation

$$\frac{d\tilde{x}}{dx} = \text{const} \tag{4.6}$$

ie. the perturbation is a linear function. This implies that there is a constant scaling of all cell through out the entire grid. This creates problems with grid movement. Since the gradients are steepest at the boundaries, cells close to the body surface (also a boundary) are subject to steep gradients. Similarly cells in the far field are also subject to steep gradients and constant scaling, however, cells in the far field are large enough to absorb the steep gradients with changes in their volumes. But, the small cells around the body surface are more prone to inversion and thus result in negative volumes (ie. an invalid grid).

This can be overcome by rewriting equation (4.5) so that there is a factor $\alpha(x)$ to compensate for the steep gradients where they exist:

$$dx \longrightarrow dx\left(1 + \alpha\frac{d\tilde{x}}{dx}\right) \tag{4.7}$$

In the Laplace equation, the required non-linearity can be introduced by using the heterogeneous steady state heat conduction equation:

$$\nabla \cdot (k\nabla\phi) = 0 \tag{4.8}$$

where k is the conductivity of the material and is a function of x, y, z and mimics $\alpha(x)$.

In the solution of equation (4.8), in 2D and 3D, the value of k at a cell, k_{cell}, is set as being equal to the inverse of the *current* cell volume (area in 2D). This leads to small cells acquiring large conductivity, ie. will translate rather than squash. To remedy situations where cell volumes are negative, k is computed by a maximum principle:

$$k_{\text{cell}} = \frac{1}{\max(CellVolume, O\_G\_MinVol)} \tag{4.9}$$

where O_G_MinVol is the smallest cell volume in the unperturbed grid.

4.2.1 Validation of the Grid Movement Algorithm

The GMM was implemented in an existing Laplace solver in 2D and 3D. The Laplace solver was a standard Galerkin finite volume discretization with a

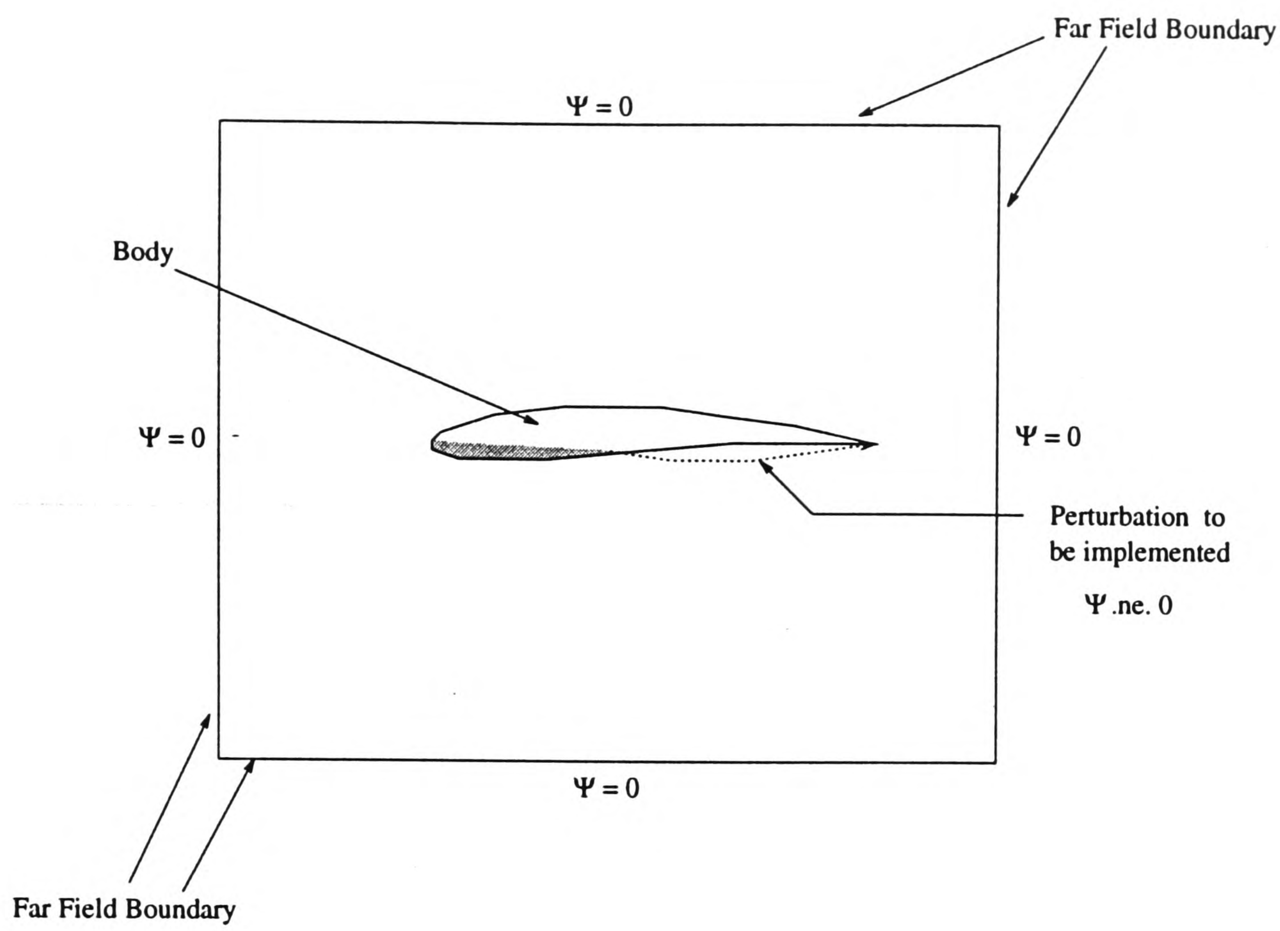

Figure 4.2: Scheme of the GMM demonstrated in 2D.

Jacobi relaxation and included a multigrid routine. It was found through experience that the success of the grid movement method (especially on fine meshes) was dependent on a good initial guess. This was because a good guess facilitated a quick untangling of the moved mesh, a full multigrid startup was used to provide a good initial guess.

The grid movement method (GMM) was tested independently in 2D and 3D. The tests, which were designed to be extreme to verify the robustness of the method, included:

2D: Transforming an NACA 0012 airfoil to a circle The initial and final computational domains are shown in figure 4.3. The initial grid is around a NACA 0012 airfoil in a circular domain. The airfoil itself is surrounded by a dense grid (see figure 4.4(a)) with the far field being dominated by large cells (the grid had 7748 triangles with 3992 nodes). The GMM is required to transform this initial grid to a grid about the displaced circle shown in figure 4.3(b). The GMM produced a valid grid that retained the original grid quality in all regions except near the leading edge (see figure 4.4(b)). The distortions near the leading edge can be attributed to the fact that we do not allow the points on the airfoil surface to slide along the surface. If this was permitted then the points would acquire a more homogeneous distribution along the circle's surface and the distortion would be smoothed out. Since such extreme cases are not expected as a part of the design method, implementation of the sliding criterion was not considered important.

3D: Aircraft subjected to pitching To demonstrate the GMM in three dimensions, a conventional two engine airliner was subjected to pitch (figure 4.5). The grid contained 330K tetrahedral cells with 58K nodes and was pitched by 15°. A cutting plane through the engine nacelle is used to display the quality of the initial and final grids in figure 4.6.

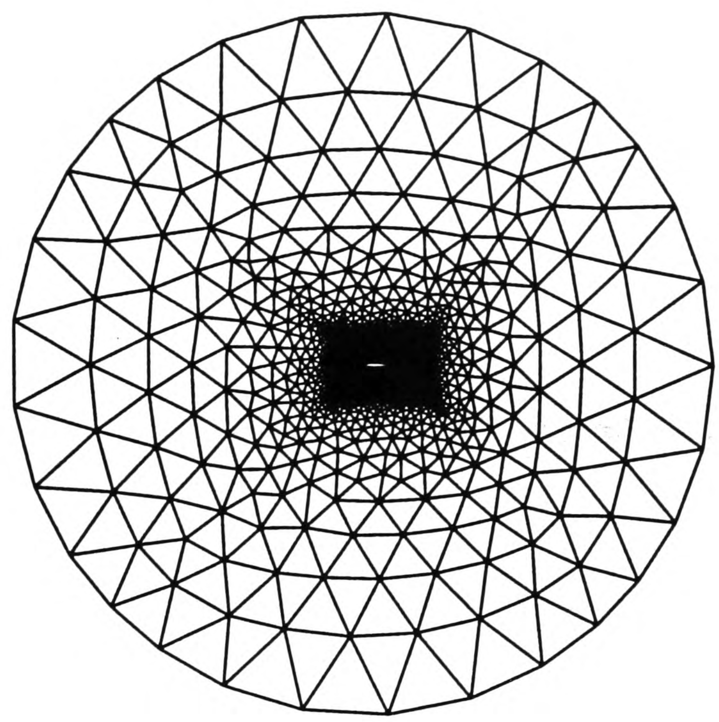

(a) Initial grid (a NACA 0012 airfoil)

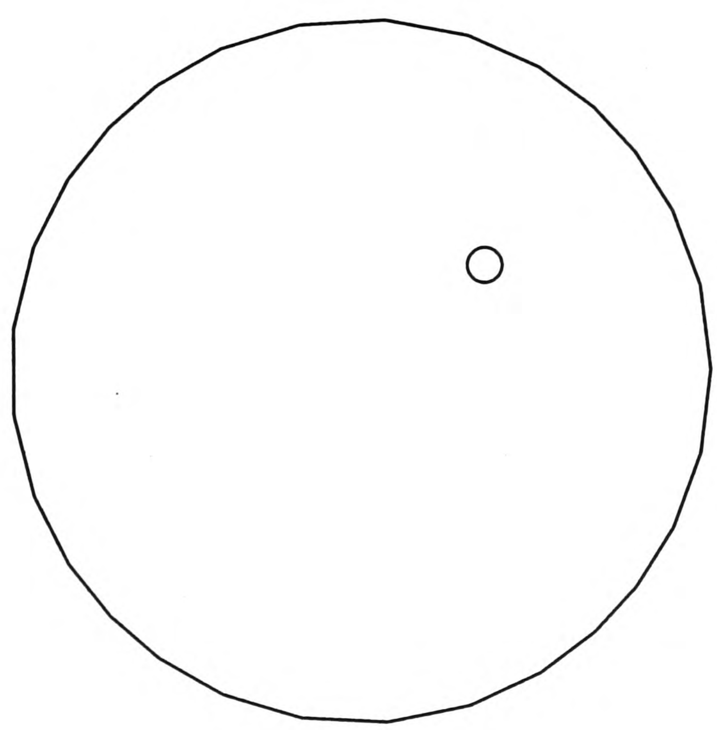

(b) Final Configuration (a displaced circle)

Figure 4.3: Illustration of the 2D grid movement capability.

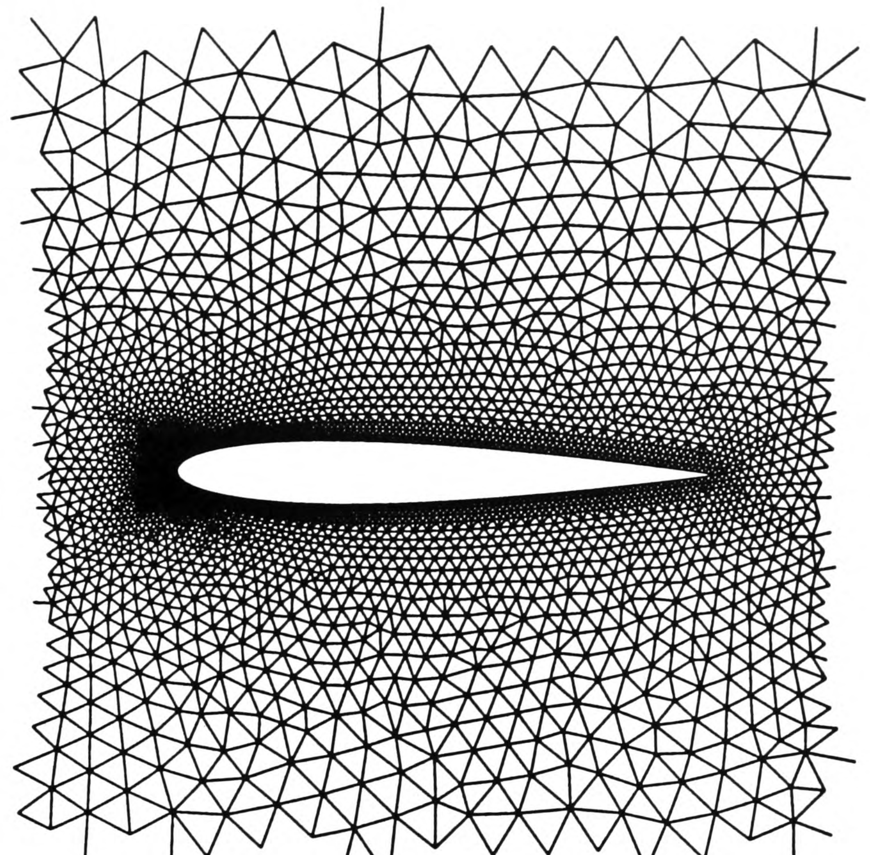

(a) Close up view of the NACA 0012 airfoil in the initial grid.

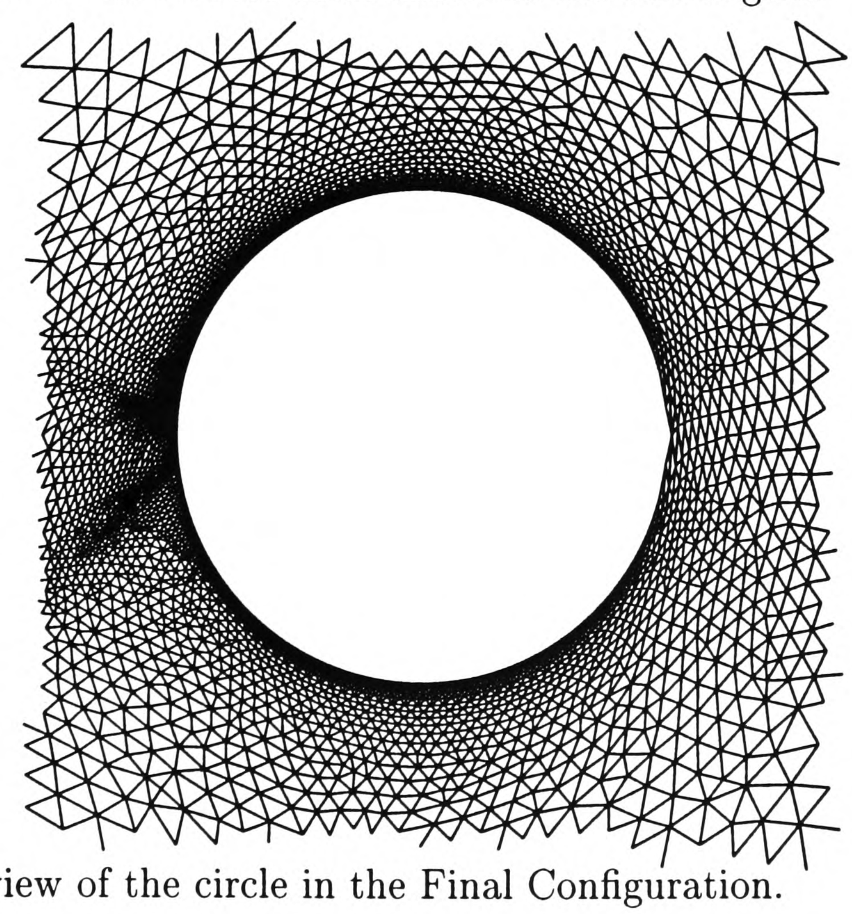

(b) Close up view of the circle in the Final Configuration.

Figure 4.4: Illustration of smoothness of the 2D grid movement method. The distortions correspond to the rapid changes in grid density close to the leading and trailing edges.

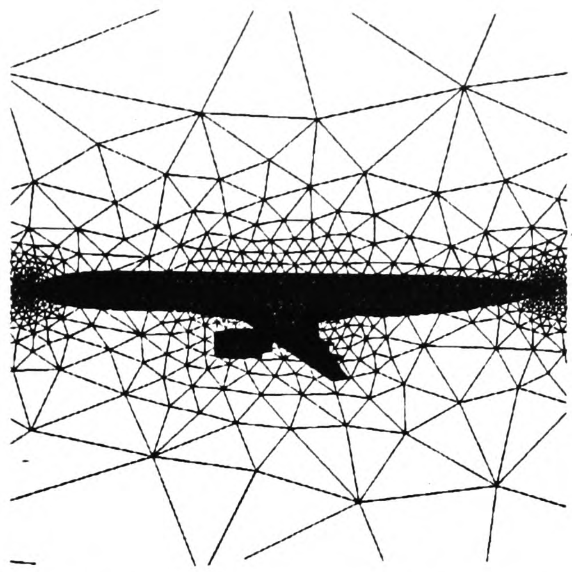

(a) Aircraft surface and symmetry plane in initial grid.

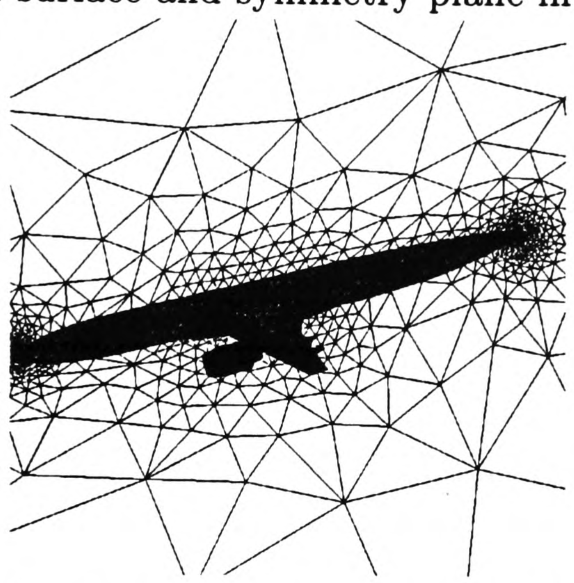

(b) Aircraft surface and symmetry plane in grid pitched down.

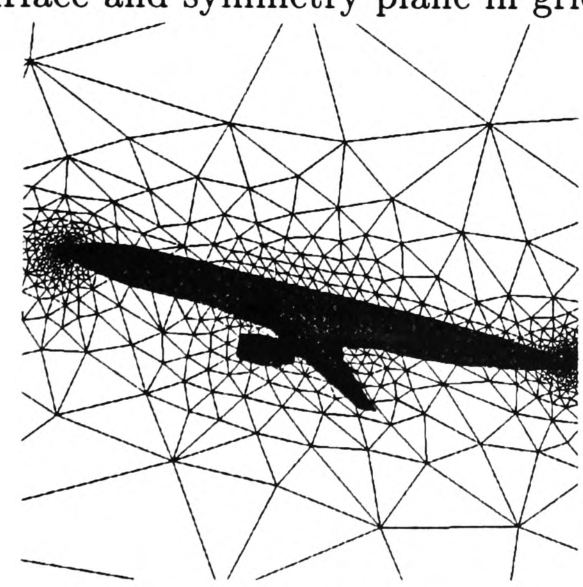

(c) Aircraft surface and symmetry plane in grid pitched up.

Figure 4.5: Illustration of the 3D grid movement method.

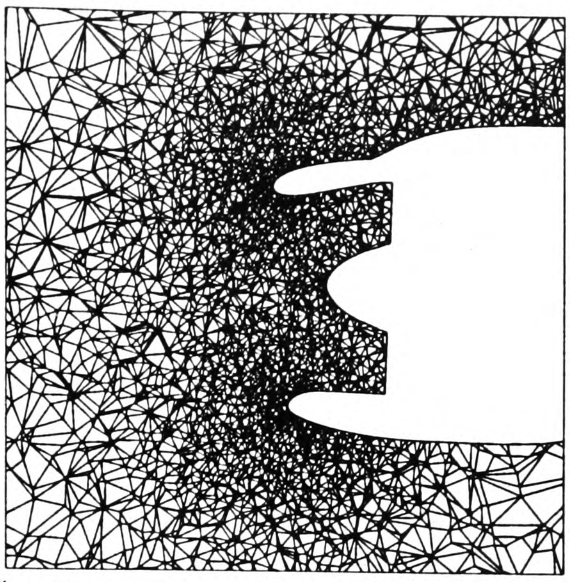

(a) Cutting plane through the initial grid.

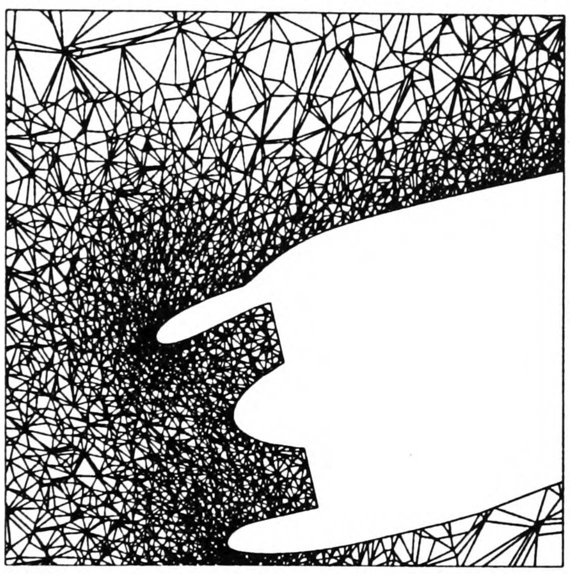

(b) Cutting plane though grid pitched down.

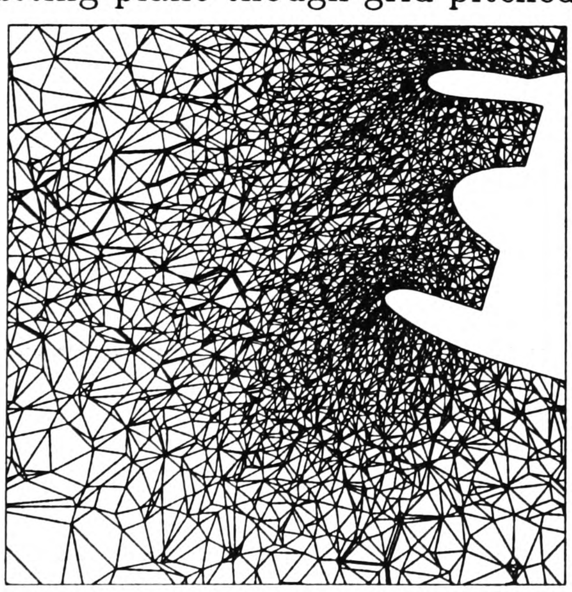

(c) Cutting plane though grid pitched up.

Figure 4.6: Illustration of the 3D grid movement method.

4.2.2 Notes on Implementation Issues

Perturbations in two dimensions are straight forward to implement, but perturbations in three dimensions need some careful consideration. This is particularly true at intersections of different surfaces. The GMM was implemented on (a) 3D pylon-OGV case and (b) a typical twin engine aircraft. Issues encountered in these experiments are outlined here:

Symmetry Plane The aircraft grid was generated for only one half of the configuration and involved a symmetry plane. One of the tests involving the GMM on the aircraft was implementing a pitching angle on the aircraft where the whole aircraft was rotated by the user specified angle. Here to ensure that the grid perturbation was consistent through out the grid, it was necessary to introduce a boundary condition on the nodes on the symmetry plane. This boundary condition permitted the nodes to slide in the symmetry plane and thus avoided shearing of the grid at the junction of the fuselage and the symmetry plane.

OGV-Annulus A very similar boundary condition (as above) was needed at the junction of the OGV and the hub and tip surfaces. Figure 6.3 (see page 109) presents the geometry. To ensure that the perturbations to the blades was consistent through out the blade span, it was necessary to allow nodes on the hub and tip surfaces to slide along the surface. In essence, the nodes were allowed to move and then they were projected back onto their respective surfaces. Thus, perturbations were uniformly implemented through out.

Wing-Pylon-Nacelle The GMM was used to "move" the engine nacelle in an aircraft to study the effect of engine location on drag. The movement of the nacelle included a perturbation along the flow direction and along the z direction (altitude). In this study, the nacelle shape was to be preserved while the pylon was allowed to distort. A smooth perturbation function from 0 to 1 was constructed for the configuration. The function was 0 over the aircraft except on the nacelle where it was 1 and on the pylon where intermediate values were used. The function is presented in figure 4.7, where the red colour is used to indicate 0 and blue represents 1. Despite such a smooth function for the perturbation, severe problems were encountered in moving the mesh. Upon investigation it was determined that there were several cells where all nodes were surface nodes (wing-pylon or pylon-nacelle) and that these cells were easily inverted if the perturbations were large (due to differing perturbations on different nodes) thus resulting in an invalid grid. Additionally the number of cells lying between the wing and nacelle were few making this movement an overconstrained problem. It was decided that the solution to these issues was in generating a new grid with greater grid density in the wing-pylon-nacelle region. This would result in smaller cells and help relieve the overconstrained nature of the problem by reducing the perturbation required for each node in a cell. The new grid was then easily perturbed by the GMM.

4.3 A Quasi-Newton Method

In the 3D OGV design problem we can express the design objective as a minimisation of the pressure mismatch integral I:

$$I = \frac{1}{2} \int_Y (p - p_{\ specified})^2 dy. \tag{4.10}$$

where Y is some curve over which the integration is performed. The discrete form of this equation can be written as

$$I = \frac{1}{2} \sum_i \left(p_i - p_{i\ specified}\right)^2 \Delta y_i \tag{4.11}$$

where the p_i is the pressure evaluated along a circumferential line upstream of the OGV's. At a minimum of I,

$$\frac{\partial I}{\partial v_j} = 0; \qquad 1 \leq j \leq N_v \tag{4.12}$$

where $\vec{v}$ is the vector of design variables and N_v is the number of design variables. Linearising about the current position in the design space we get the following N_v Newton equations.

$$\sum_{j=1}^{N_v} \delta v_j \cdot \frac{\partial^2 I}{\partial v_j \partial v_k} = -\frac{\partial I}{\partial v_k}; \qquad 1 \leq k \leq N_v \tag{4.13}$$

Substituting equation (4.11) in (4.13) we get

$$\sum_{j=1}^{N_v} \delta v_j \left\{ \sum_i \left[\frac{\partial p_i}{\partial v_j} \frac{\partial p_i}{\partial v_k} + (p_i - p_{i\ specified}) \frac{\partial}{\partial v_j}\left(\frac{\partial p_i}{\partial v_k}\right) \right] \Delta y_i \right\}$$
$$= -\sum_i \left(p_i - p_{i\ specified}\right) \Delta y_i \frac{\partial p_i}{\partial v_k}; \qquad 1 \leq k \leq N_v \tag{4.14}$$

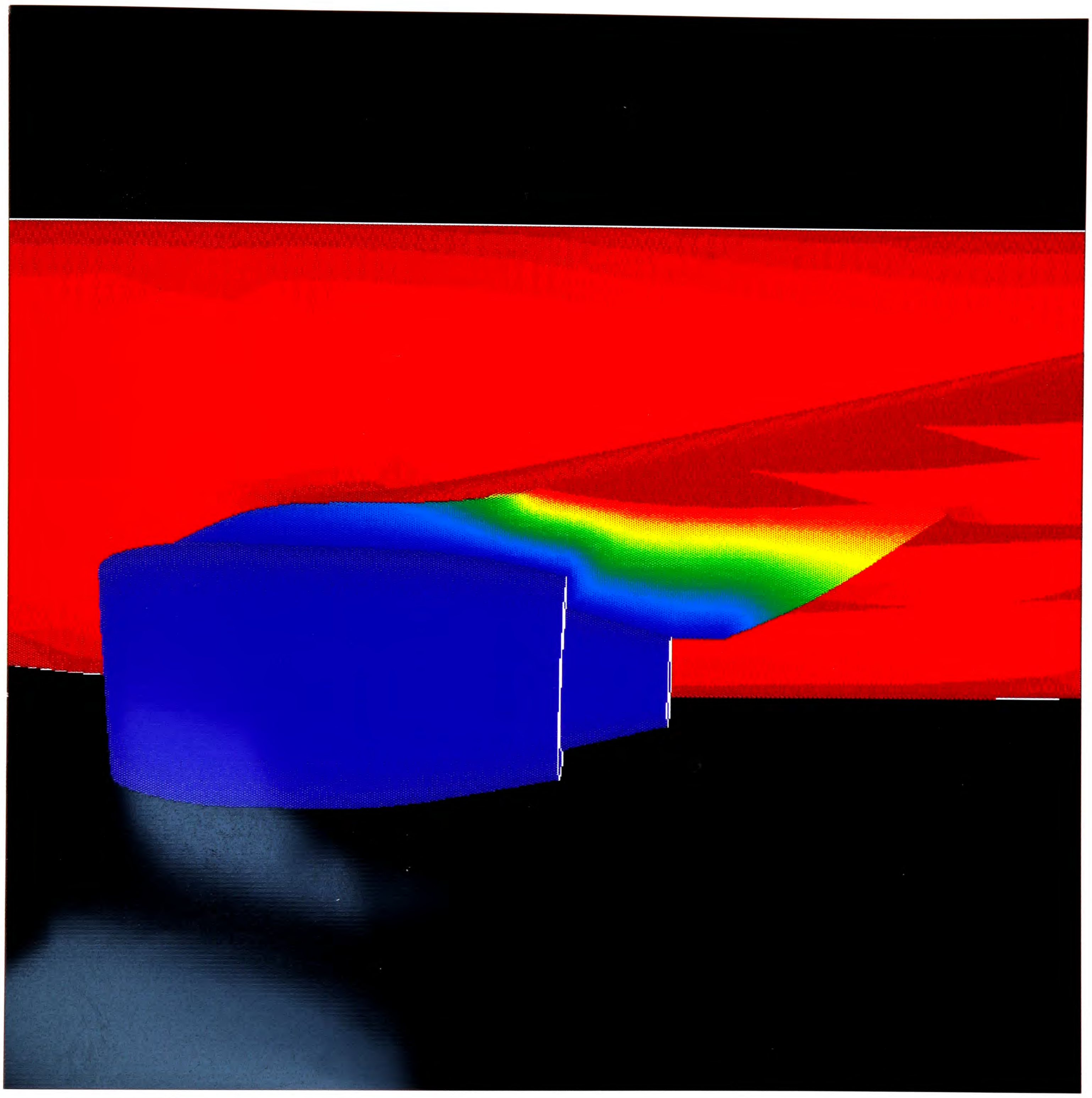

Figure 4.7: Z perturbation function specified on an aircraft wing-pylon-nacelle configuration.

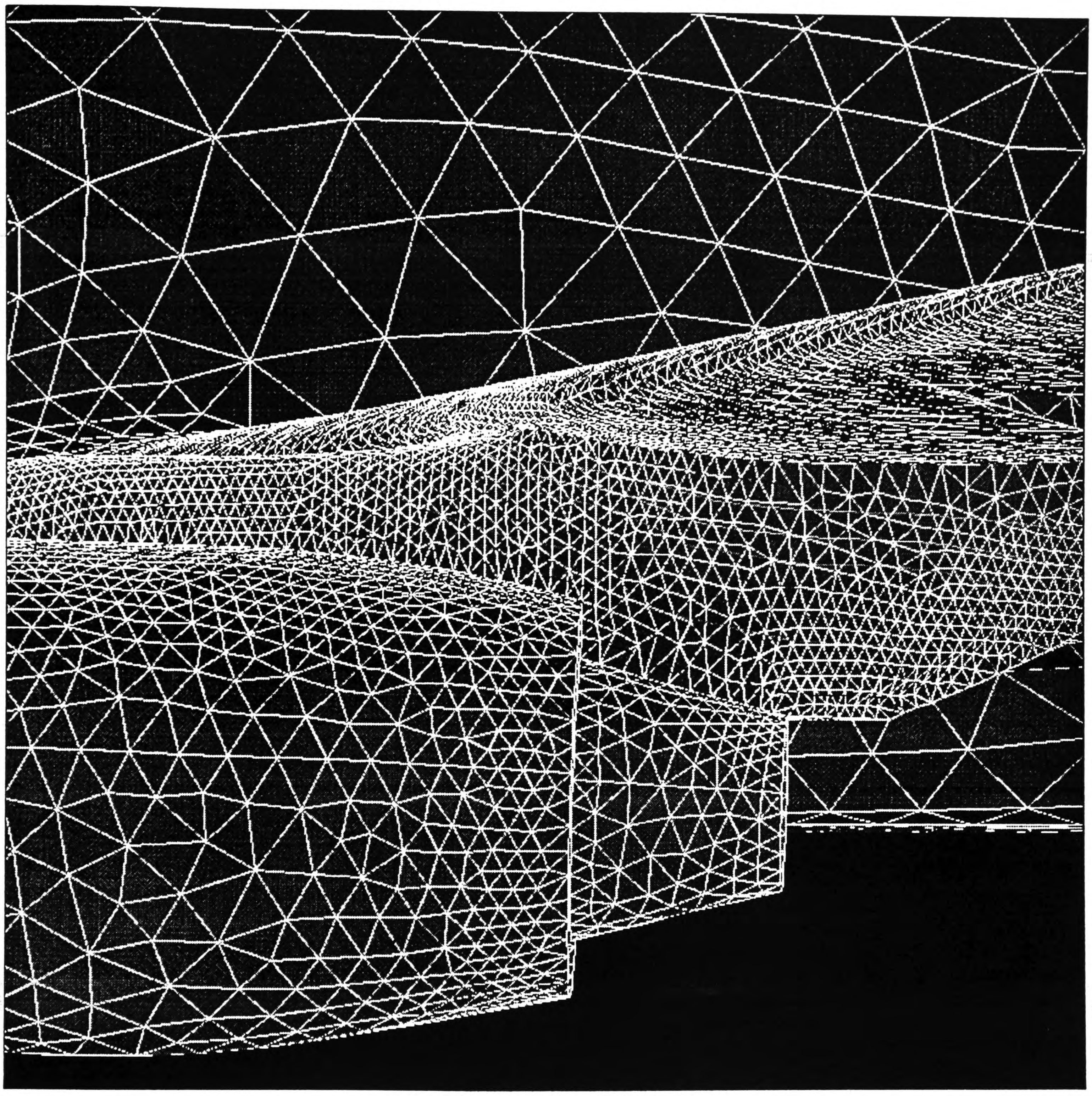

Figure 4.8: Illustration of increased grid density in wing-pylon-nacelle region.

The terms within the square brackets represents the Hessian matrix for the pressure mismatch integral I. In the present study we make the Quasi-Newton approximation in which we neglect the cross derivative terms in the square brackets (the second term) because it is complicated and expensive to compute. This approximation is acceptable, because we are interested in a redesign and are therefore not very far from the minimum. In this region the $(p_i - p_{i\ specified})$ term becomes very small and the effect of dropping the cross derivative terms is negligible. It has also been observed by Drela [15] that the neglected term has a minor impact.

For a one variable case equation 4.14 reduces to:

$$\delta\vec{v} = -\left(\frac{\sum_i \left(p_i - p_{i\ specified}\right) \frac{\partial p_i}{\partial \vec{v}} \Delta y_i}{\sum_i \left(\frac{\partial p_i}{\partial \vec{v}}\right)^2 \Delta y_i}\right) \tag{4.15}$$

while, for a two variable case we solve the following system of equations:

$$\begin{bmatrix} \sum_i (\frac{\partial p_i}{\partial \vec{v}_1})^2 \Delta y_i & \sum_i \frac{\partial p_i}{\partial \vec{v}_1}\frac{\partial p_i}{\partial \vec{v}_2} \Delta y_i \\ \sum_i \frac{\partial p_i}{\partial \vec{v}_1}\frac{\partial p_i}{\partial \vec{v}_2} \Delta y_i & \sum_i (\frac{\partial p_i}{\partial \vec{v}_2})^2 \Delta y_i \end{bmatrix} \cdot \begin{bmatrix} \delta\vec{v}_1 \\ \delta\vec{v}_2 \end{bmatrix}$$

$$= \begin{bmatrix} -\sum_i (p_i - p_{i\ specified}) \frac{\partial p_i}{\partial \vec{v}_1} \Delta y_i \\ -\sum_i (p_i - p_{i\ specified}) \frac{\partial p_i}{\partial \vec{v}_2} \Delta y_i \end{bmatrix} \tag{4.16}$$

The 1 and 2 variable quasi-Newton cases will be used in this thesis. This method becomes expensive for problems that involve many design variables. In such circumstances it will be beneficial to use adjoint methods to compute the gradients. The term $\frac{\partial p_i}{\partial \vec{v}}$ in the equations is computed by finite differences.

$$\frac{\partial p_i}{\partial v_j} = \frac{p_{i,pert} - p_i}{\Delta v_j} \tag{4.17}$$

where v_j is the j^{th} component of $\vec{v}$ and $p_{i,pert}$ is the variable p measured at the i^{th} line segment on the perturbed grid. Note however that there is no perturbation to the grid on circumferential line used to define I. The accuracy of this approximation depends on the step size used and the degree of convergence to steady state of the flow solution (reduction of residual by acceptable orders of magnitude) prior to the finite differencing. These issues are discussed in a following section.

4.3.1 Validation of the Quasi-Newton scheme

The validation of the quasi-Newton design method was based on a simple ONERA M6 wing test case. The pitch angle was specified as the design parameter. The pressure distribution at a specific spanwise location computed at $\alpha = 5°$ was specified as the design objective. It was desired that by altering the pitch angle, (by actually perturbing the grid rather than varying the input information to the flow code), the design code should achieve the target pressure at the predetermined spanwise location. The Cp plots on the wing surface are presented in figure 4.9, the history of pitch angle is plotted in figure 4.10.

Figure 4.10 has two curves that corresponds to two different grids of the ONERA M6 geometry. The `om6.oxd` grid had 46K nodes while the `s8.oxd` grid had 5.5K nodes. It can be seen that the initial prediction overshoots the objective, however the next step taken corrects the error and the design objective is met. The overshoot can be attributed to the inaccurate evaluation of the gradient, the linearisation approximations coupled with the neglected cross-derivative term. The rapid convergence is very encouraging; it will be seen in subsequent chapters that convergence is always attained within 3 steps for this class of problems.

4.4 Implementation Issues of the Design Method

We have the basic ingredients of a design method. A robust and fast flow solver, a robust grid movement algorithm and an optimization procedure. A mechanism to integrate these various systems needs to be developed. The design method serves as a virtual machine linking a cluster of computers that include high performance computers (slaves) and a desktop graphic workstation (master). The design code will send the flow solver and the GMM to the slaves, and will use the graphic workstation to visualise the progress. Using such a master-slave setup allows the designer to interact with the design code and to alter the configuration of the virtual machine dynamically. Additionally, it will be possible to farm out the computation of the GMM and flow solutions on perturbed geometries to different slaves to take advantage of the inherent parallelism of this process. The structure of the design method developed in the course of this thesis is presented in figure 4.11. The master program interacts with the slaves through a system of job-cards which spawn the GMM and the flow solver on appropriate machines. The master recovers control when all flow solutions have been acquired. The next point in design

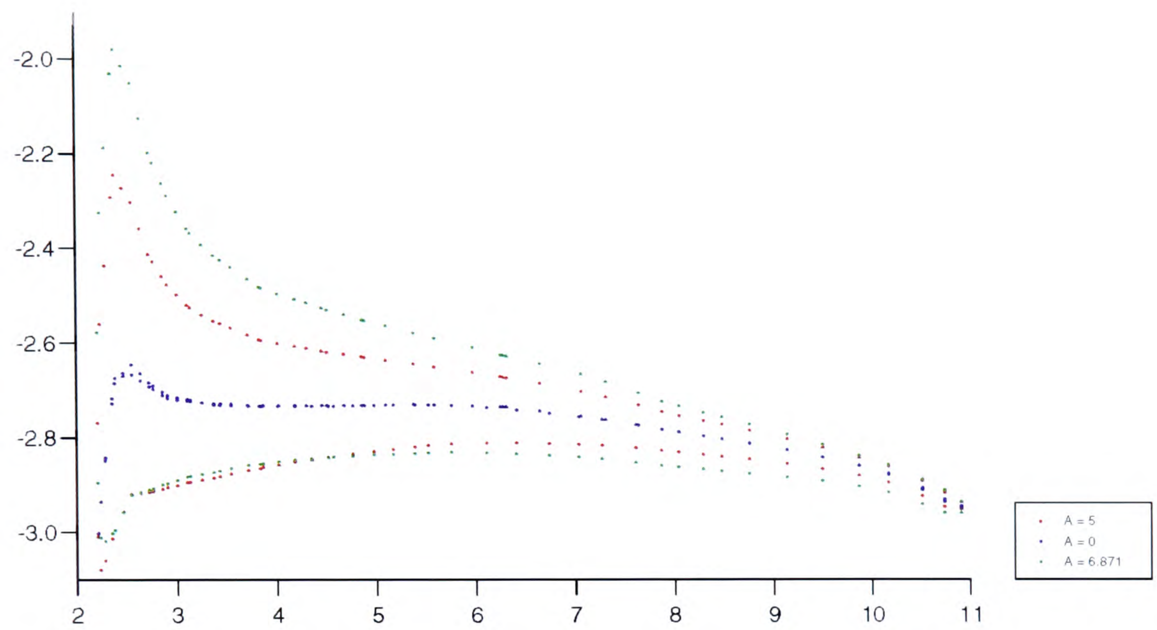

Figure 4.9: ONERA M6: Initial, 1st step and desired Cp plots.

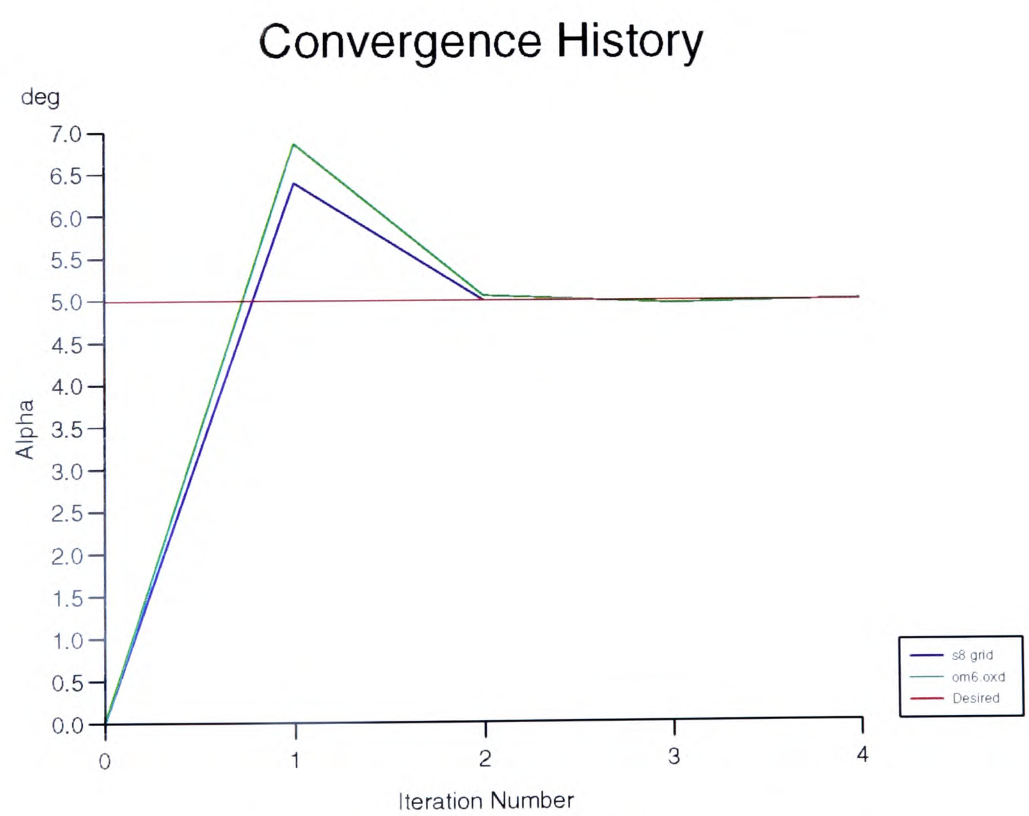

Figure 4.10: ONERA M6: Convergence of design variable.

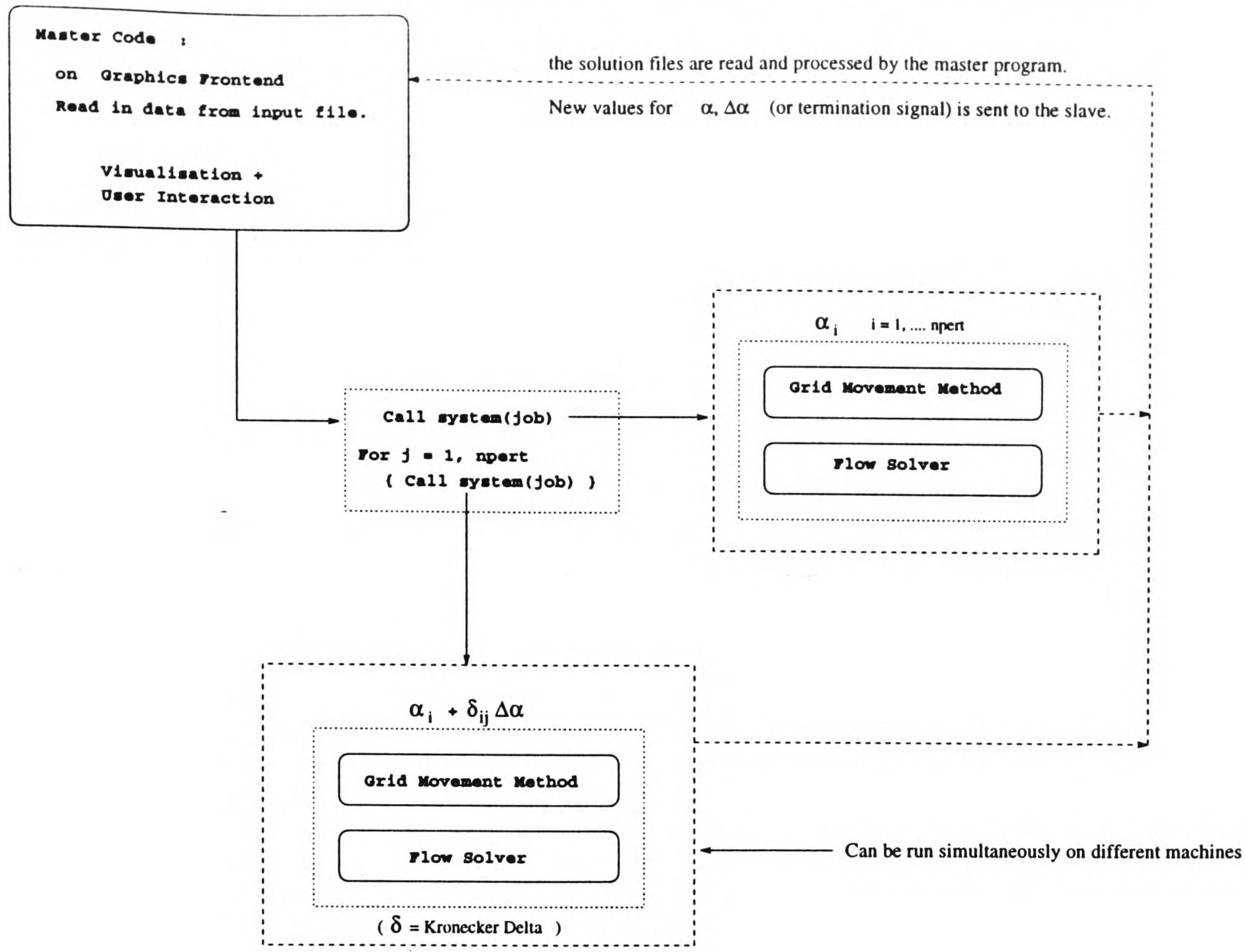

Figure 4.11: Structure of the design code.

space is computed, which is then tested for termination criteria (convergence and number of iterations) and based on this the master either executes the design loop again or exits.

An important issue that needs to be resolved is the definition of "tolerance". The minimisation routine needs some mechanism wherein it can decide whether the desired objective has been sufficiently met. The tolerance defined for a design run has to be carefully selected. Such tolerances can be based on (a) the cost function or (b) the predicted change in design variables. Since we obtain sensitivities by finite differences, the step size used to compute sensitivities serves as a lower bound on the size of design perturbations. When the predicted changes are smaller than the step size, the next set of sensitivities obtained through finite differences can cease to be meaningful and so the design method terminates. This is the convergence criterion used in the present work. The number of design iterations can also be used as a termination criterion.

4.5 Acceleration Techniques

We have by now decided on a design mechanism and also on certain implementation issues. What remains to be investigated are techniques by which the design code can be accelerated. In this section we will review two different methods of accelerating the design process.

By the term "acceleration" here we do not necessarily mean just a quicker descent in terms of the number of iterations needed to converge the design process, but in actual reduction in time taken to compute the new design. In fact, there is no interest in acceleration unless it directly results in decreased "wall clock" time for a design process. However, we exclude methods such as parallel processing in flow solvers because we treat computational codes as black boxes and their acceleration is beyond our control. So given a set of computational methods and computer hardware we need to decrease design time. There is essentially one control over this process and that is the accuracy of the gradient computed by means of a finite difference procedure.

In the following subsections we will discuss two methods to measure these gradients accurately. The first approach will be to vary the step size to acquire more accurate/representative gradients. The second is an idea similar to the multigrid method and involves subtracting the residuals of the flow solution at the current point in design space from the RHS of the system of equations for the perturbed cases.

4.5.1 Step size for Gradient Evaluation

The step size $\Delta\vec{v}$ used in the finite difference routine is crucial to the performance of the design method. When the step size is too large or too small we get an incorrect approximation of the gradient which can mislead the optimiser. However, since we use a Newton descent method and assume that we are in the vicinity of the solution, the use of large step sizes can help overcome nonlinearities in the behaviour of the cost function. This allows us to converge towards the right solution much faster.

By comparing figure 4.13 and 4.17 we observe a drastic reduction in the tower blocks. This is due to the large step size which helps the finite difference method acquire a more "representative" gradient even when the flow solutions have not converged. However, one can note, that when the flow solver is allowed to converge sufficiently (to about 10^{-9}) both methods perform equally well. In tables 4.1-4.3 data is presented for the design code run on the ONERA M6 validation case using different step sizes (under the "Resread = False" column).

A combination of step sizes on different grids is the best way to achieve acceleration ie. if the design mode in question is a low frequency mode (ie, will have a recognisable effect on the flow field even in a coarse mesh) then a coarse mesh and a large step size can be used to pick out the neighbourhood of the minima and then smaller step sizes can be be used in conjunction with fine grids to identify the required design point.

4.5.2 Use of Residuals of the Previous Calculation

Flow codes consume a very significant part (upto 85%) of the time taken in each iteration of the design process. Most of this time is spent in driving the residuals down even after all important flow variables have converged (to within engineering tolerances). It is the norm to drop the residual by at least 5 orders of magnitude before the solution is deemed acceptable. The gradients are evaluated from such converged flow solutions. The issue here is, the actual flow solution is not the primary objective of the design code, it is the gradients that we are interested in. So the quality of the flow solution should not be very crucial, as long as the gradients can be computed accurately. Figure 4.12 demonstrates what we are attempting here. Let us assume that we are trying to compute $\frac{\partial P}{\partial \alpha}$, where P is some function of α (as shown in figure 4.12). The solid line in the figure is the "true" solution, the dashed lines that surround it are the bounds within which any computed solution lies for a given tolerance of the computational method used to compute $P(\alpha)$. Point a in the figure corresponds to the solution $P(\alpha)$, the gradient is computed as:

$$\frac{\partial P}{\partial \alpha} = \frac{P(\alpha + \delta\alpha) - P(\alpha)}{\delta\alpha} \tag{4.18}$$

Points b,c,d represent three possible values computed for $P(\alpha + \delta\alpha)$. To obtain an accurate estimate of the gradient we need c–a. Gradients based on b–a and d–a will be erroneous. But, there is no method by which we can the flow solver can be directed to obtain point c in preference over b or d. All the points lie within the tolerance specified for the flow solver. To compute more accurate gradients we need to reduce the tolerance, thus requiring more stringent convergence criterion on the flow solver, thereby increasing flow solution time. The trade offs here is between greater flow solution time at each step against a greater number of iterations in the design loop (due to incorrect gradients), and greater solution time is the obvious choice.

We shall try to use the residuals of the first flow solution (point a in figure 4.12). Let us assume that the flow field is defined by a system of the form:

$$A \cdot X = b \tag{4.19}$$

where X is the unknown flow field parameters. The solutions that correspond to α and $(\alpha + \delta\alpha)$ can be expressed as:

$$A_1 \cdot X_1 = b_1 \tag{4.20}$$
$$A_2 \cdot X_2 = b_2 \tag{4.21}$$

where the X_1 is the true solution for the flow field at α and X_2 is the true solution for the flow field at $(\alpha+\delta\alpha)$. In an iterative solution, the above system is never solved completely. Instead we actually obtain Y_1 and Y_2, which are solutions for the following systems:

$$A_1 \cdot Y_1 = b_1 - r_1 \tag{4.22}$$
$$A_2 \cdot Y_2 = b_2 - r_2 \tag{4.23}$$

where r_1 and r_2 are the residuals. Also since we assume a small perturbation $\delta\alpha$, A_2 can be expressed as:

$$A_2 = A_1 + \delta A \tag{4.24}$$

The finite difference equation (4.18) can be expressed in terms of X as

$$\frac{\partial P}{\partial \alpha} = \frac{X_2 - X_1}{\delta\alpha} \tag{4.25}$$

thus, for accurate gradients we need to minimise the error E, where E is:

$$E = (Y_2 - Y_1) - (X_2 - X_1) \tag{4.26}$$

$(Y_2 - Y_1)$ can be expressed as:

$$(Y_2 - Y_1) = A_2^{-1}(b_2 - r_2) - A_1^{-1}(b_1 - r_1) \tag{4.27}$$

rearranging terms we get

$$Y_2 - Y_1 = (X_2 - X_1) + A_1^{-1}r_1 - A_2^{-1}r_2 \tag{4.28}$$

combining eqns (4.26) and (4.28) we get

$$E = A_1^{-1} r_1 - A_2^{-1} r_2 \tag{4.29}$$

by rearranging terms and using A_2 as defined in eqn (4.24) we get

$$E = \frac{r_1 - r_2}{(A_1 + \delta A)} + \frac{r_1 \delta A}{A_1 (A_1 + \delta A)} \tag{4.30}$$

The second term in this equation is a very small quantity and can be neglected. It is therefore the first term that dominates the error E.

By using the residuals we mean to write out r_1 when the flow computation is terminated and to reuse this in the computations on perturbed flow fields. The residual will be subtracted from the RHS of equation 4.23 giving

$$A_2 \cdot Y_3 = (b_2 - r_1) - r_3 \tag{4.31}$$

Note: *Solution of the new system will not result in Y_2 but in a Y_3 which is associated with a residual r_3*. Using the new system, the error E (now defined as $(Y_3 - Y_1)$) can be written as

$$E = \frac{r_1 \delta A}{A_1 (A_1 + \delta A)} - \frac{r_2}{(A_1 + \delta A)} \tag{4.32}$$

The first term is a small term and can be neglected and the second term is seen to dominate E. However, unlike before we have a definite bound on E. The error is now dependent only on r_2. Thus, we need to solve the perturbed flow solutions to a greater accuracy than the base flow solution.

Numerical experiments to determine the relation between the $||\cdot||_\infty$ of r_1 and r_3 were conducted. These experiments involved varying the level of convergence of the flow solver while performing the ONERA M6 based design test case. The number of design iterations needed to converge the design process was noted. This is presented in figures 4.13-4.18 and tables 4.1-4.3. The experiments included varying the step sizes to observe their effect on the convergence (of the design process). In the figures, the X axis (shown as T1 in all figures) is the log of the residual of the base run. A -4 corresponds to a convergence criteria of 1.0E-04 on the flow solver. Similarly the Y axis (shown as T2 in all figures) presents the convergence criteria for the perturbed flow solution. The Z axis is used to show the number of iterations used by the design code to converge to solutions. In cases when no convergence was obtained or the design method crashed a "high" number of 40 was used. When the design code was close to the solution but didn't converge a number of 20 was used. In

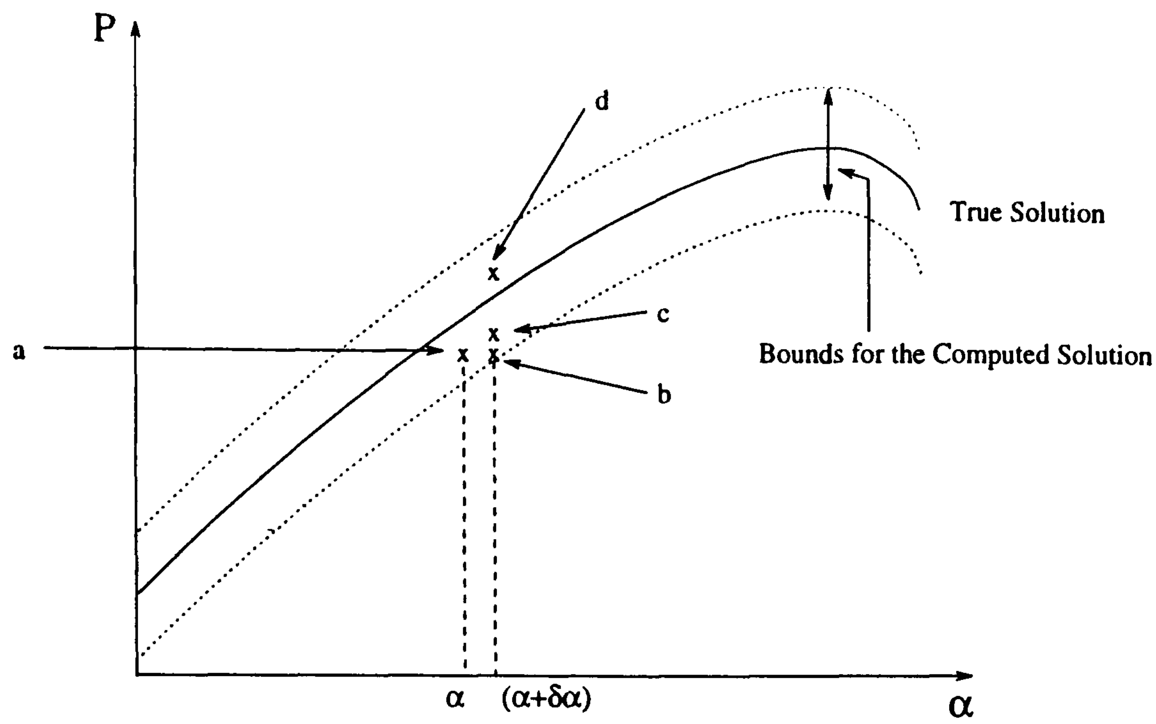

Figure 4.12: Concept of reading residuals at $(\alpha + \delta\alpha)$.

effect, the tall "tower block" like structures represent combinations of r_1 and r_3 for which the design code failed completely. If the change in α predicted by the design method was lower than 0.01 then the design method was deemed to have converged. This was done to have a uniform convergence criteria for all runs, such a criterion was acceptable for the present study because I is linear w.r.t α and there was no fear of flow separation.

The reduction in tower blocks is clearly visible in all figures. The effectiveness is more pronounced in tests with smaller step size because eqn (4.24) is valid. This is not the case when the step size is equal to 1.

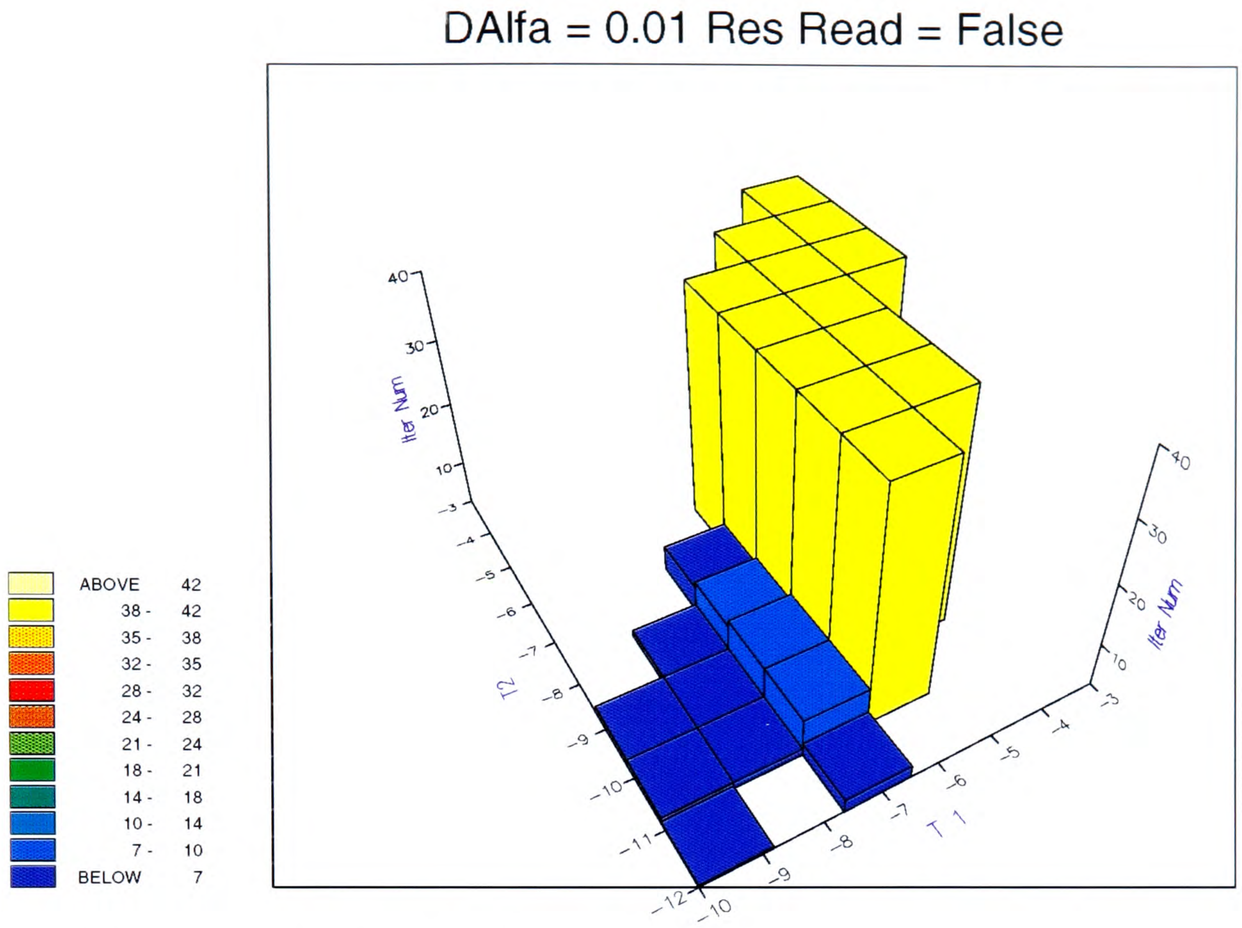

Figure 4.13: Tower Block figure for $\delta\alpha = 0.01$, no residual subtraction.

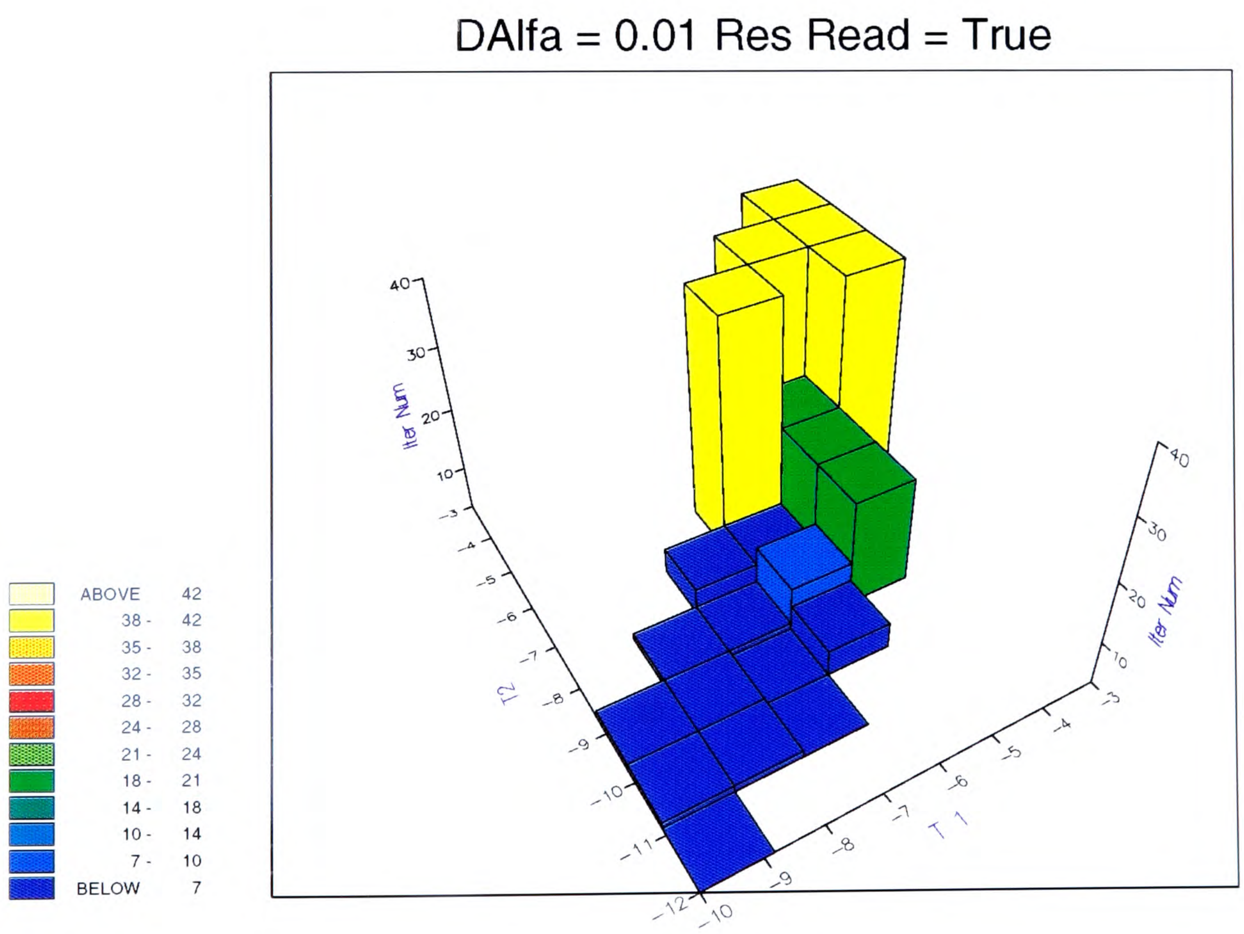

Figure 4.14: Tower Block figure for $\delta\alpha = 0.01$, residual subtraction.

Log (r_1)	Log (r_1)	No of Design Itern at ResRead = FALSE	No of Design Itern at ResRead = TRUE
-3	-3	No Convergence	Not Feasible
	-4	No Convergence	Not Feasible
	-5	No Convergence	Not Feasible
	-6	Not Feasible	Not Feasible
-5	-5	No Convergence	Not Feasible
	-6	Not Feasible	No Convergence
	-7	Not Feasible	No Convergence
	-8	Not Feasible	No Convergence
-6	-6	No Convergence	Not Feasible
	-7	No Convergence	7
	-8	Not Feasible	5
	-9	Not Feasible	2
-7	-7	7	4
	-8	8	3
	-9	9	3
	-10	9	4
-8	-8	4	4
	-9	4	4
	-10	4	4
-9	-9	4	4
	-10	4	4
	-11	3	3
-10	-10	4	4
	-11	3	3
	-12	3	3

Table 4.1: Step Size = 0.01

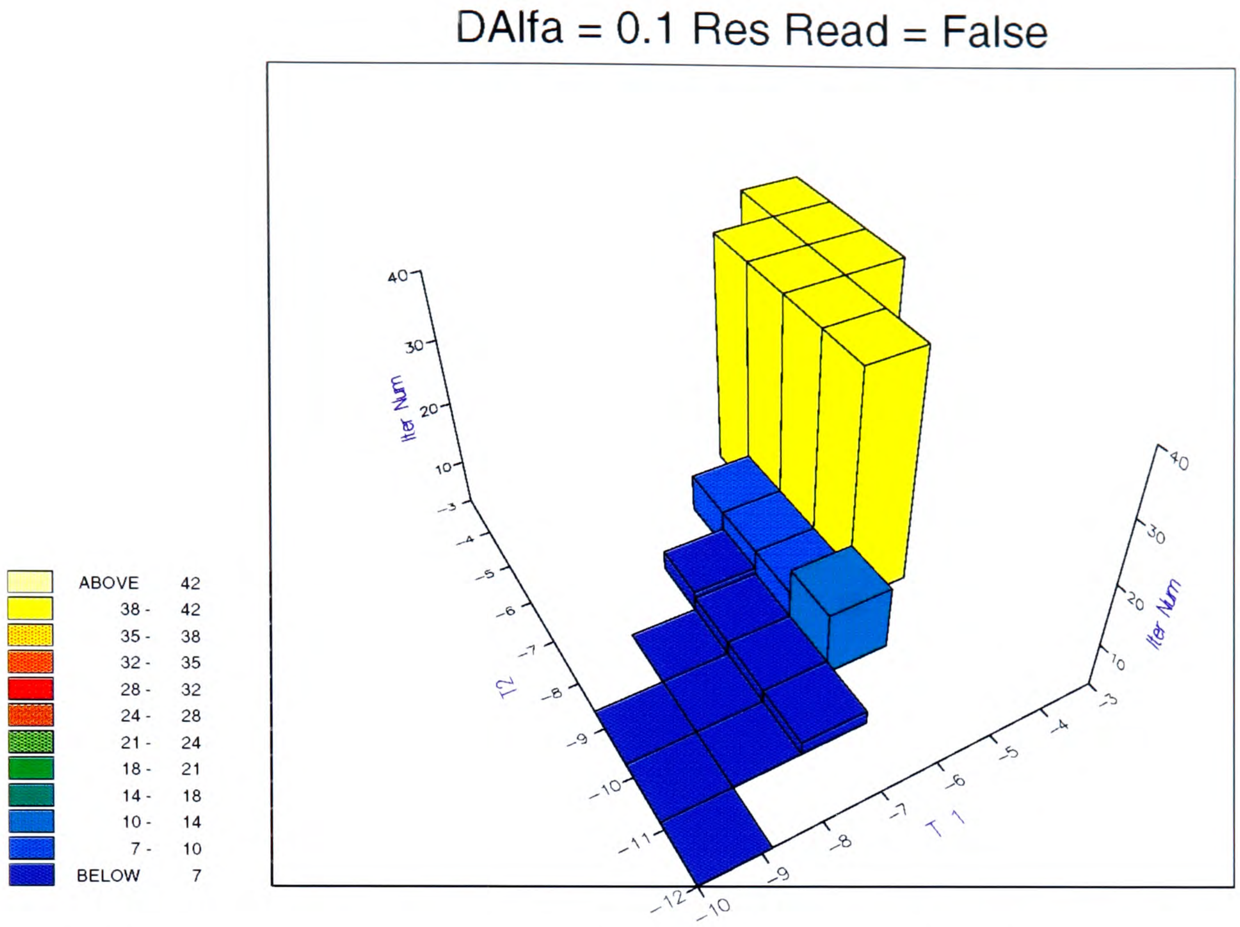

Figure 4.15: Tower Block figure for $\delta\alpha = 0.1$, no residual subtraction.

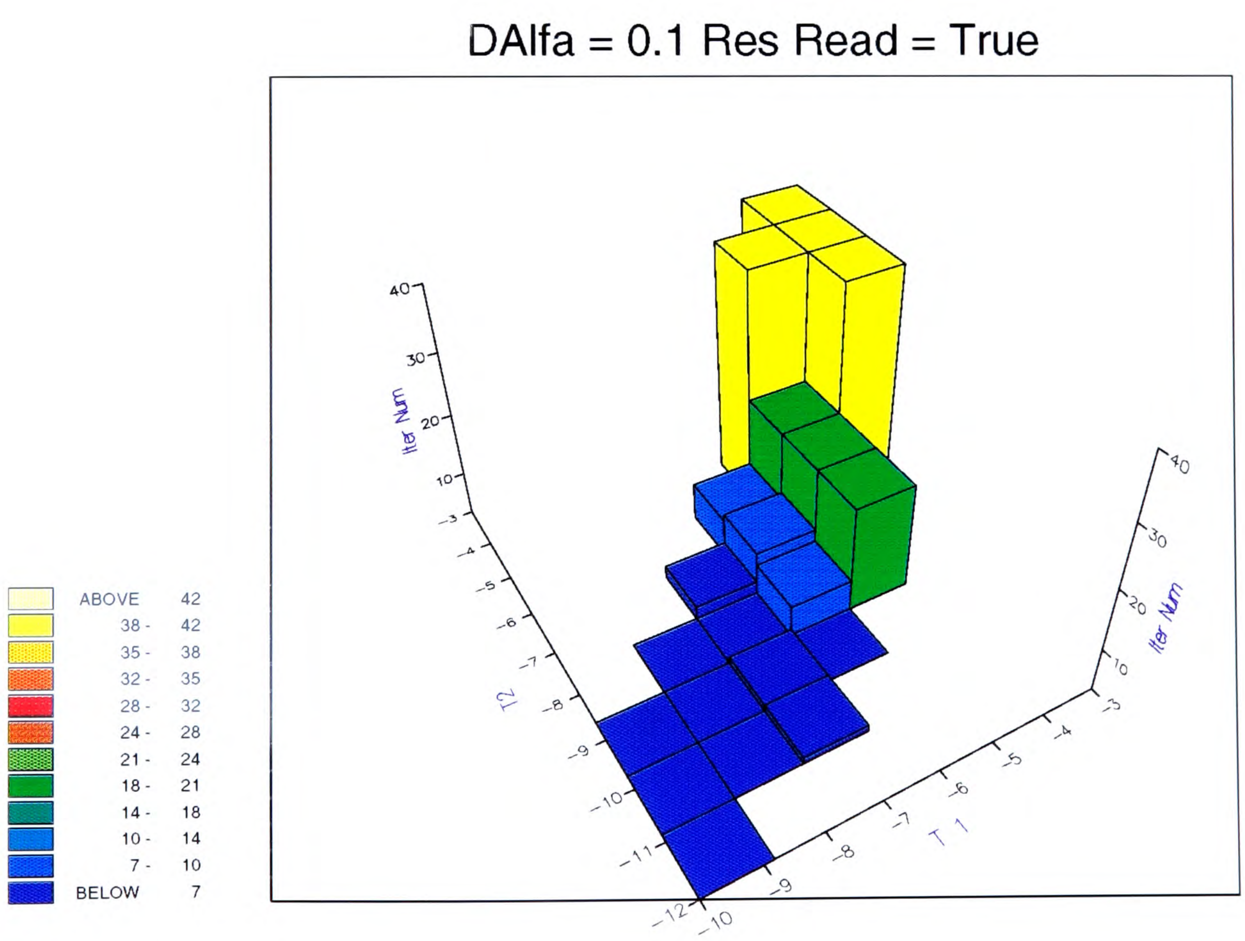

Figure 4.16: Tower Block figure for $\delta\alpha = 0.1$, residual subtraction.

Log (r_1)	Log (r_1)	No of Design Itern at ResRead = FALSE	No of Design Itern at ResRead = TRUE
-3	-3	Not Feasible	Not Feasible
	-4	No Convergence	Not Feasible
	-5	Not Feasible	Not Feasible
	-6	Not Feasible	Not Feasible
-5	-5	Not Feasible	Not Feasible
	-6	Not Feasible	No Convergence
	-7	Not Feasible	No Convergence
	-8	Not Feasible	No Convergence
-6	-6	9	9
	-7	9	10
	-8	9	8
	-9	13	3
-7	-7	6	5
	-8	5	3
	-9	5	4
	-10	5	4
-8	-8	3	3
	-9	3	3
	-10	3	3
-9	-9	3	3
	-10	3	3
	-11	3	3
-10	-10	3	3
	-11	3	3
	-12	3	3

Table 4.2: Step Size = 0.1

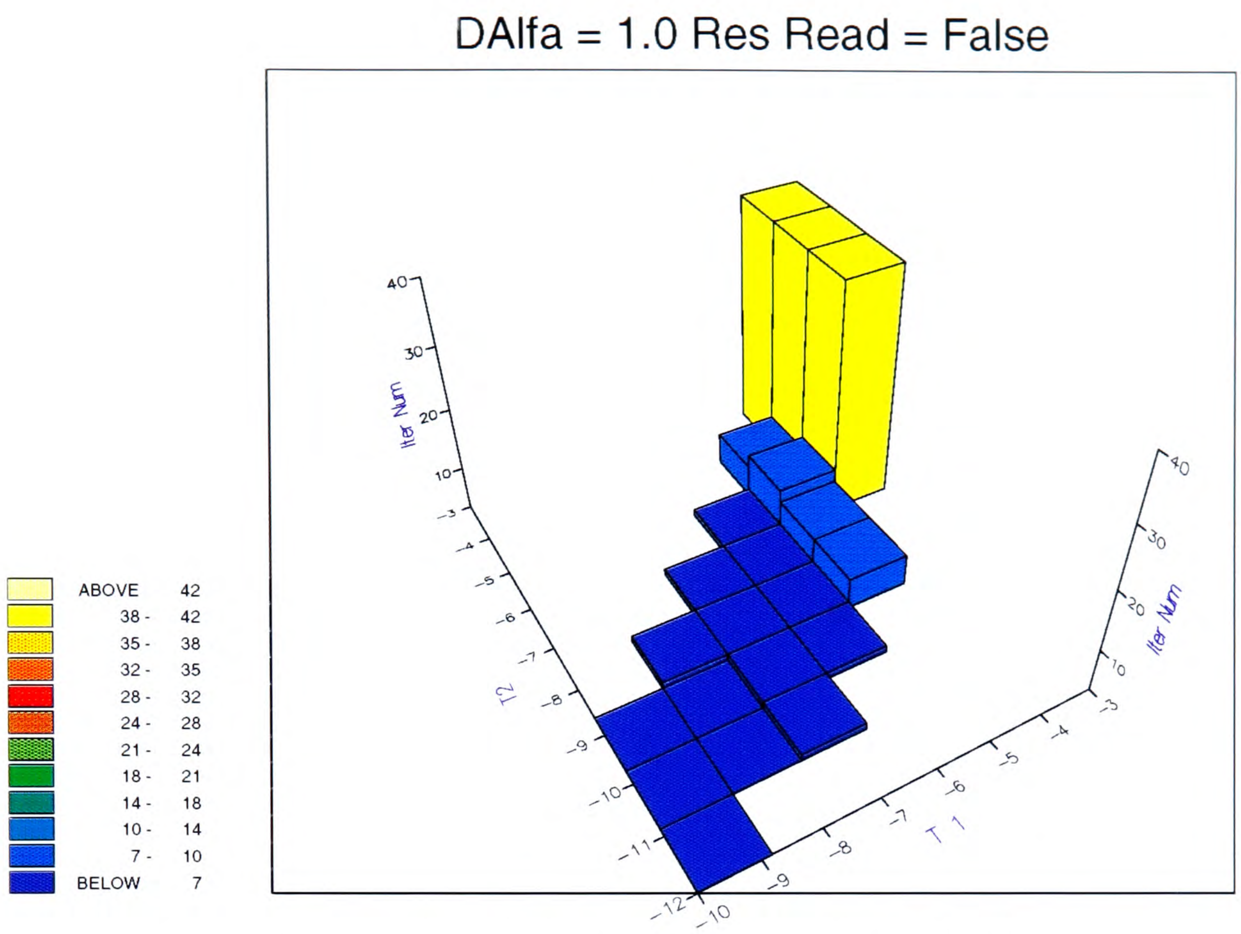

Figure 4.17: Tower Block figure for $\delta\alpha = 1.0$, no residual subtraction.

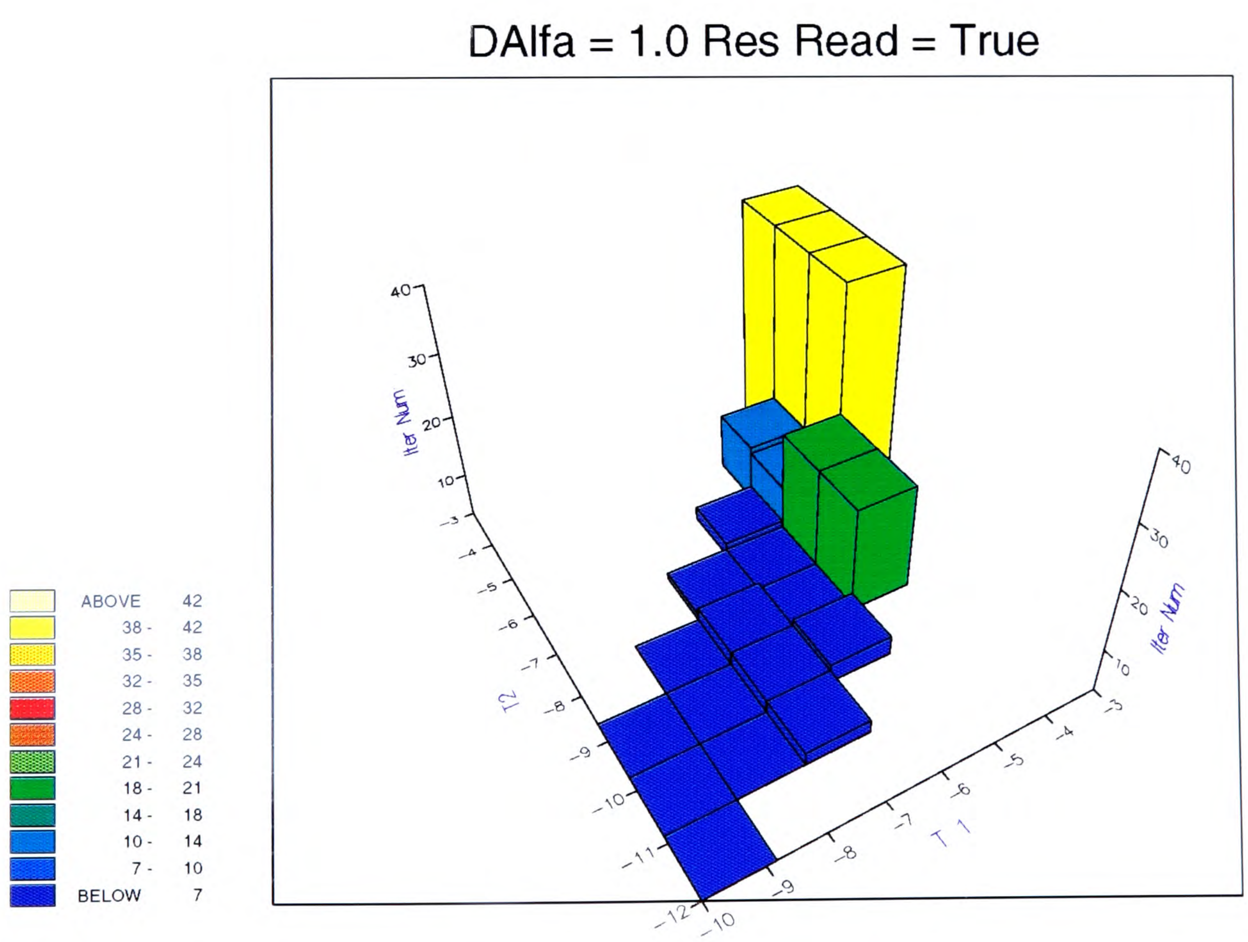

Figure 4.18: Tower Block figure for $\delta\alpha = 1.0$, residual subtraction.

Log (r_1)	Log (r_1)	No of Design Itern at ResRead = FALSE	No of Design Itern at ResRead = TRUE
-3	-3	No Convergence	Not Feasible
	-4	No Convergence	Not Feasible
	-5	Not Feasible	Not Feasible
	-6	No Convergence	Not Feasible
-5	-5	8	12
	-6	10	11
	-7	8	No Convergence
	-8	8	No Convergence
-6	-6	4	5
	-7	4	4
	-8	4	4
	-9	4	6
-7	-7	4	4
	-8	4	5
	-9	4	5
	-10	4	5
-8	-8	4	3
	-9	3	3
	-10	3	3
-9	-9	3	3
	-10	3	3
	-11	3	3
-10	-10	3	3
	-11	3	3
	-12	3	3

Table 4.3: Step Size = 1.0

Chapter 5

Redesign of an OGV row

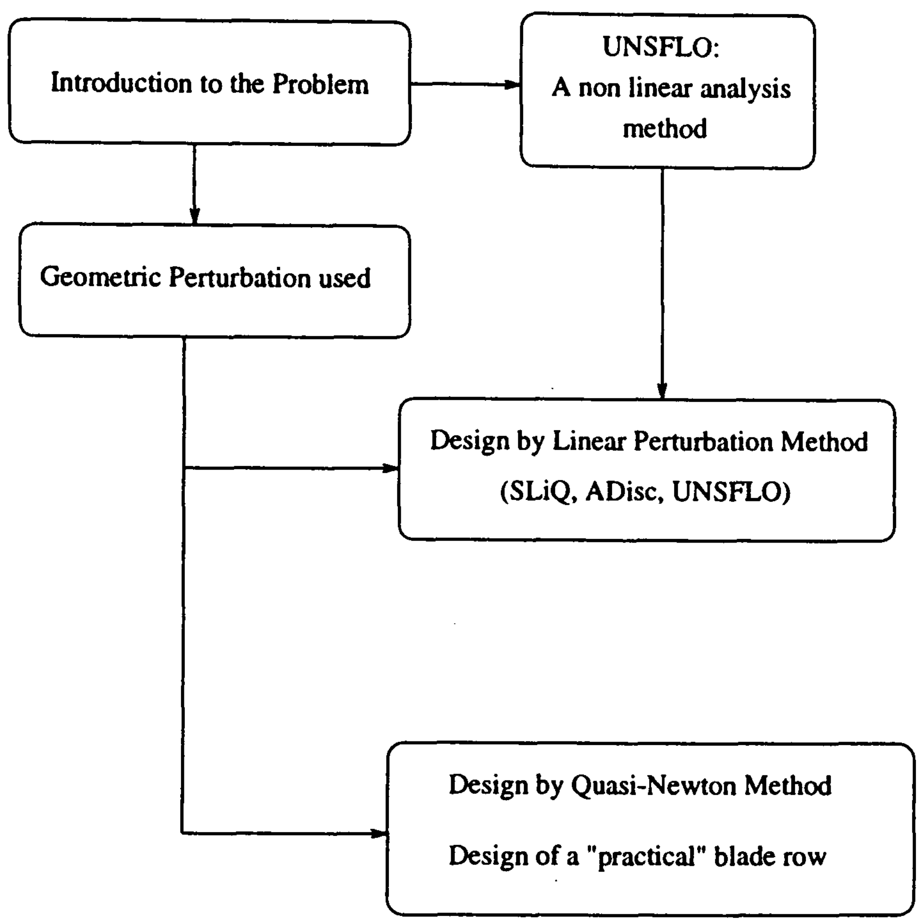

Figure 5.1: Flow chart of Chapter 5.

5.1 Introduction

It has been observed that the fan experiences high level of stresses due to excitation from the flow field. Analysis has identified this to be due to the excitation of the fan by the pylon induced static pressure field. It has also been observed that there can be a reduction of OGV efficiency, brought on by altering the incidence angle which can be attributed to the pylon induced pressure field. The jet engine of a commercial airliner is connected to the wing by the pylon (see fig 1.2) which serves not only as the structural link between the wing and the engine, but also as the conduit for the generator shafts, bleed air and hydraulic and control systems. The pylon, therefore, is a large obstacle to the flow in the bypass duct and, given its role, the redesign of the pylon itself is not feasible.

The presence of each component creates upstream and downstream disturbances. The OGV's also induce static pressure perturbations, but these have a very small circumferential wavelength and so decay rapidly in the axial direction and do not influence either the fan or the pylon. However, the pylon induced disturbance has a very slow decay and the pylon induced disturbance traverses the entire length of the bypass duct and interacts with the OGV's and the fan.

There have been various suggestions to prevent interaction with the pylon induced field [70] which include (a) the introduction of additional vanes to divert the flow around the pylon and (b) an increase in the distance between the OGV's and the pylon. Since the pylon induced field has a low axial decay rate, option (b) becomes unacceptable as it will require a considerable increase in engine size. Both modifications are unattractive as they will almost certainly result in increased size and weight of the engine and result in the introduction of additional components. These changes will have to be subjected to structural analysis and will be very time consuming. Therefore a passive redesign, tailoring existing components, is more appealing. Kodama and Nogano [48] have applied actuator disc theory [47] to analyze the problem of stator and downstream strut interaction. Using this theory they have performed stator tailoring to suppress the pressure field of the downstream strut and have also obtained good experimental verification. Barber and Weingold [2] have investigated the application of a Douglas-Neumann singularity method to determine the incompressible flow field through multibody cascades. Cerri and O'Brien [10] have studied the interaction problems of a stator-strut system at the rotor trailing edge. They have successfully reduced the strut induced pressure field to the same levels of the stator induced field by redesigning the stator blades.

In this thesis the tailoring of OGV's using the concept of cyclically varying camber is used as the test problem. The resulting OGV blades will induce a pressure perturbation equal and opposite in magnitude to that induced by the pylon in the flow field upstream of the OGV's. The changes to camber will be introduced as modification to the trailing edges so that the leading edge of the

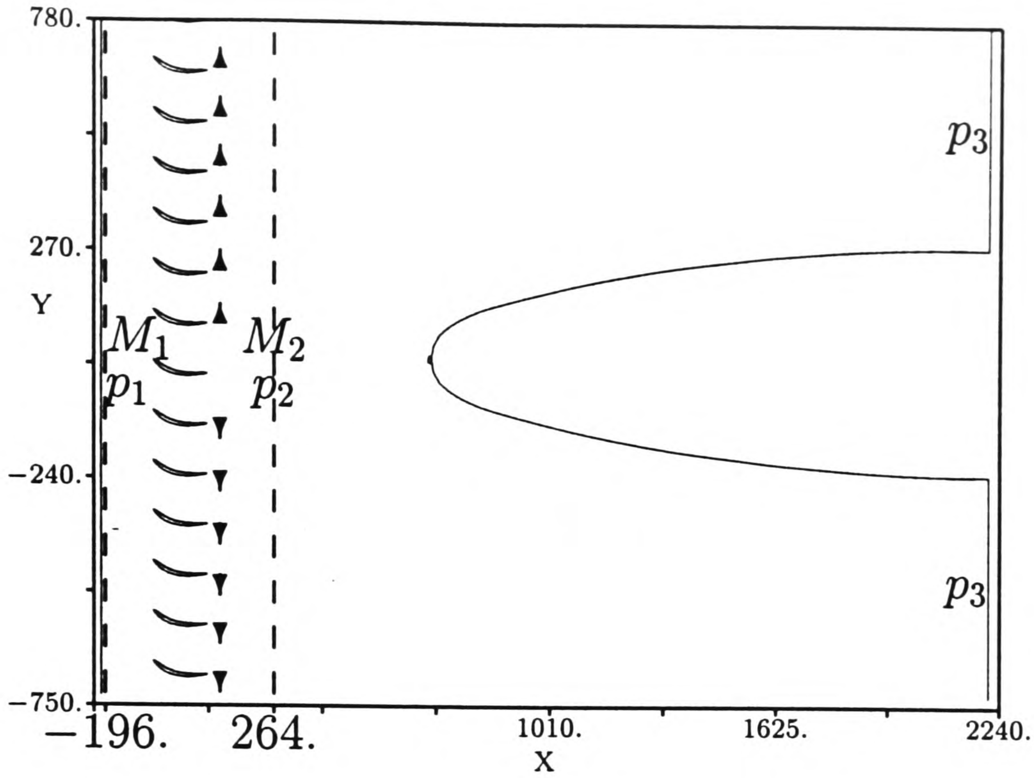

Figure 5.2: Pylon, OGV's and key axial locations used in analysis; arrow heads indicate direction of camber modification.

blade remains unchanged. This is consistent with the objective of achieving a uniform OGV incidence angle.

5.2 Camber Perturbation

The camber perturbation is designed to change the exit flow angle but leave the inlet flow unaffected. The overall design goal is to eliminate all non-uniformities upstream of the OGV's in which case the leading edge geometry of all blades should be kept fixed to achieve uniform incidence Accordingly, the perturbations used are of the form:

$$\Delta y = C_c(X - X_{le})^2 \exp(-iky) \tag{5.1}$$

where C_c is a complex quantity and $\exp(-iky)$ represents the harmonic nature of the perturbation. As explained in theory, only real part of Δy is actually used. The change in camber can be viewed as a variation in the trailing edge angle. If α is the mean exit flow angle from the OGV row then:

$$\tan(\alpha) = \frac{\Delta y}{\Delta x} \tag{5.2}$$

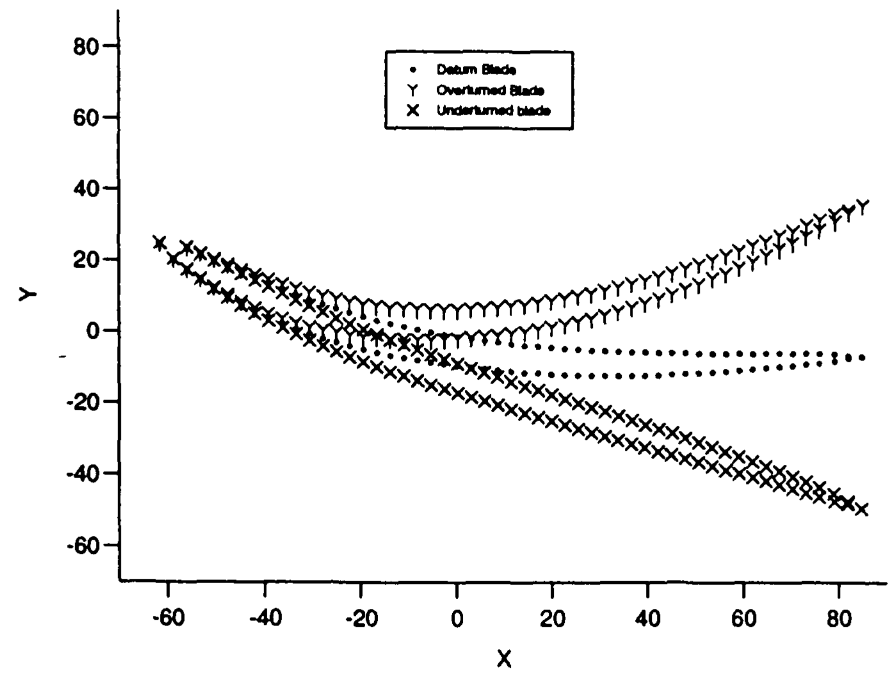

Figure 5.3: Camber perturbed blades.

which can be expressed in terms of perturbation quantities as:

$$\tilde{\alpha}\sec^2(\alpha) = \frac{\Delta\tilde{y}}{\Delta x} \tag{5.3}$$

but from eqn (5.1)

$$\frac{d\tilde{y}}{dx} = 2\ CCons\ (X - X_{leadingedge})\ \exp(-iky) \tag{5.4}$$

therefore, $\tilde{\alpha}$ can be expressed as

$$\tilde{\alpha} = 2\ \cos^2\alpha\ C_c\ (X - X_{le})\ \exp(-iky). \tag{5.5}$$

The sensitivity of camber to a unit perturbation is determined in the SLiQ analysis by setting $C_c = 1$. The crux of the redesign is to determine the appropriate value of C_c. Figure 5.3 (pg 5.3) illustrates the extreme limits of the camber perturbations for $C_c = 5 \times 10^{-2}$.

5.3 A Non Linear Analysis

As a verification tool a nonlinear analysis code "UNSFLO" was used. UNSFLO [23] can solve for steady or unsteady, viscous or inviscid equations of motion in two dimensions. It can handle various kinds of unsteadiness and arbitrary wake/rotor, stator/rotor pitch ratios. It uses highly accurate non-reflecting boundary conditions developed by Giles [22], which reduce the non-physical reflections at inflow and outflow boundaries. The computations are performed on an unstructured triangular grid, generated by an advancing front grid generator developed by Lindquist and Giles [52].

The use of UNSFLO for pylon/OGV interactions has been validated by Suddhoo using experimental data [70]. In the current application, UNSFLO is used in its inviscid mode, which uses the Lax-Wendroff algorithm to solve the Euler equations [26]. Though there are viscous effects present in the flow in the vicinity of the OGV's, the pressure disturbance is an inviscid feature, thereby permitting the use of UNSFLO and SLiQ in the inviscid mode.

5.4 Comparability of Various Solutions

In studies where there is a comparison of data from various sources, it is necessary to ensure that the results being compared are obtained from computations on the same flow conditions. This can be done by identifying a parameter of the flow which is common to all calculations and ensuring that this variable is maintained constant. The location of the parameter was chosen to be at $x = 264$ (shown in fig 5.2, pg 86) because this location was common to all computations (SLiQ, UNSFLO and ADisc). Mach number was selected as the key parameter since it is critical in determining the decay rate λ. As seen from fig 5.2 (pg 86), location 1 refers to the inlet $X = -196$, location 2 refers to $X = 264$ (exit of SLiQ and ADisc) and location 3 refers to the exit of the UNSFLO flow domain. The correct M_2 (Mach number at location 2) in the UNSFLO calculations was obtained by altering the exit pressure p_3. In the following runs M_2 was maintained close to 0.38. Important flow parameters for the linear perturbation based redesign are presented in table 5.1.

5.5 Redesign by a Linear Approach

It can be demonstrated from actuator disc theory that the pressure distribution is very sensitive to a change in the angle of the flow leaving the trailing edge of the OGV's. This sensitivity was used in the stator tailoring exercise. In all the plots included here the results from UNSFLO are duplicated so they

parameters	Original	Pylon Alone	Mod Blades Alone	Final Run
γ	1.4	1.4	1.4	1.4
P_{exit}	0.70		0.8968	0.70
α_{inlet}	-42.	0.0	-42	-42
α_{exit}	-0.004	-0.026	2.064	-0.021
M_1	0.583	–	0.543	0.583
M_2	0.379	0.395	0.374	0.380
M_3	0.715	0.729	–	0.715
Nodes	7602	1565	8006	7613
Cells	14490	2917	15370	14512

Table 5.1: Important flow parameters in various UNSFLO runs.

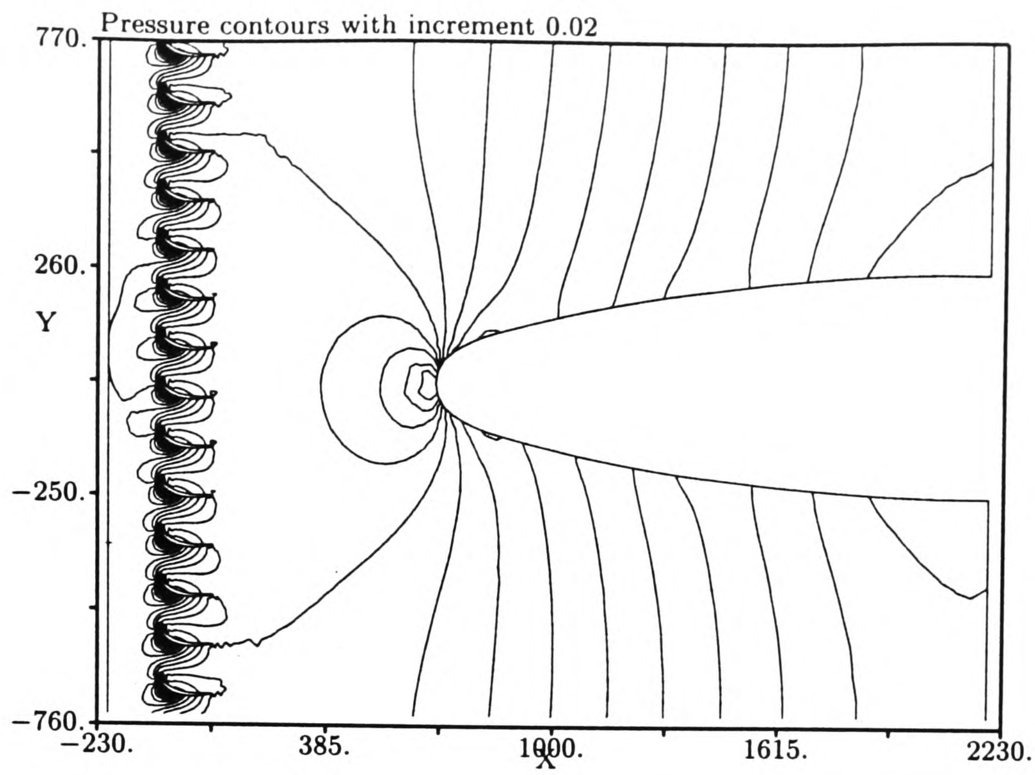

Figure 5.4: Pressure Contours from UNSFLO calculation of initial configuration.

appear as though two pylons and twice as many blades were present. This is in line with engineering conventions and allows easy comparison of the two ends of the curves (which should match). The steps in the redesign include:

i Evaluation of the initial geometry to determine the pressure disturbance that propagates upstream of the OGV's. This analysis was performed using UNSFLO. The computational domain included the OGV's and the pylon. The analysis was performed for $p_3 = 0.7$ (see the previous section for details on p_{1-3}), and M_1, M_2 were determined. To ensure that the following runs were comparable, the desired M_2 was closely replicated by altering the exit pressure boundary condition as required. A plot of pressure contours is presented in fig 5.4 and a circumferential line plot of pressure obtained at the entrance to the computational domain is presented in fig 5.5.

ii Determination of the pressure field of the pylon alone. This analysis is used to determine the pylon induced pressure field, so the calculation is carried out on a grid where the blades are absent. The pressure variation that is obtained at $x = 264$ is the pressure perturbation that is the input to the SLiQ run and the ADisc run. To ensure comparability with the previous run, p_3 is again adjusted in such a way that M_2 is the same as

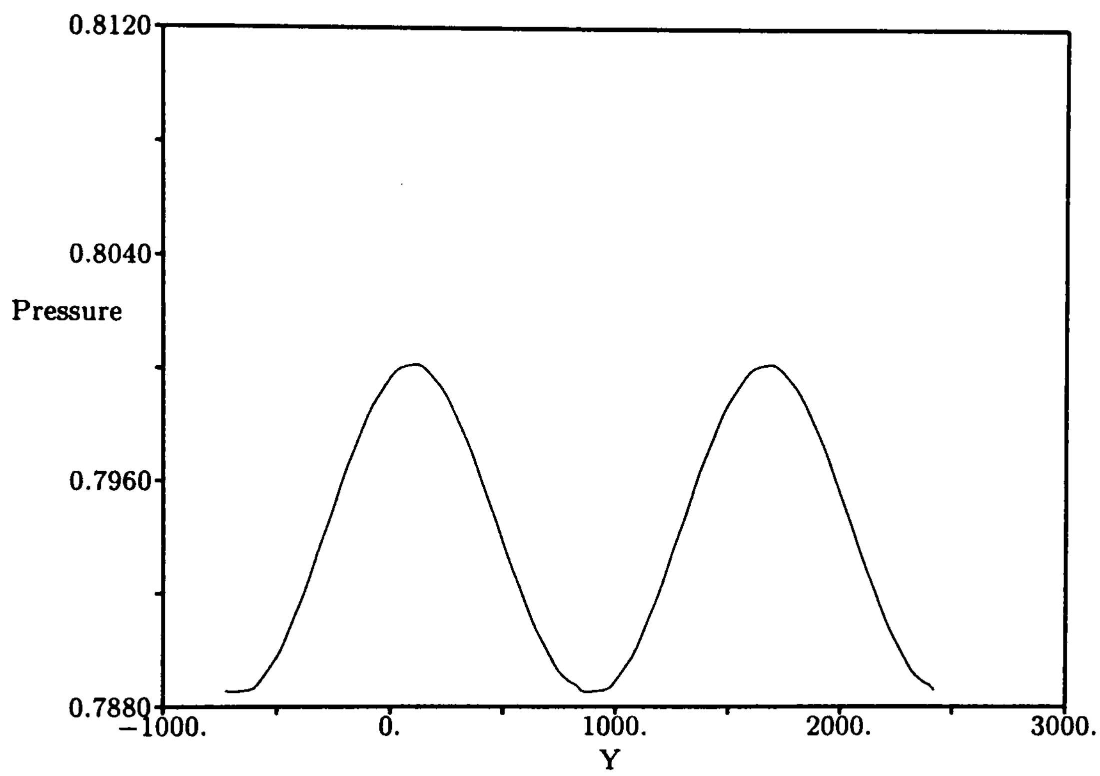

Figure 5.5: Circumferential Line plot of pressure at entry to computational domain at $x = -196$

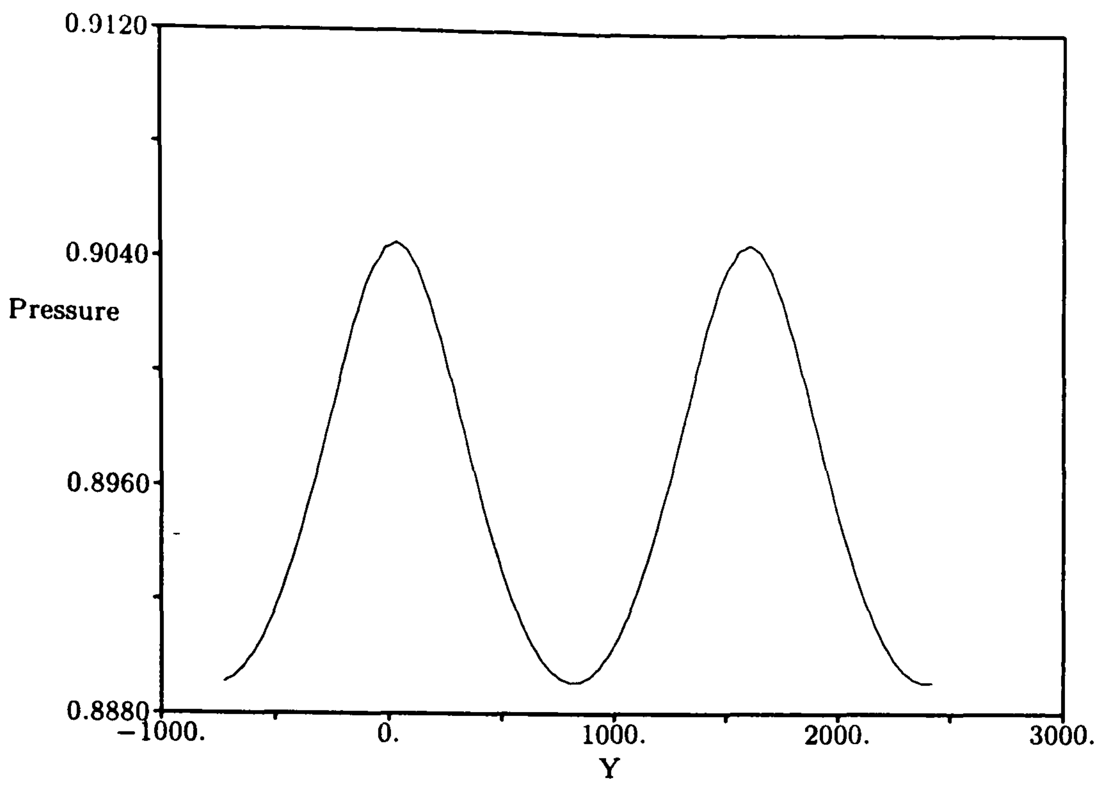

Figure 5.6: Line plot of pressure from UNSFLO measured at $x = 264$ in a "pylon-alone" run. This is used as the exit boundary condition in SLiQ analysis.

before. The line plot of p_2, the pressure measured at $x = 264$ is presented in fig 5.6 (pg 92).

iii A validation of SLiQ is carried out by analyzing the unmodified blades under the influence of the pylon-alone pressure field determined in the previous step. The grid used by SLiQ is presented in fig 5.7 (pg 93). The solution obtained for the single blade passage defines the solution for the whole annulus using equation (3.3). The pressure variation predicted by SLiQ, UNSFLO and ADisc at the entry to the computational domain is shown in fig 5.8 (pg 94). The comparison is excellent. This validates the assumption that the influence of the pylon can be isolated and the redesign carried out on the OGV's alone; ie. the interaction is linear. It also validates the previous step and confirms the possibility of using SLiQ in conjunction with UNSFLO.

iv The success of the previous step confirms the assumption that the problem can be viewed by isolating the OGV's from the pylon. The next step is to determine the sensitivity of pressure to change in camber. SLiQ is used to calculate the linearised effect of a circumferential variation in camber of unit magnitude. Again the calculation is performed using one OGV passage and then the variation in other passages is reconstructed using equation (3.3). The circumferential pressure perturbation

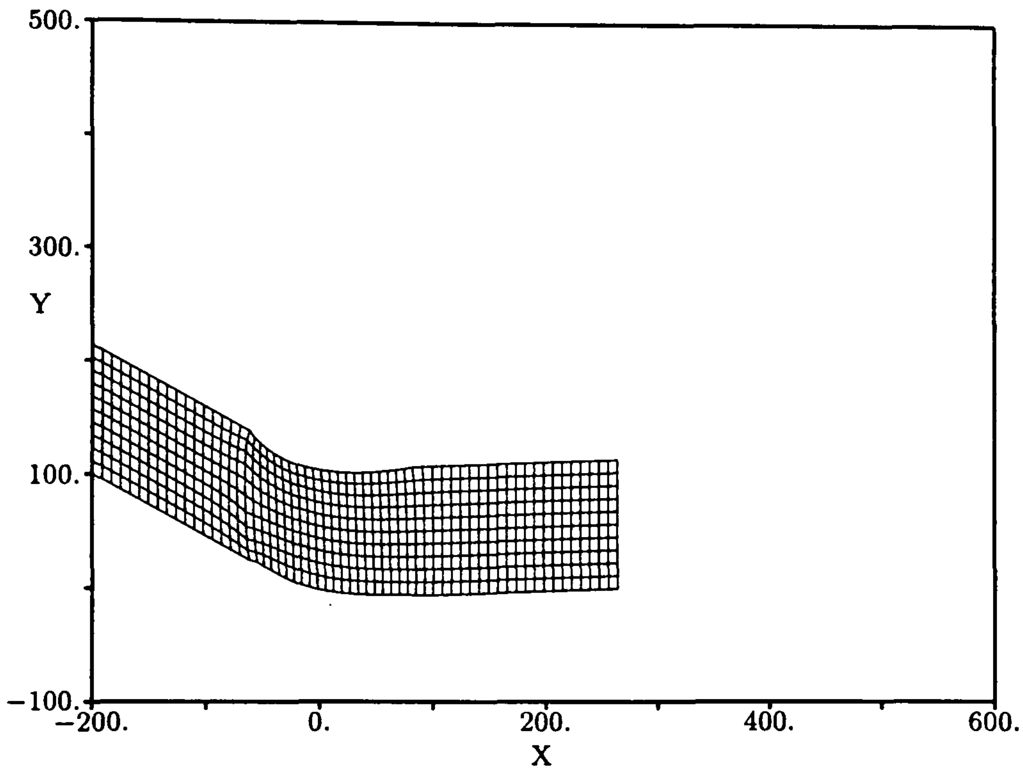

Figure 5.7: SLiQ computational grid for uniform OGV's.

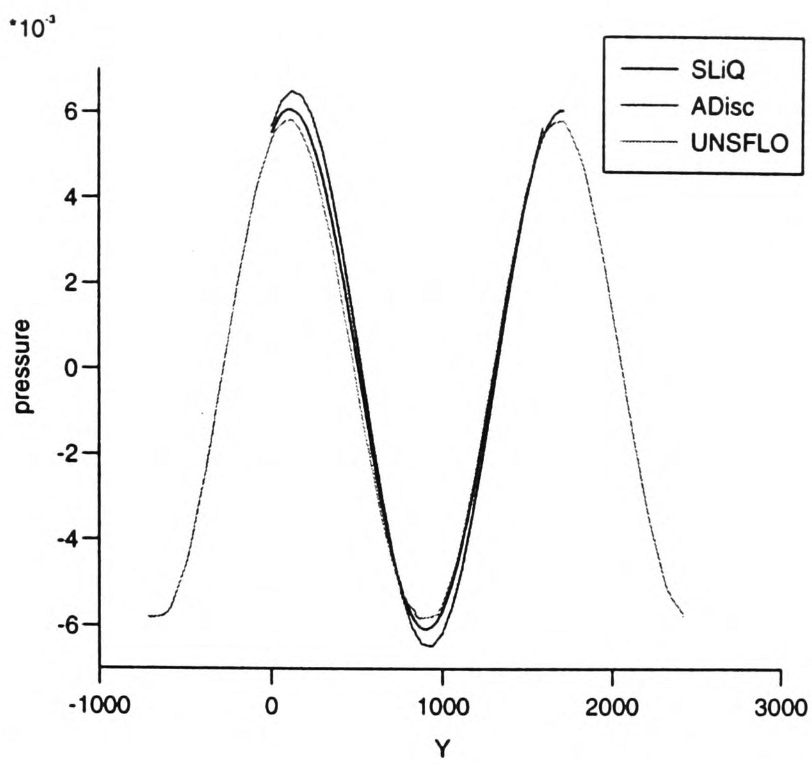

Figure 5.8: Comparison of circumferential pressure variation predicted by SLiQ, UNSFLO and ADisc upstream of OGV's at $x = -196$.

upstream of the OGV's is shown in fig 5.9 (pg 95).

v Using the sensitivity calculated in the previous step, the required change in camber of the OGV blades is determined. This is expressed as a harmonically varying change. The change when applied to the blades, serves to divert the flow around the pylon and therefore reduce the build up of static pressure in front of the pylon. In fig 5.2 (pg 86) the arrows at the trailing edges of the OGV's indicate the direction of suggested changes.

vi For initial verification a computational domain involving just the redesigned blade row is analyzed by UNSFLO. The upstream pressure is compared to the pressure measured at the same location in the uniform OGV configuration. They are required to be equal and opposite. The pressures predicted by UNSFLO, SLiQ and ADisc are presented in fig 5.10 (pg 95).

vii As the final step, the predicted blade geometry is inserted into the OGV pylon grid and analyzed with UNSFLO. This should confirm a complete suppression of the flow upstream of the OGV's. However, the result (plotted in fig 5.11, pg 96) shows a residual pressure variation. When viewed with the pressure variation of the datum OGV row, it becomes

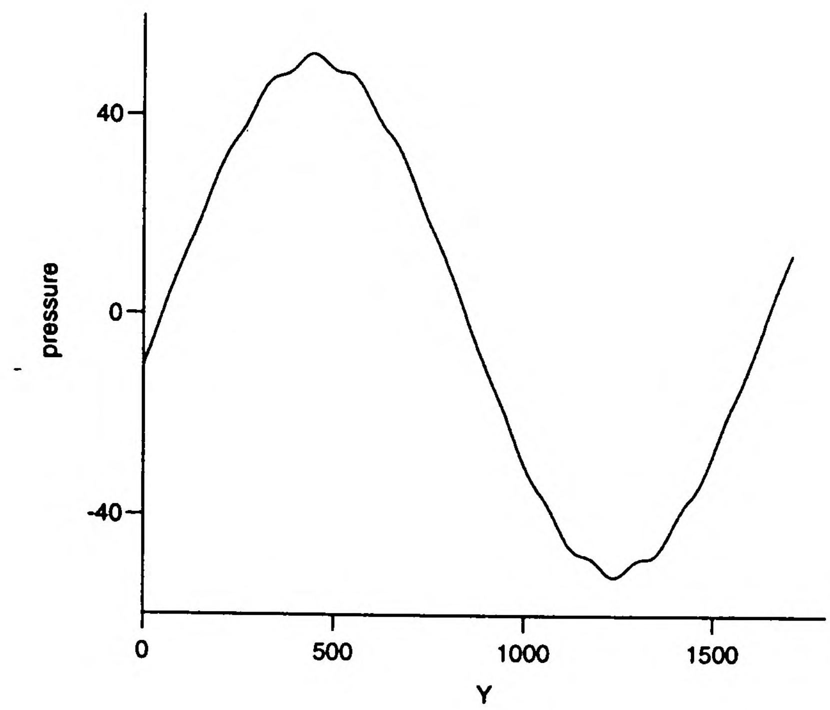

Figure 5.9: Line plot of pressure at inlet to computational domain, at $x = -196$, for a unit perturbation in camber, calculated by SLiQ.

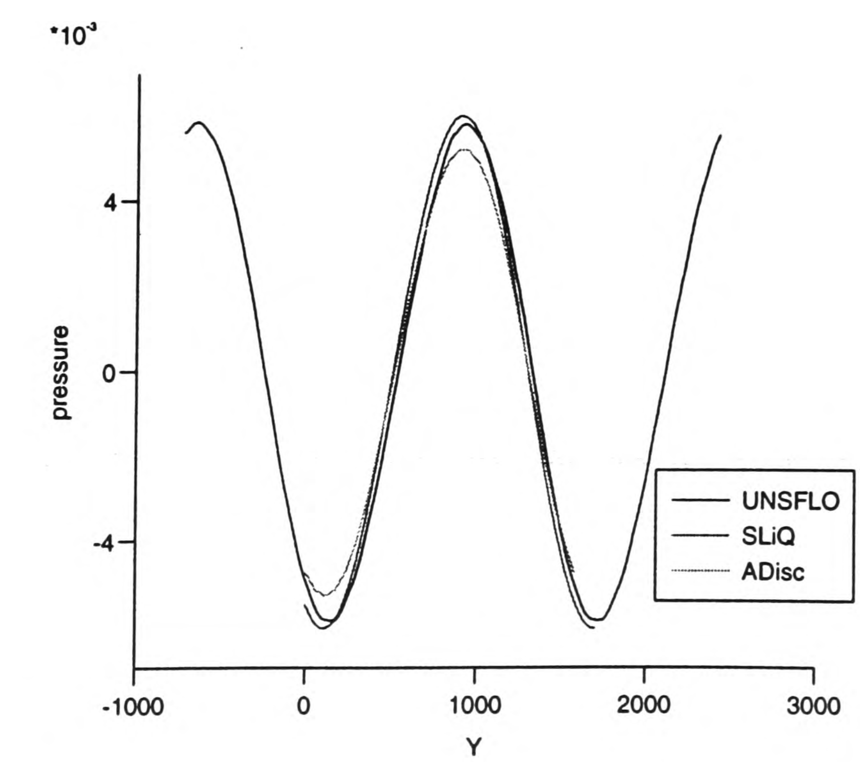

Figure 5.10: Comparison of pressure variation predicted upstream of a cascade of tailored blades, at $x = -196$.

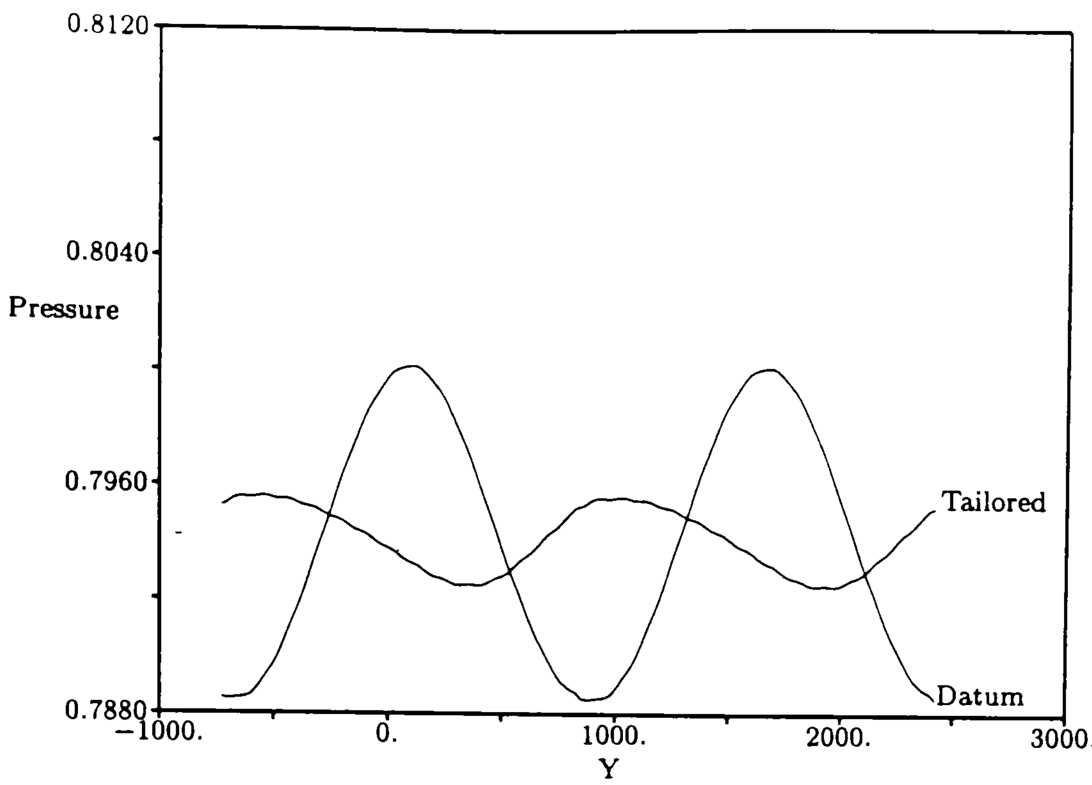

Figure 5.11: Comparison of pressure variations upstream of the OGV row at, $x = -196$, for a OGV-pylon configuration using uniform and tailored blades.

evident that the correction prescribed has "overcorrected" the error.

5.5.1 An Interaction Effect

The reason for the over-correction of the re-designed OGV's was investigated by using UNSFLO to perform a number of nonlinear OGV/pylon calculations. The circumferential pressure variation upstream of the OGV's is plotted in fig 5.12 (pg 98). Each of the three curves represents the difference in pressures obtained from two nonlinear calculations, one using the re-designed OGV's and the other using the original OGV's. The two grids are very similar and the calculations were performed for the same Mach number M_2 as discussed earlier, so the pressure difference corresponds solely to the change in the flow field due to the change in the OGV's. The factor that is different for the three curves is the pylon downstream of the OGV's. One curve corresponds to calculations using no pylon, just the OGV's. A second curve corresponds to calculations using the regular (thick) pylon. The third curve uses a thin pylon of half the thickness of the regular pylon.

The results show that the pressure perturbation due to recambering the

OGV's is greater in the presence of the thick pylon than with the thin pylon or no pylon at all. The linear SLiQ analysis corresponds to a linearisation of the nonlinear calculation without the downstream pylon. Using the SLiQ analysis to design the recambering produces modified OGV's which, in the presence of the thick pylon, will then produce too large a pressure change, over-correcting the original pressure disturbance due to the pylon. The results in fig 5.12 (pg 98) are therefore consistent with the observed over-correction.

The cause of the results in fig 5.12 (pg 98) is less clear. There are two possible explanations. The first is a feedback phenomenon. The change in the OGV camber produces flow field changes downstream of the OGV as well as upstream. In the absence of a downstream pylon, the downstream changes are irrelevant, but when there is a pylon it may cause a 'reflection' of the disturbance producing a new, although much smaller, pressure perturbation which will affect the OGV's. The magnitude of the reflection will depend on the thickness of the pylon, because it can be shown mathematically that in the limit in which the pylon becomes a flat plate there is no reflection.

The second possibility is nonlinear effects. The whole basis of the linear approach using SLiQ is that the separate pressure perturbations due to the pylon and the re-cambering of the OGV's can be linearly superimposed. In practice, this is not strictly correct since the equations are nonlinear. The magnitude of the error will be proportional to the product of the two perturbations, and so will be roughly proportional to the thickness of the pylon.

Despite the over-correction the design approach has been successful in greatly reducing the pressure variation upstream of the OGV's. If even more reduction is needed, the next step would be to use the results of the nonlinear analysis giving the remaining pressure variation; feeding these into a further iteration of the design process would give an additional much smaller camber perturbation to eliminate the majority of the remaining pressure perturbation.

5.5.2 Engineering Issues Regarding Number of Blades

One problem with this design procedure is that it generates a set of OGV's each of which is unique. This leads to unacceptable additional costs both in the manufacture of the OGV's and in the airlines' costs of inventory maintenance. A practical compromise is to use a limited number of different OGV's; for

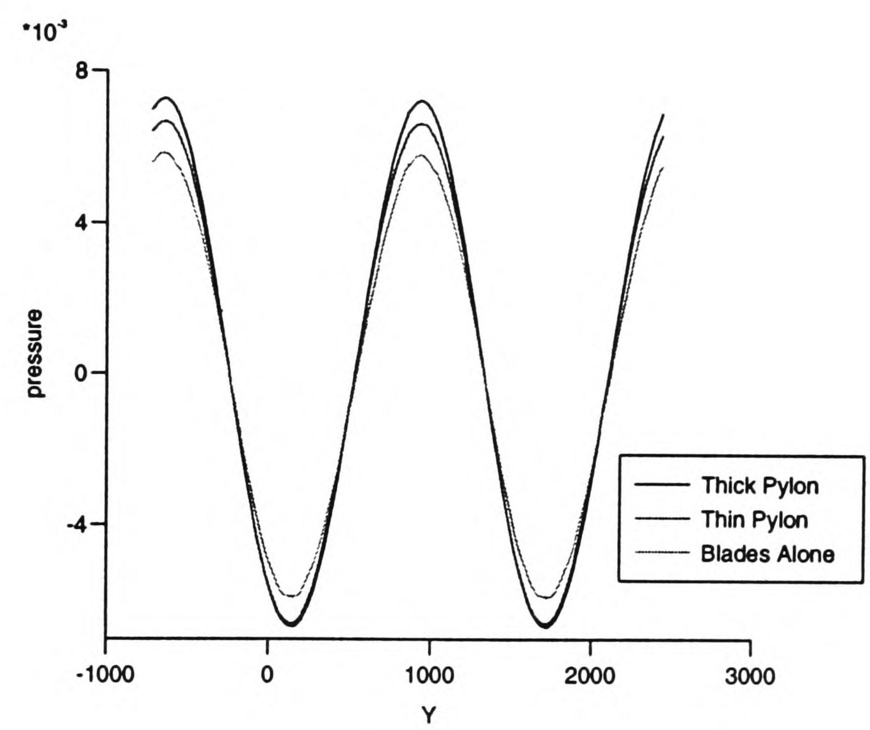

Figure 5.12: Influence of pylon size on upstream pressure changes due to re-cambering

example three, one with the datum exit flow angle, one with overturning and one with underturning. These can then be grouped and collectively designed to completely cancel the first circumferential harmonic of the pressure field generated by the pylon. The design can still be performed using the linear tools described in this paper. The OGV trailing edge flow angle is now a square wave function, corresponding to the different groups of blades. This square wave can be decomposed into a sum of circumferential harmonics, each of which can be analyzed separately with its own steady interblade phase angle. By linear superposition the results can then be combined to give the overall perturbation flow field. Linear scaling of the geometric perturbation will then lead to cancellation of the first harmonic of the upstream pressure perturbation. Additional harmonics can also be eliminated using a larger number of different blades. However, this may be unnecessary since these higher harmonics decay axially at a faster rate and so are less likely to adversely affect the fan.

5.6 Redesign by the quasi-Newton Approach

The flow calculations are performed here using a parallelised Euler solver as discussed in section 4.3 (page 66). The move to a parallelised Euler solver was necessitated by the fact that UNSFLO does not include acceleration techniques such as multigrid or parallel processing. Turn around times were considerably reduced by using the new Euler solver. Since the current Euler solver did not have non-reflecting boundary conditions implemented, the computational domain was extended into the upstream flow field to damp spurious reflections in the solution. The flow variable of interest here was the pressure at $X = -196$. The design parameter was C_c as in eqn(5.1) but assuming C_c was purely imaginary, ie

$$\Delta y = C_c^\star (X - X_{le})^2 \sin(ky) \tag{5.6}$$

where $C_c = iC_c^\star$ The sensitivities were obtained by finite differencing the flow variation with C_c. The Euler solution was obtained on a grid modified by the grid movement algorithm (discussed in section 4.2). The flow field around the datum geometry is first computed then the blade geometries are perturbed by a specified amount and the new flow field is obtained. The pressures obtained from these solutions are finite differenced to obtain the sensitivity. These sensitivities are used in eqn(4.14) to determine the next point in the design space. This was performed iteratively till no further changes in the design parameters were predicted by the Newton method.

5.6.1 Numerical experiments

A redesign of the OGV row was attempted using the Newton method. The reduction in pressure variation achieved was very impressive. The pressure variations are presented in fig 5.13 (pg 101). The first step predicted by the Newton scheme achieved a reduction of over 86% (curve sf-1 in fig 5.13. The second step made a minor correction and resulted in a small increase, decreasing the pressure suppression to 85% (curve sf-2 in fig 5.13). No further reduction was achieved. The reduction of the pressure variation normalised with respect to the initial variation is shown in fig 5.14 (pg 101).

5.6.2 Engineering Issues Regarding Number of Blades

As before, the problem with this design procedure is that it generates N different blade shapes leading to unacceptable additional costs. The practical compromise is to use a limited number of different OGV's; for example three, one with the datum exit flow angle, one with overturning and one with underturning. These can then be grouped and collectively designed to completely cancel the first circumferential harmonic of the pressure field generated by the pylon.

Such a design was attempted using the grouping of blades shown in Figure 5.15 (pg 102). The magnitude of change in flow exit angle was the same for the overturning and underturning blades so again there is just one design variable. The first step of the Newton scheme achieves a 72% reduction in the pressure variation. Subsequent iterations make minor corrections with the final figure at 73.8%. The pressure plot is presented in fig 5.16 (pg 103) and a plot of the pressure variation index is presented in fig 5.17 (pg 103). These results are extremely encouraging since the current design is "practical" and can easily be used in a industrial environment.

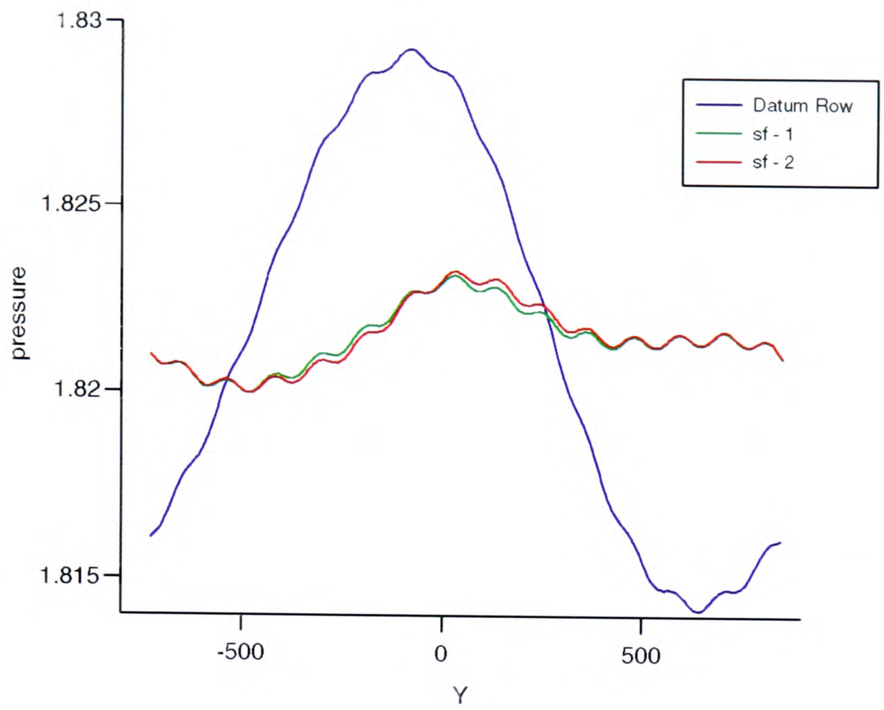

Figure 5.13: Plot of circumferential pressure variation for continuously varying camber case.

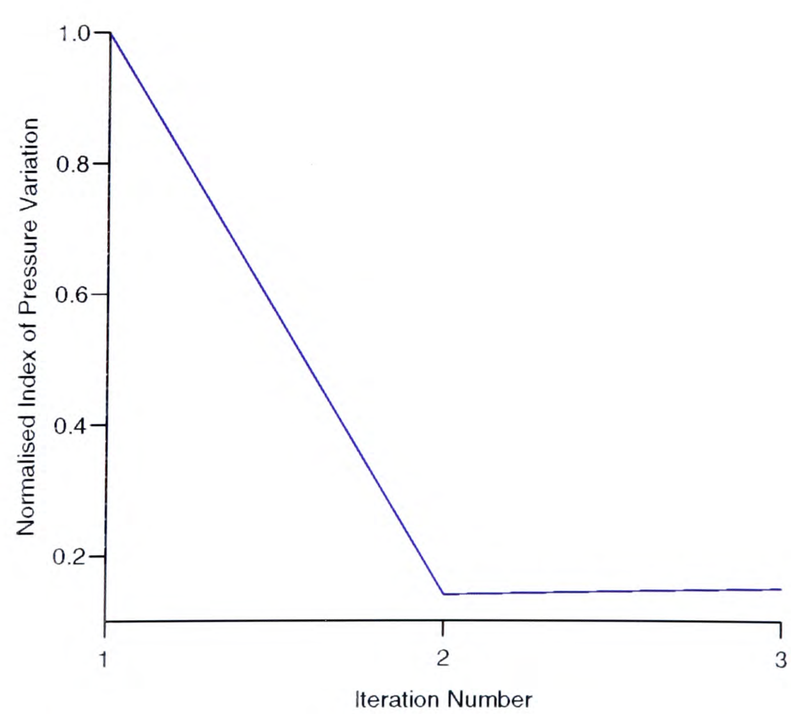

Figure 5.14: History of pressure variation for the continuously varying camber case.

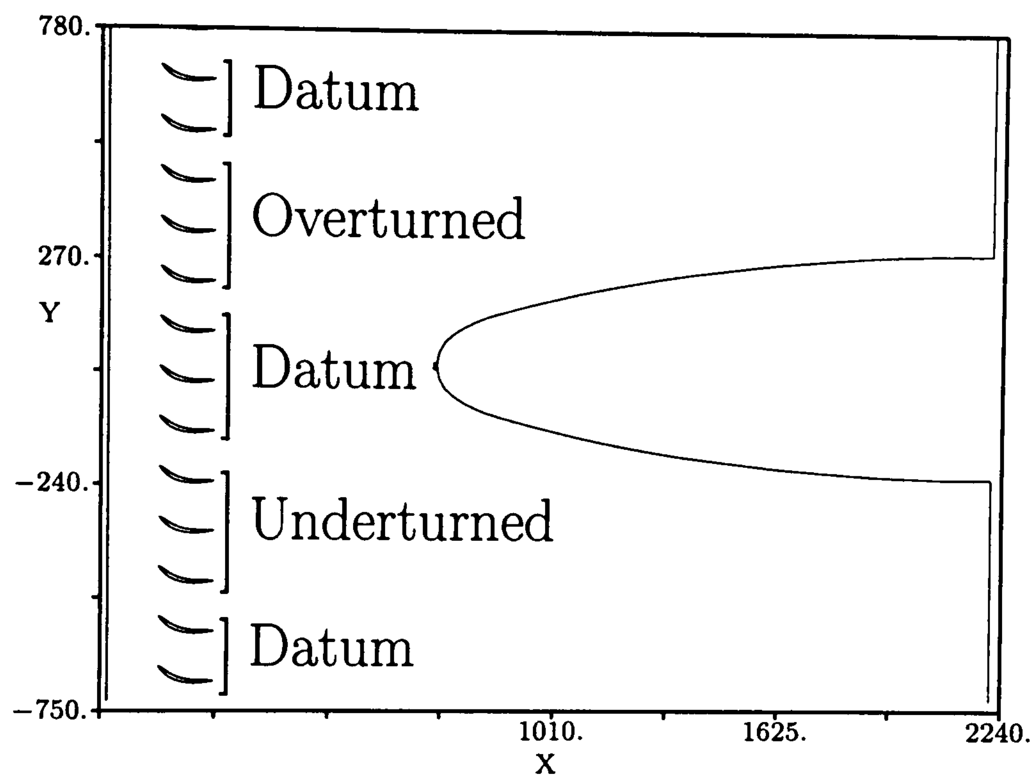

Figure 5.15: Grouping of blades for 3 blade case.

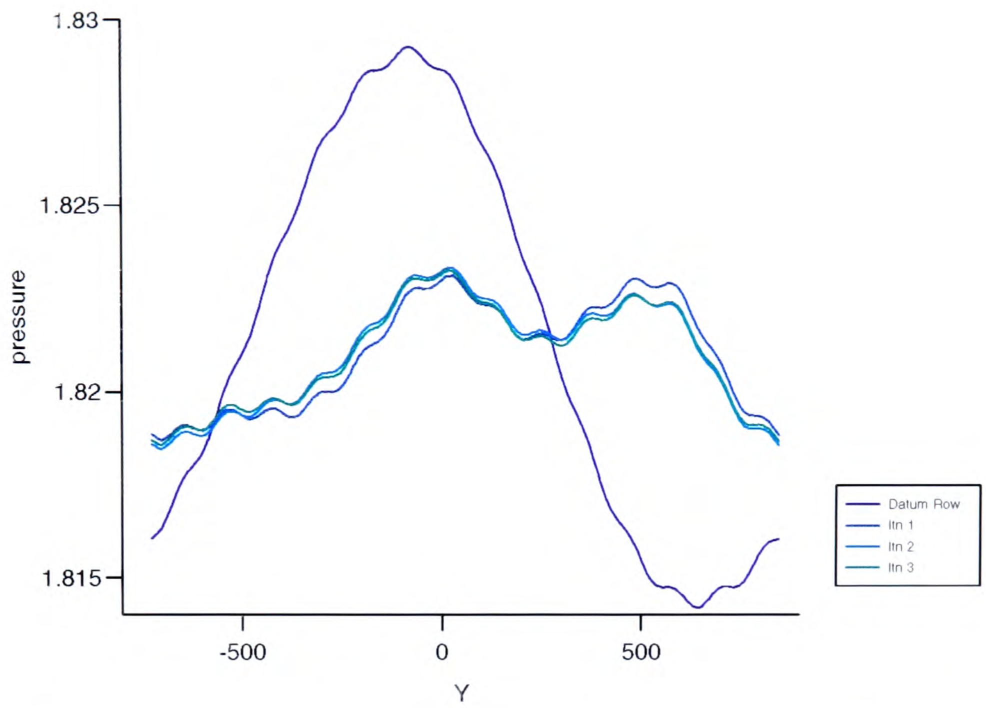

Figure 5.16: Plot of circumferential pressure variation for 3 blade case.

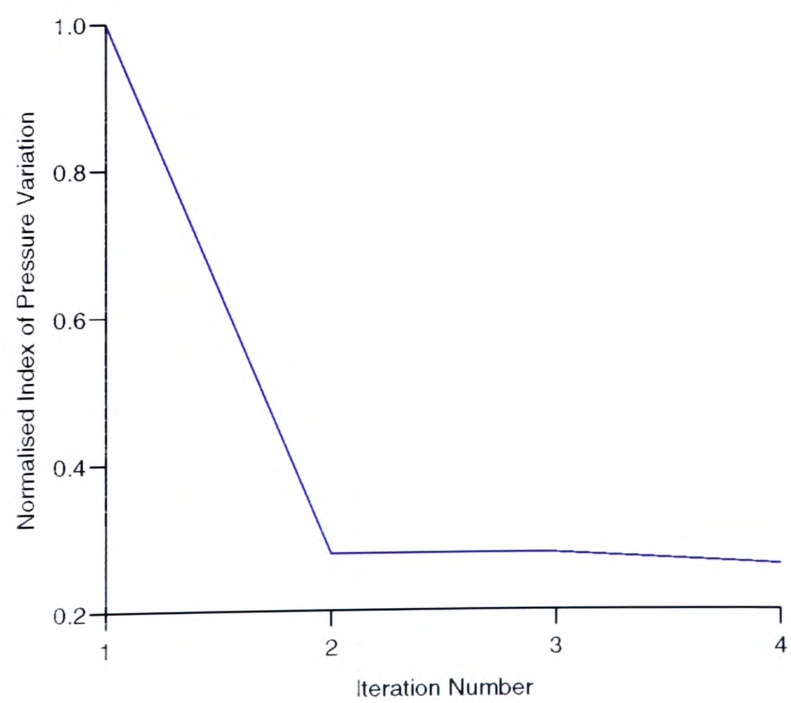

Figure 5.17: History of pressure variation for the 3 blade case.

Chapter 6

Redesign of a 3D Blade Row

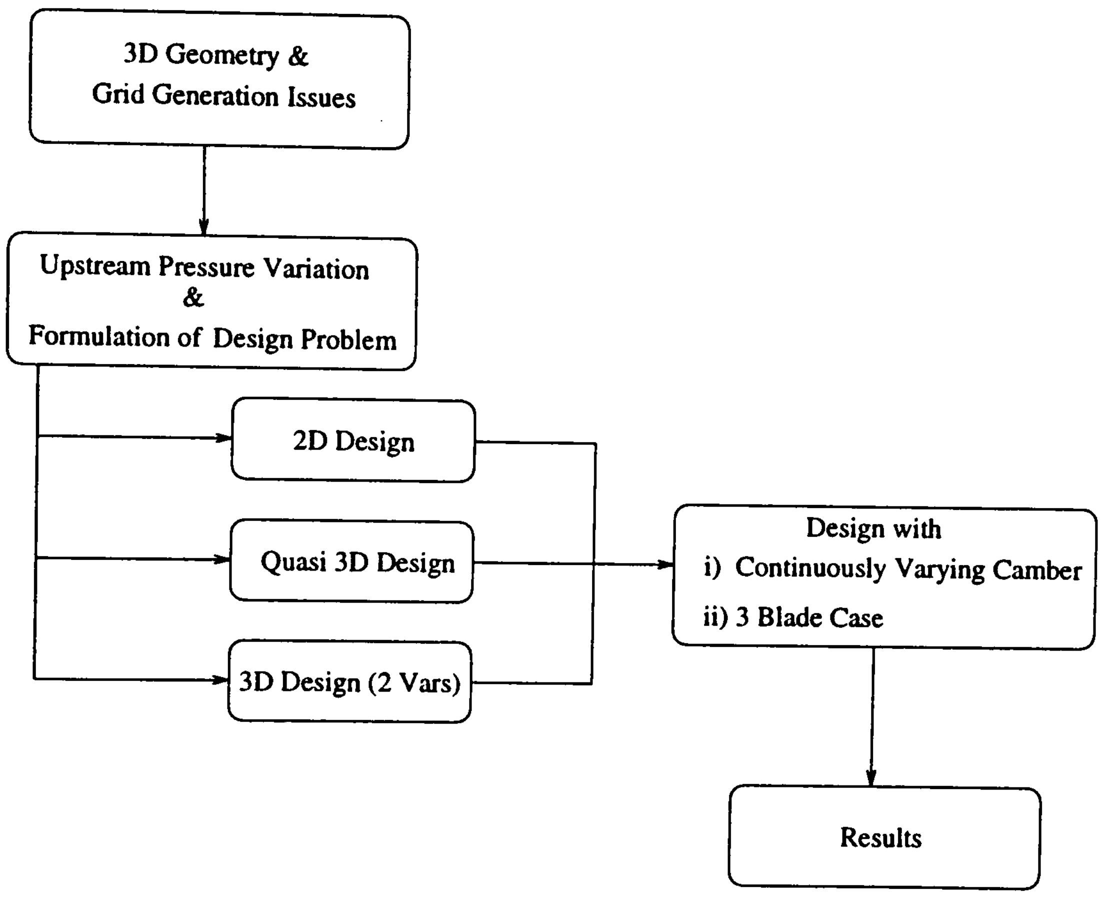

Figure 6.1: Flow chart of Chapter 6.

6.1 Introduction

In the previous chapter we studied the redesign of OGV's in two dimensions. Inherent in such an approach is the belief that the pressure perturbation does not vary with radius and in the event that it is a function of radius, a set of 2D designs can be "stacked" to obtain a 3D design. For the want of a suitable design method and computing resources, designers have often resorted to the stacking approach to circumvent radial variation in flow conditions. Such approaches neglect the three dimensionality of the flow and are inaccurate. In this chapter we evaluate a fully three dimensional design method in conjunction with 2D methods. The 3D method discussed in this chapter is identical to the quasi-Newton method implemented in 2D in the previous chapter. In this chapter we will use a full 3D configuration in conjunction with 3 different approaches to design. These approaches are: (a) two dimensional, (b) quasi-three dimensional (the stacking idea) and (c) three dimensional. These methods differ essentially in their approach to gradient evaluation.

3D design methods become important when there is sufficient three dimensionality in the flow field. This three dimensionality can be due to many sources, the curcial ones being:

(i) Pylon "lean". This refers to the three dimensional design of the pylon where the geometry varies as a function of radius. The "lean" angle is the angle of the pylon leading edge w.r.to the vertical (similar to the sweep angle of a wing).

(ii) Asymmetric inlet flow conditions. Depending on the airframe-engine integration, it is possible for the engine to be subjected to a severe cross wind.

In this chapter we will concern ourselves with the influence of pylon lean.

6.2 Geometry & Grid Generation

A three dimensional bypass duct based on the pylon-OGV configuration was developed from the following information (which reflects standard engine configurations):

- The two dimensional grid (used in the previous chapter) corresponds to the configuration at the hub.
- (Radius at Tip) / (Radius at Hub) = 1.36.
  This ratio was obtained from other engines. The values for the current case are: $R_H = 250.446$ and $R_T = 340.60$.

- An extreme lean of 20 degrees was assumed for the pylon.
- A linear variation (as a function of radius) in geometric parameters from hub to tip was assumed.

The outlines of the hub and tip configurations are presented in figure 6.2.

The grid for the above configuration was generated by the following steps:

- A two dimensional grid of the hub was generated using an advancing front grid generator [52].
- The coordinates of boundary nodes for the tip case were computed from the tip dimensions and the distribution of boundary nodes on the hub grid. This was performed by a modified advancing front grid generator with the help of a startup file that contained the hub boundary node distribution information.
- These tip coordinates were used as input to move the hub grid to a tip grid. The grid movement algorithm (described in section 4.2 computed the nodal displacements necessary to move obtain a tip grid from a hub grid.
- Two dimensional grids for 8 radial locations between hub and tip were generated by linearly interpolating between the hub and tip grids.
- These two dimensional grids were stacked and corresponding triangles were connected to form prisms which were then subdivided to give a valid tetrahedral grid. The grid was then wrapped around to form an annulus and the cyclic boundary was deleted with additional reordering of node and cell information to give the desired cylinderical geometry. The computational programs used were due to Dr. P. Crumpton. A view of the final geometry is presented in figure 6.3.
- The edge collapsing algorithm [14] was used to generate coarse grids for the multigrid flow solver. Grid information for various grid levels is provided in table 6.1.

Grid	Nodes	Cells
2D Hub	10787	20715 (Triangular)
3D 3	3326	10410 (Tets)
3D 2	12736	56685 (Tets)
3D 1	106570	559305 (Tets)

Table 6.1: 2D and 3D grid sizes.

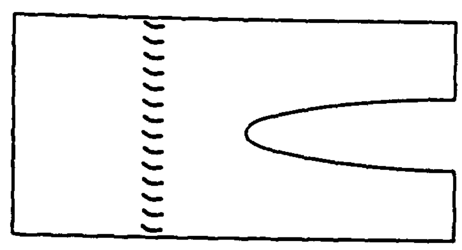

(a) Hub

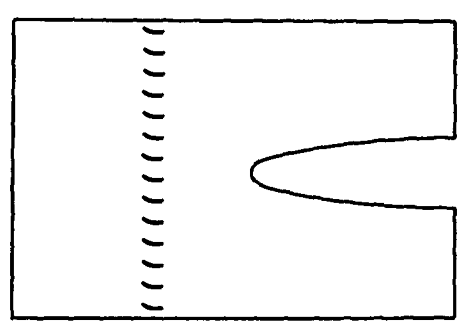

(b) Tip

Figure 6.2: Hub and Tip profiles demonstrate the change in geometry due to radius.

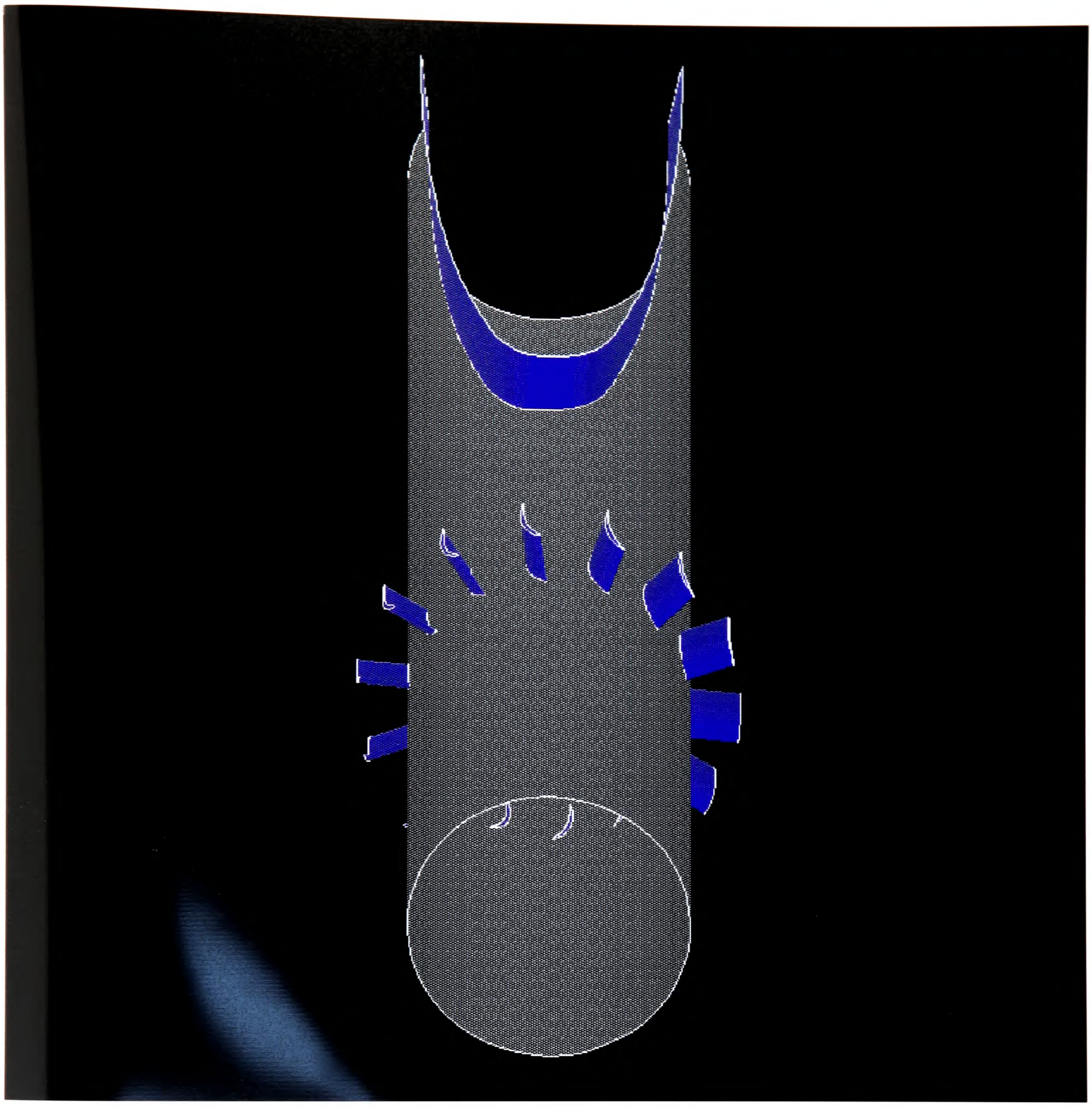

Figure 6.3: A view of the three dimensional geometry.

6.3 Formulation of the Design Problem

The pressure variation measured at the fan trailing edge ($x = -198$) at three different radial locations (hub, mid and tip) are presented in figure 6.4. The lower peak of the tip curve is due to the increased distance (because of pylon lean) between the pylon and the fan trailing edge. It can be concluded from the above figure that the effect of pylon lean is not drastic and the redesign can be addressed through two dimensional methods with suitably altered geometries. However, it is not clear whether it is that lack of three dimensional design methods that has prompted the design of very "2D" geometries such as the one adopted as a test case in this thesis. It is possible that 3D design methods might be provide the design engineer with that extra tool to attempt innovative solutions to design issues. A comparison of various design approaches will be a very interesting pointer to their effectiveness in tackling major design problems.

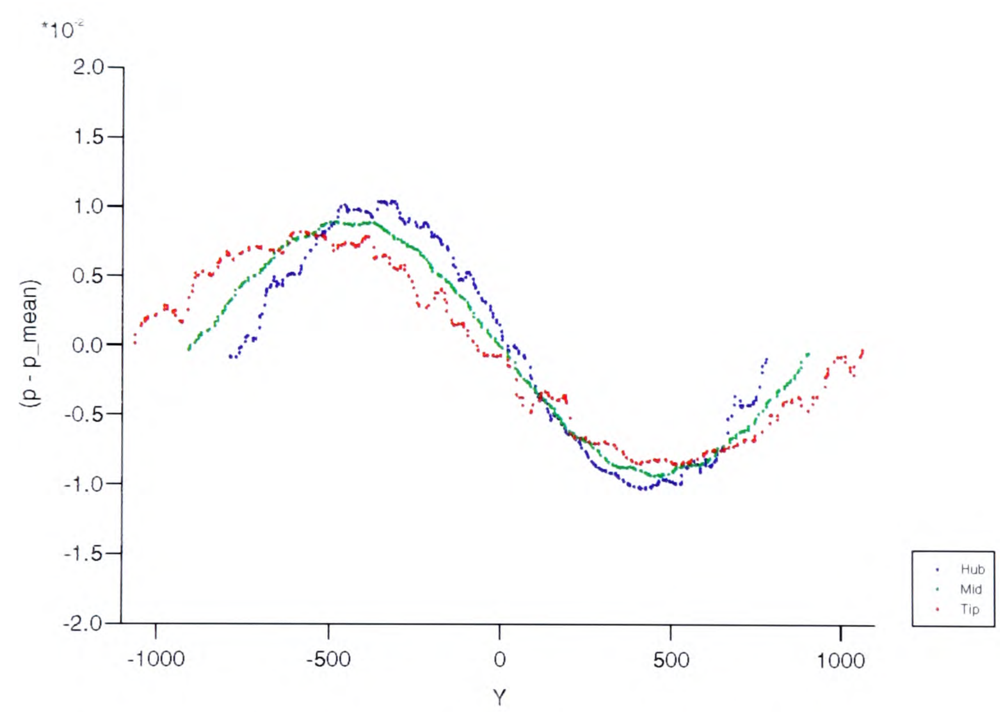

Figure 6.4: Pressure variation at fan trailing edge measured at three different radial locations.

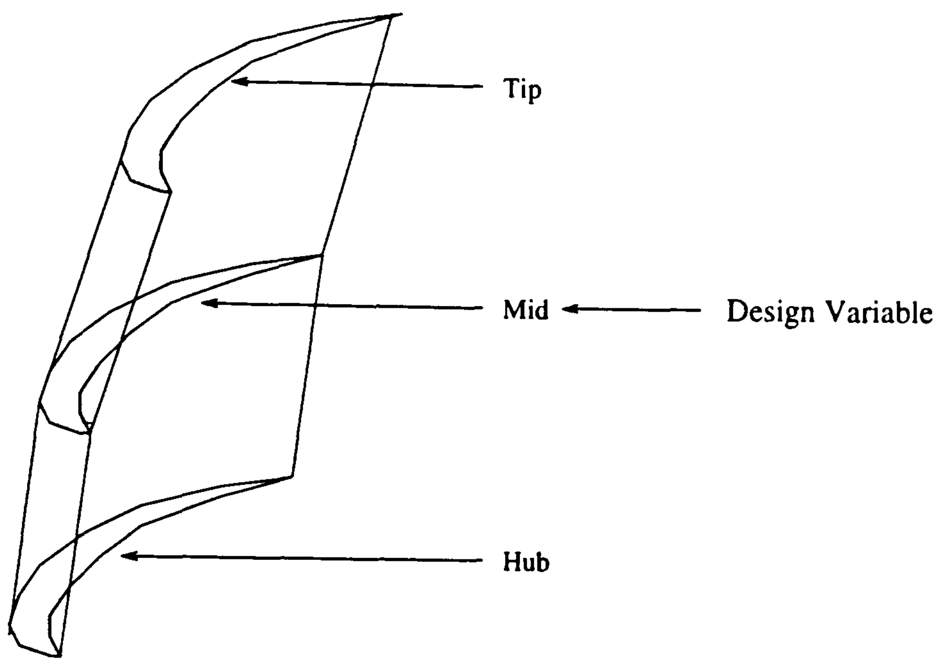

Figure 6.5: Design: location of design variables. Note, figure is schematic only.

The different philosophies are:

2D design: Here a 3D flow solution is obtained over the geometry but the pressure mismatch integral is evaluated at one radial location (ex. mid). All design perturbations are computed from this integral and are applied uniformly along the whole length of the blade thus making it a two dimensional design method (see figure 6.5, pg 112). There is only one design variable for the blade (also the blade row, due to the harmonic nature of the problem, see section 5.2). *To determine the sensitivity, the whole blade is perturbed by a constant amount and the flow field is determined around the new geometry, then the gradient is computed by finite differencing.* This approach will provide interesting insight into the three dimensionality of the flow field. In the extreme case of a 2D flow, the percentage reduction in the pressure mismatch will be identical at all radial locations. It will also serve as useful comparison to evaluate the 3D method.

Quasi-3D design: If there is sufficient three dimensionality in the flow field the design will need to include this effect in the blade shape, which will be a function of radius. However, it is possible that the three dimensionality is due to external causes and the flow field within the passage is two dimensional, ie. any geometric perturbation at the tip will have no effect on the flow at the hub. Thus, the design can be driven by just one design parameter that has different values at different radial locations. This is identical to the idea of stacking several two dimensional designs to obtain the 3D geometry. *For computing the sensitivity we need to compute the flow around the perturbed geometry only once (where the whole blade is perturbed uniformly,* this is possible because the zone of influence of the geometric perturbation is confined to the current radial location, and thus every cross section is independent of the others and can be evaluated at the same time. It should be noted here that, such a method will lead to three dimensional geometries (ie. will produce "twisted" blades).

3D design: This is the truly three dimensional design approach. Like the previous two cases, it is based on a full 3D flow solution, but unlike them the geometric design parameters at different cross sections are treated as independent design variables. So a perturbation at the tip is assumed to have an influence on the flow at the hub. *Thus, for sensitivity calculations one needs N flow solutions in addition to the solution around the current design point (where N is the number of design variables, ie. independent cross sections considered).* The result of such a design process is a truly three dimensional blade that can take into account distortions in the flow field due to external and internal sources.

In the current design exercise the camber perturbations used were identical to those used in the two dimensional design exercise in the previous chapter. The design objective was to obtain the constant C_c that induces the lowest I, where I is the pressure deficit integral.

The actual implementation issues are discussed in the following section where the results of computational experiments are also presented.

6.4 Results

The flow solutions were obtained on an IBM SP2 and a SGI PowerChallenge using a "parallel" Euler solver. The CPUs for both these machines are comparable in number crunching speeds. However, due to the different architectures (SP2 is a distributed memory machine, while the Challenge is a shared memory machine) the execution times of the solvers were slightly different. The grid movement was performed by a "serial" code which was run on a single processor of the Challenge, and included a full multigrid startup, it took approximately 45 minutes of CPU time. The execution time for the Euler solver depended on the mechanism used to initialise the flow field, there were three types:

(a) The base flow solution. This flow solution was obtained only once and is the analysis run around the datum geometry. The Euler solver required 386 multigrid (MG) iterations to reduce the residual of error to less than 1.0E-08. This corresponds to about 4 hours of wall clock time on a 4 node SP2. This run had a full MG startup where the flow field was initialised to the inlet flow conditions.

(b) Flow solution at a new point in design space. The flow solver was restarted with the base flow solution as the initial guess. Such a solution took about 240 MG iterations that corresponds to $2\frac{1}{2}$ hours of CPU time on a 4 node SP2.

(c) Flow solution at perturbed geometry – used to evaluate sensitivity. For such a solve the flow solution at the current point in design space was used as the initial guess. The Euler solver took about 110 MG iterations to solve this case, this corresponds to 1 hour of CPU time on a 4 node SP2.

In the base flow solution no restart file was provided, the Euler solver used the inlet flow condition as the initial solution and thus needed more iterations to determine the solution. Similarly, it can also be observed from the above data that the base flow field is not a very good guess for the redesigned flow field, and the solver needs a larger number of iterations to calculate the flow field at a new point in the design space. A clear indication that the design process is altering the flow field.

6.4.1 A 2D Design

Here the two dimensional approach described in the previous section was applied to the test case. The pressure deficit was evaluated at the mid radial location and all geometric perturbations were applied uniformly along the span of the blade. The design target was to minimise the pressure deficit at mid-point. Pressure variations and convergence plots of the pressure deficit are presented in figures 6.6-6.7. The pressures in these figures are measured at the mid radial location. In tables 6.2-6.3, the value of the pressure deficit integral is presented along side the absolute value of the design parameter (C_c). The present method has only one design parameter that is constant throughout the blade span, which is presented in the table under the midspan entry.

Design mode	Location	Itn 0	Itn 1	Itn 2
	Hub	20.0	1.92	1.89
2D	Mid	20.6	1.64	1.62
	Tip	21.7	2.17	2.18
-	Hub	20.0	3.04	1.96
Quasi-3D	Mid	20.6	3.21	1.69
	Tip	21.7	3.80	2.20
	Hub	20.0	1.70	1.41
3D	Mid	20.6	1.40	0.99
	Tip	21.7	2.47	2.14
	Hub	20.0	4.48	4.31
3D-3Blade	Mid	20.6	4.54	4.36
	Tip	21.7	5.11	4.95

Table 6.2: Measure of pressure variations for various cases.

Design mode	Location	Itn 0	Itn 1	Itn 2
2D	Hub	0.00	–	–
	Mid	0.00	1.1E-04	1.11E-04
	Tip	0.00	–	–
Quasi-3D	Hub	0.00	1.31E-04	1.16E-04
	Mid	0.00	1.18E-04	0.99E-04
	Tip	0.00	1.34E-04	1.14E-04
3D	Hub	0.00	-1.37E-04	-0.68E-04
	Mid	0.00	–	–
	Tip	0.00	3.63E-04	2.94E-04
3D-3Blade	Hub	0.00	0.487E-03	0.516E-03
	Mid	0.00	–	–
	Tip	0.00	-0.214E-03	-0.253E-03

Table 6.3: Magnitude of design variable for various cases.

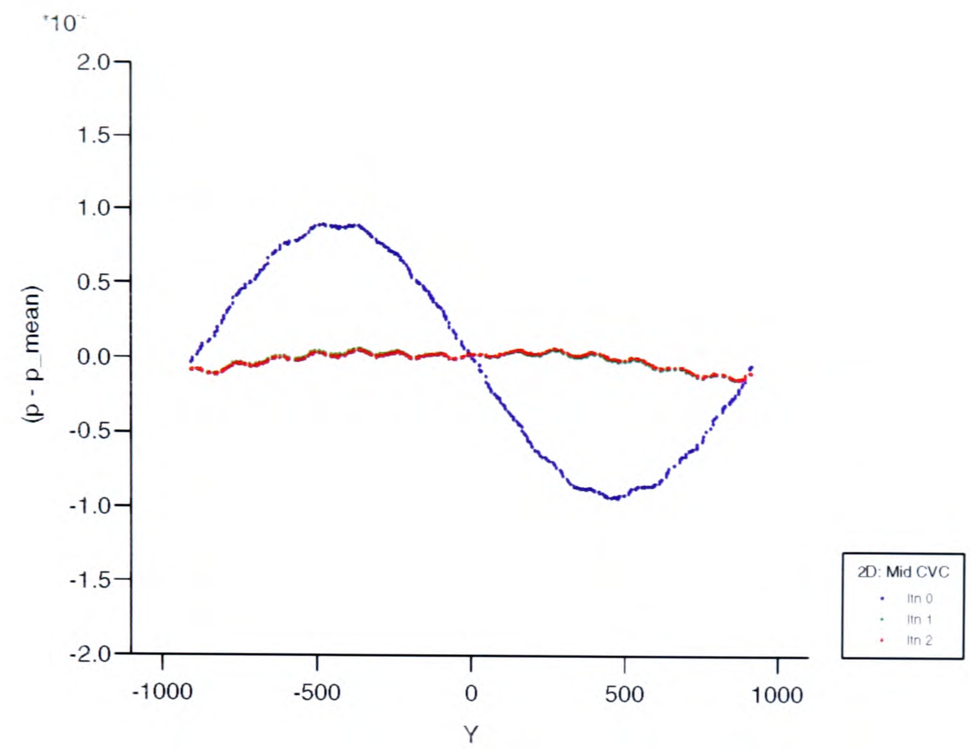

Figure 6.6: 2D Design: Circumferential pressure variation at **mid** for continuously varying camber case.

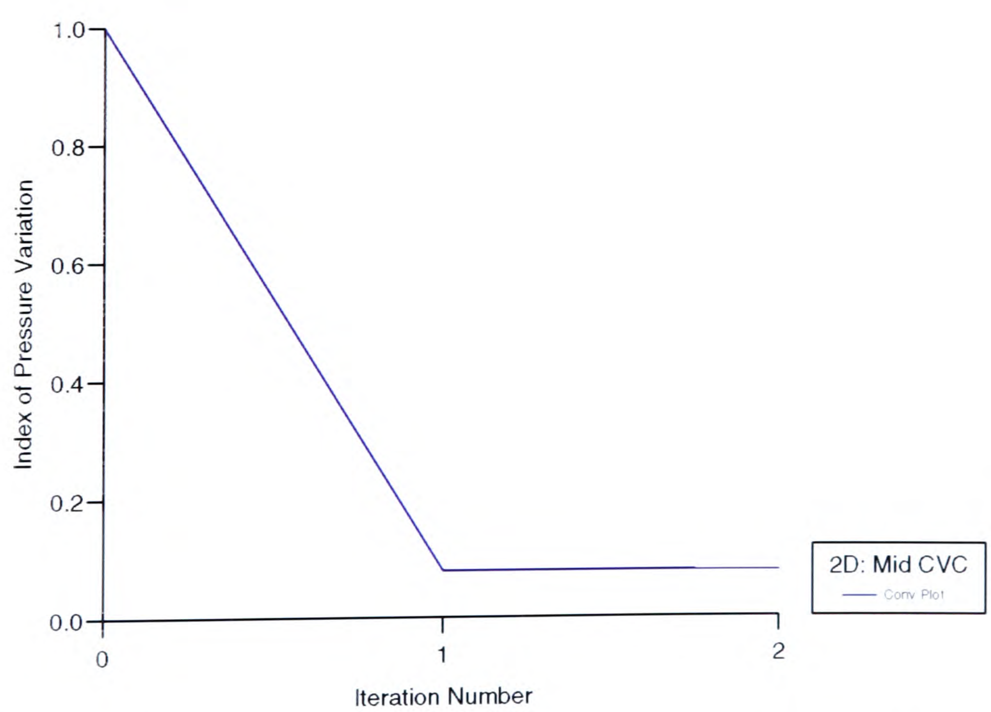

Figure 6.7: 2D Design: History of pressure variation at **mid** for the continuously varying camber case.

6.4.2 A Quasi-3D Design

In this approach, it is assumed that the hub, mid and tip radial locations can have different values of C_c. However, the sensitivity computations involve only one flow solution in addition to the current design. For this additional flow solution, the current design is uniformly perturbed by a constant amount and the flow field evaluated. Pressure variations and convergence plots of the pressure deficit are presented in figures 6.8-6.13. The pressures in these figures are measured at the hub, mid and tip radial location respectively. In tables 6.2-6.3, the value of the pressure deficit integral is presented along side the absolute value of the design parameter (C_c). The present method has different values associated with the design parameter at different radial locations, these values are presented under the hub, mid and tip entries. The design variable is assumed to have a linear variation in between the cross sections that are evaluated by the design process.

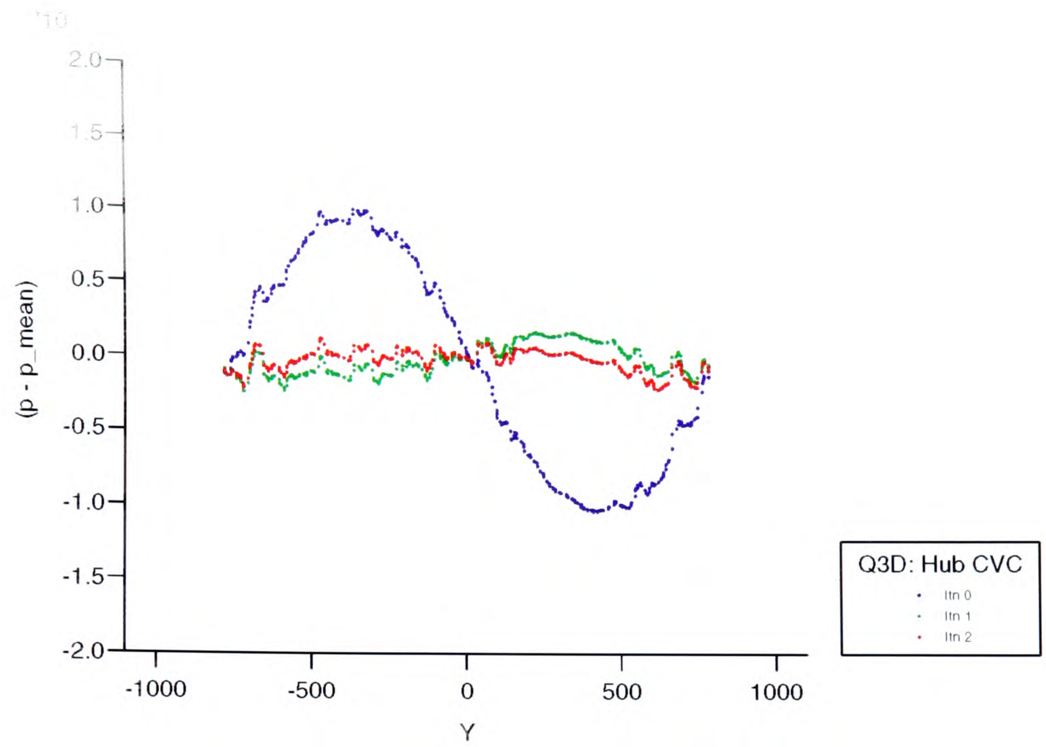

Figure 6.8: Quasi-3D Design: Circumferential pressure variation at **hub** for continuously varying camber case.

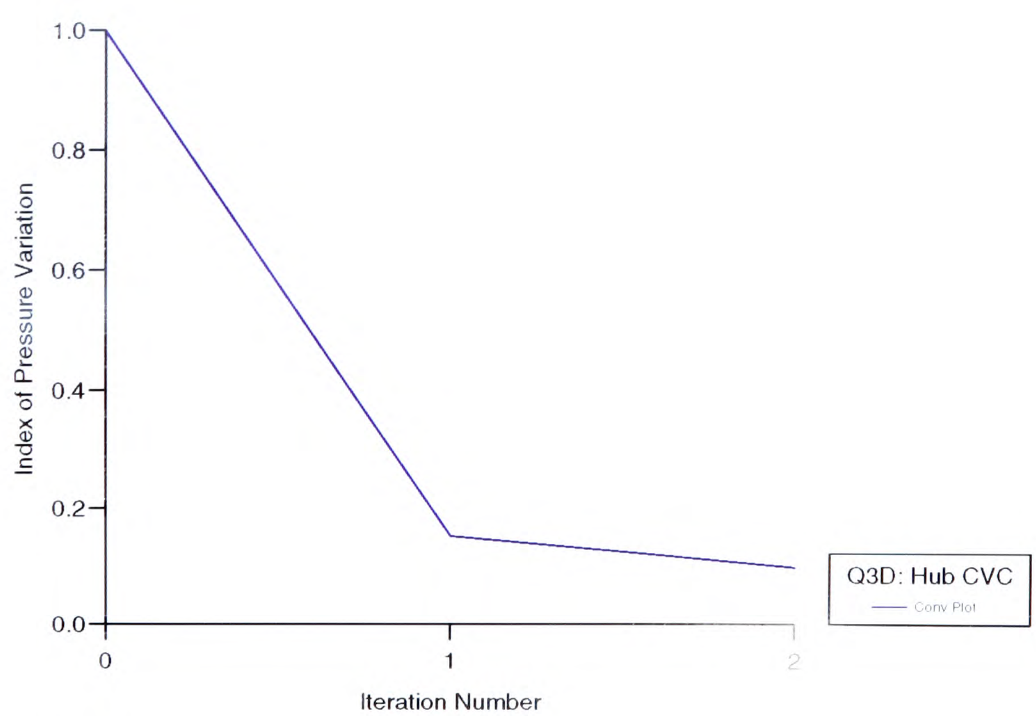

Figure 6.[illegible] Quasi-3D Design: History of pressure variation [illegible] co[illegible]y varying camber case.

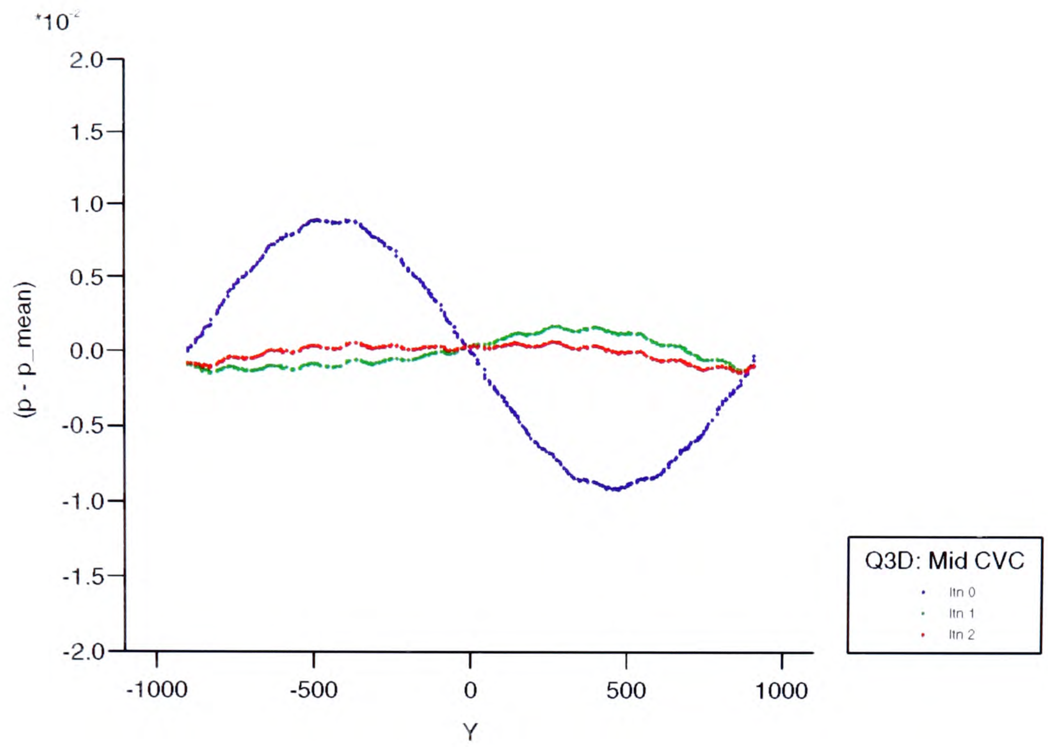

Figure 6.10: Quasi-3D Design: Circumferential pressure variation at **mid** for continuously varying camber case.

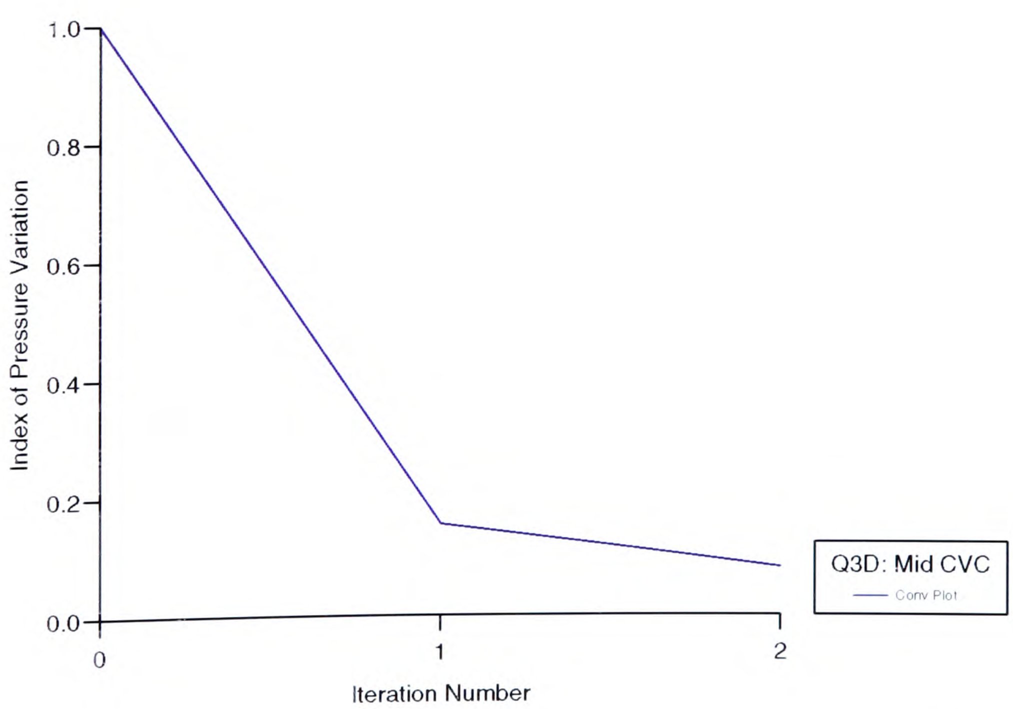

Figure 6.11: Quasi-3D Design: History of pressure variation at **mid** for the continuously varying camber case.

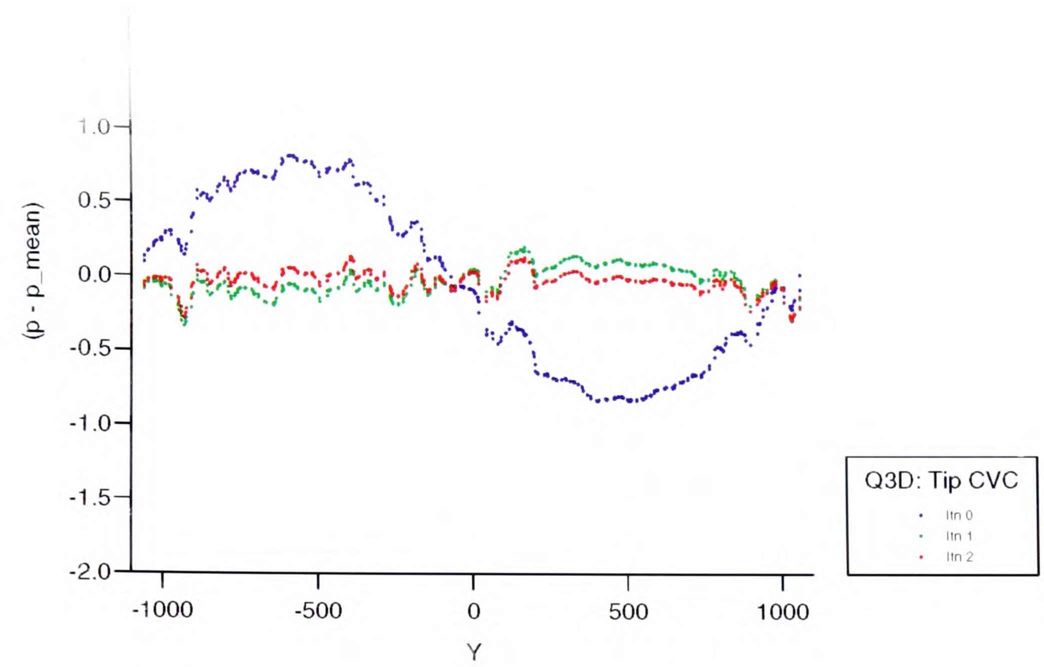

Figure 6.12: Quasi-3D Design: Circumferential pressure variation at **tip** for continuously varying camber case.

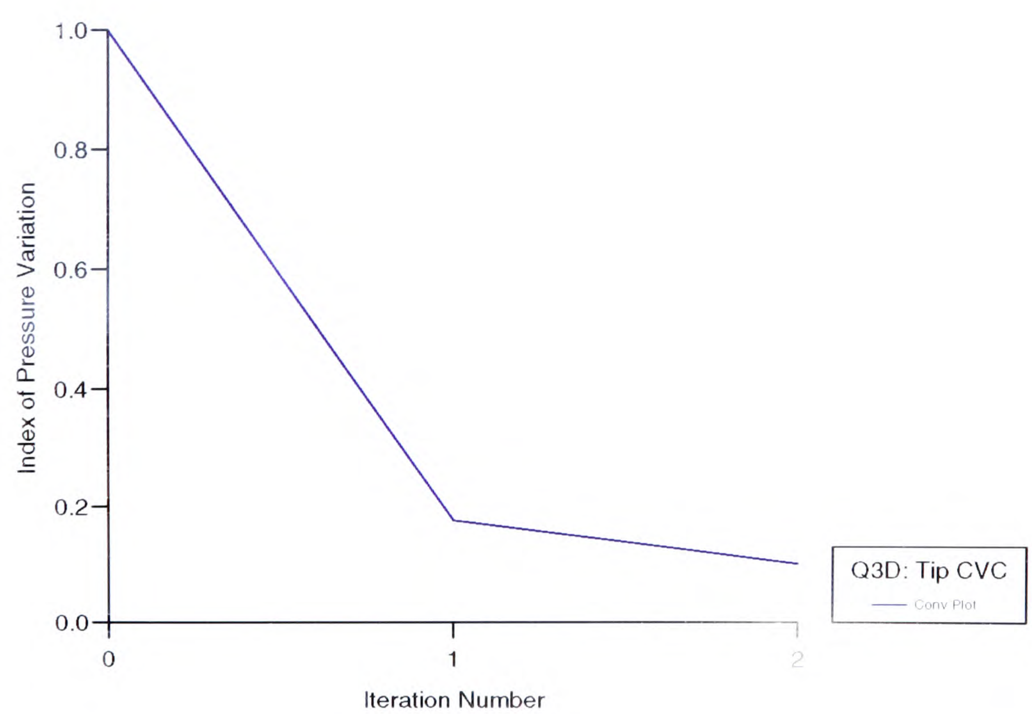

Figure 6.1[illegible]: Quasi-3D Design: History of pressure variation [illegible] con[illegible] varying camber case.

6.4.3 A 3D Design

The final design approach to be attempted is the fully three dimensional design approach. Here we use two design variables, C_{ch} and C_{ct} which are C_c at the hub and tip respectively. Based on the discussion in the preceding section, it is assumed that these are two independent design variables and a 2×2 system of equations has to be solved to determine the new design point. The design variable is assumed to have a linear variation from hub to tip. Pressure variations and convergence plots of the pressure deficit are presented in figures 6.14-6.19. The pressures in these figures are measured at the hub, mid and tip radial location respectively. In tables 6.2-6.3, the value of the pressure deficit integral is presented along side the absolute value of the design parameter (C_c). The present method has different values at the hub and tip radial locations, these values are presented under the hub and tip entries.

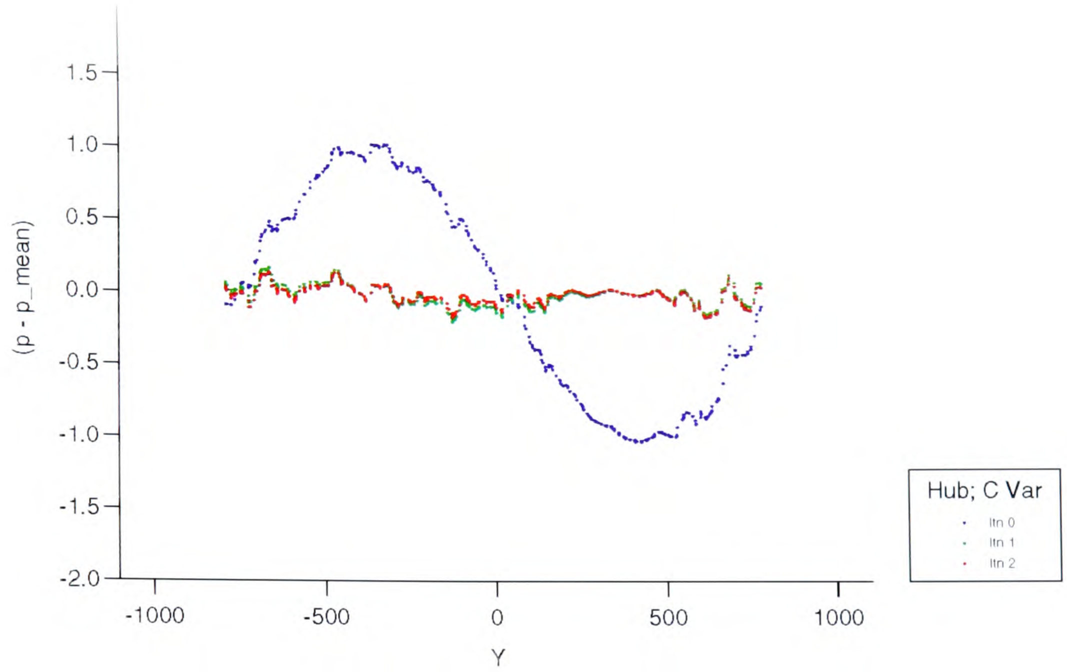

Figure 6.14: 3D Design: Circumferential pressure variation at **hub** for continuously varying camber case.

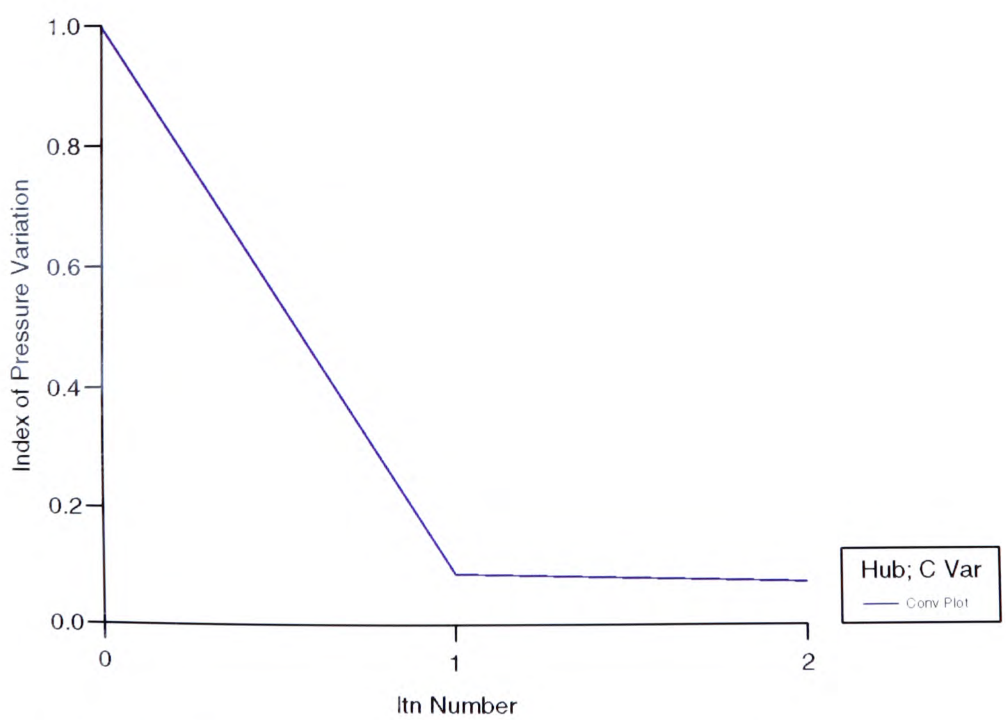

Figure 6.15: 3D Design: History of pressure variation at **hub** for the continuously varying camber case.

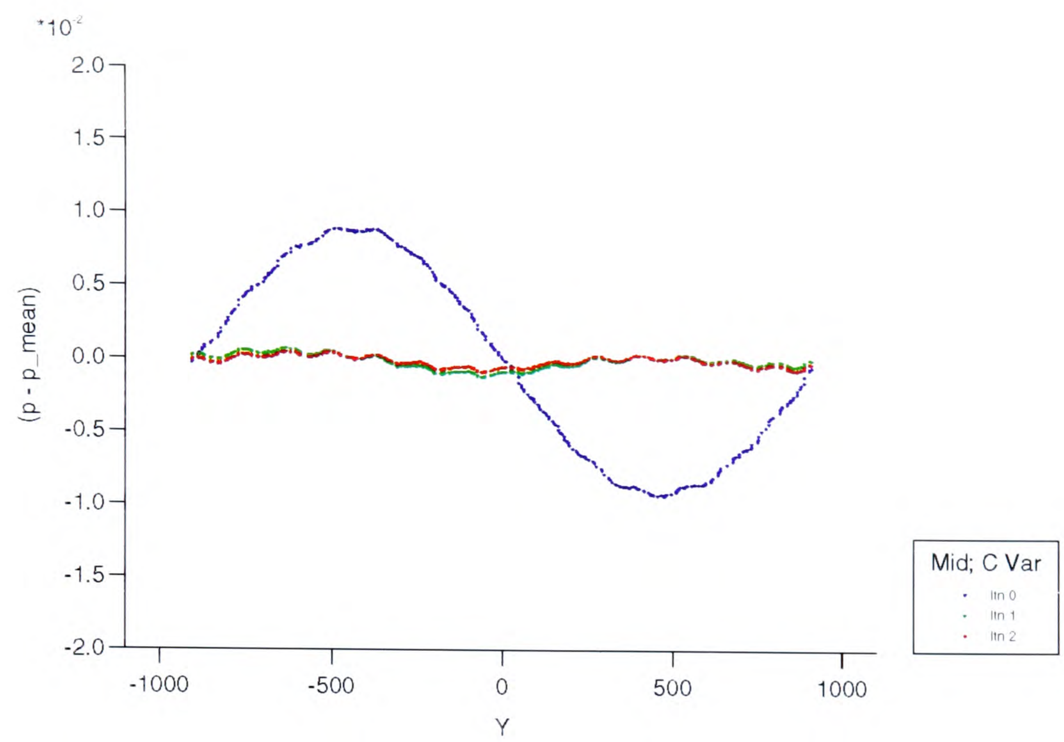

Figure 6.16: 3D Design: Circumferential pressure variation at **mid** for continuously varying camber case.

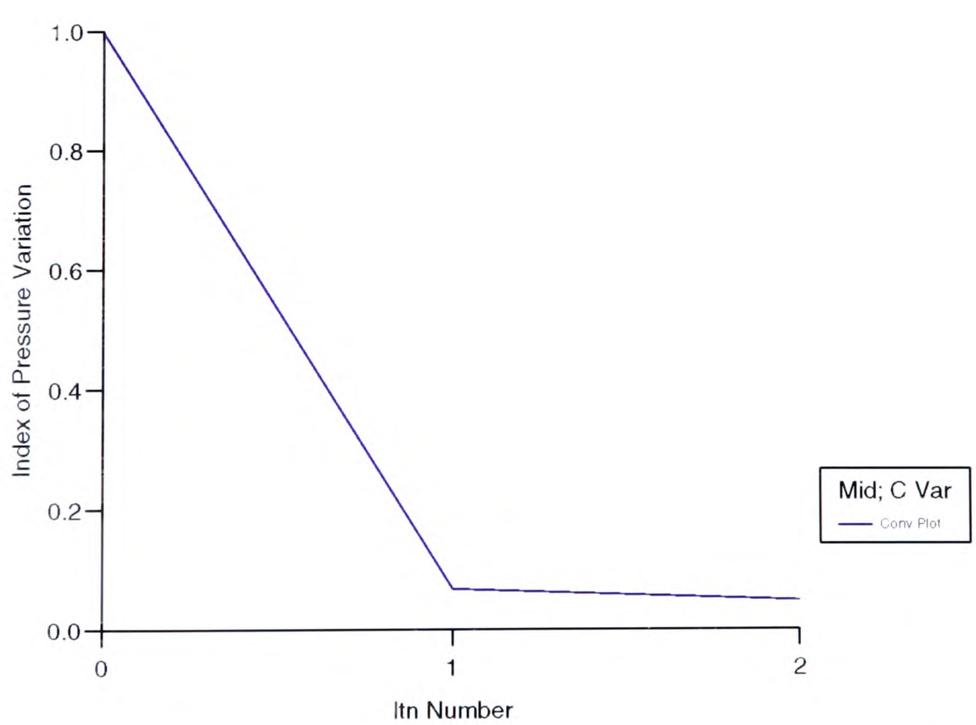

Figure 6.17: 3D Design: History of pressure variation at **mid** for the continuously varying camber case.

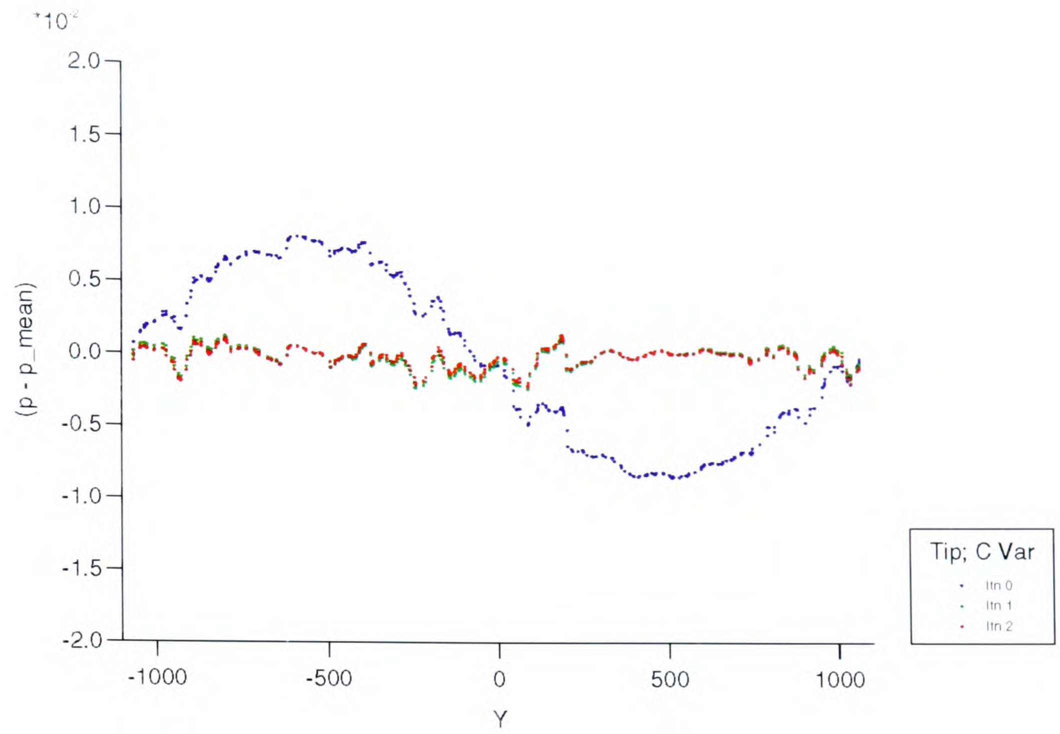

Figure 6.18: 3D Design: Circumferential pressure variation at **tip** for continuously varying camber case.

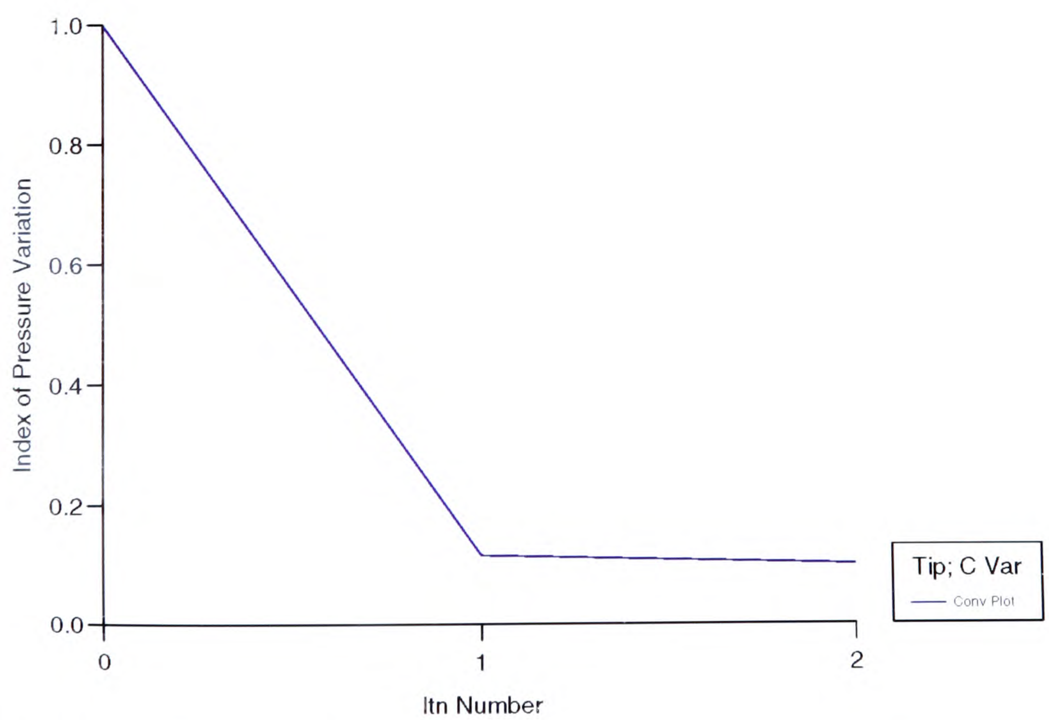

Figure 6.19: 3D Design: History of pressure variation at **tip** for the continuously varying camber case.

The limitations of a design that incorporates a unique blade for each position in the blade row has been discussed earlier in section 5.5.2. Thus, there is a need to have a reduced number of uniquely differing blades. As in the 2D case, we will attempt a redesign here that involves three different blade sets. One for datum, one for overturning and one for underturning. To further simplify the design process the magnitude of overturning will be equal to the underturning. This retains a design method with 2 design variables C_{ch} and C_{ct}. The grouping of the blades is identical to the 2D case and is presented in figure 5.15. Pressure variations and convergence plots of the pressure deficit are presented in figures 6.20-6.25. The pressures in these figures are measured at the hub, mid and tip radial location respectively. In tables 6.2-6.3, the value of the pressure deficit integral is presented along side the absolute value of the design parameter (C_c). The present method has different values at the hub and tip radial locations, these values are presented under the hub and tip entries.

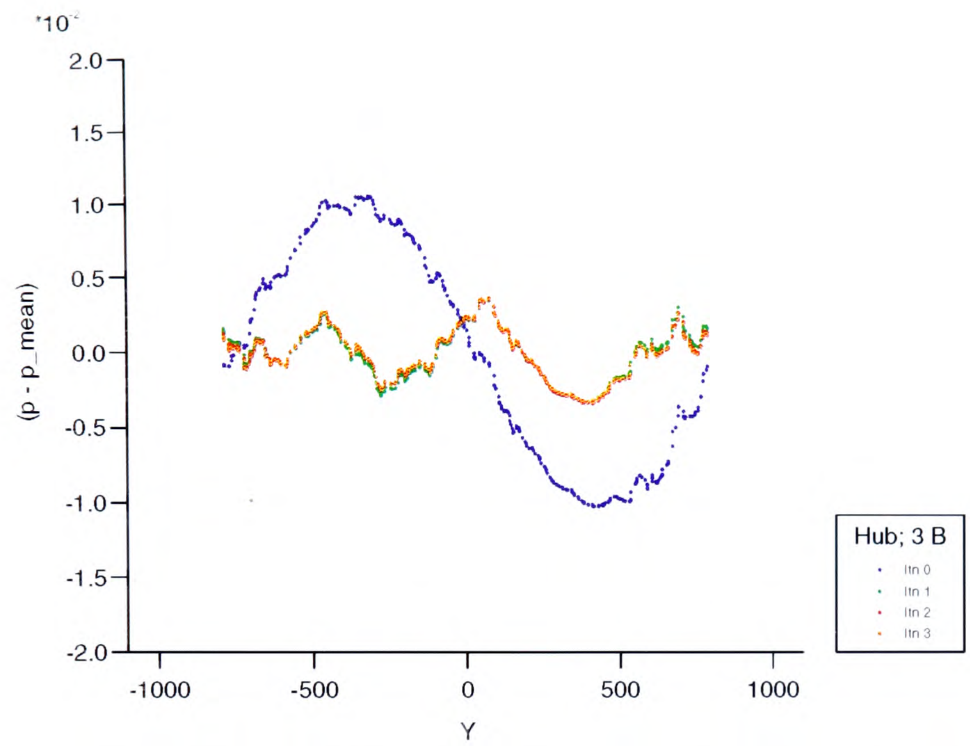

Figure 6.20: 3D Design: Circumferential pressure variation at **hub** for 3 blade case.

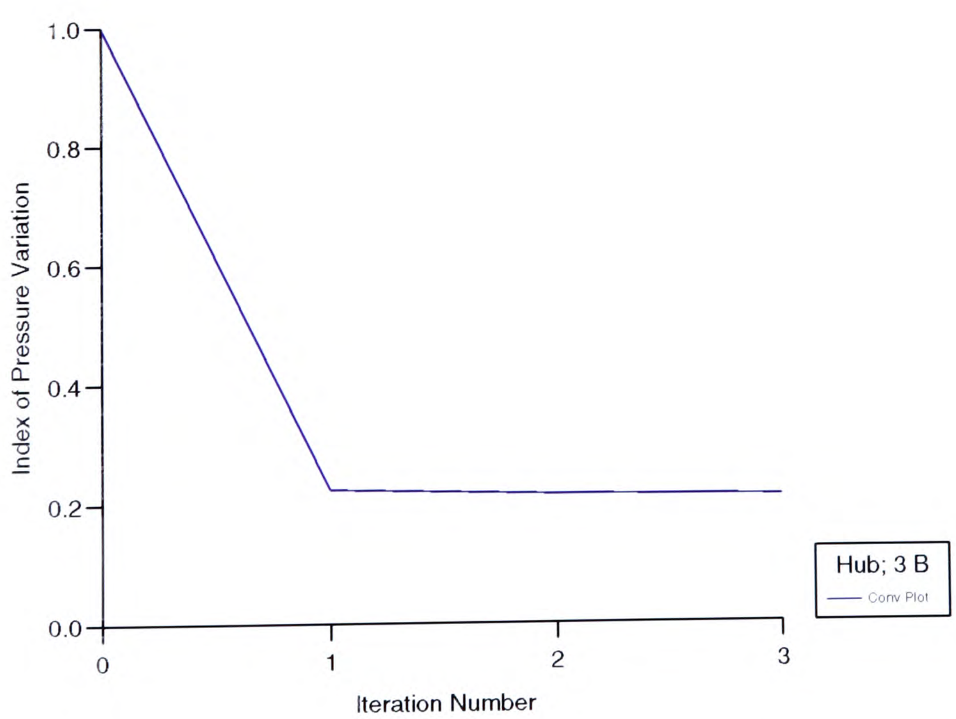

Fig… 6.21: 3D Design: History of pressure variation at **hub** for the 3 blade ca…

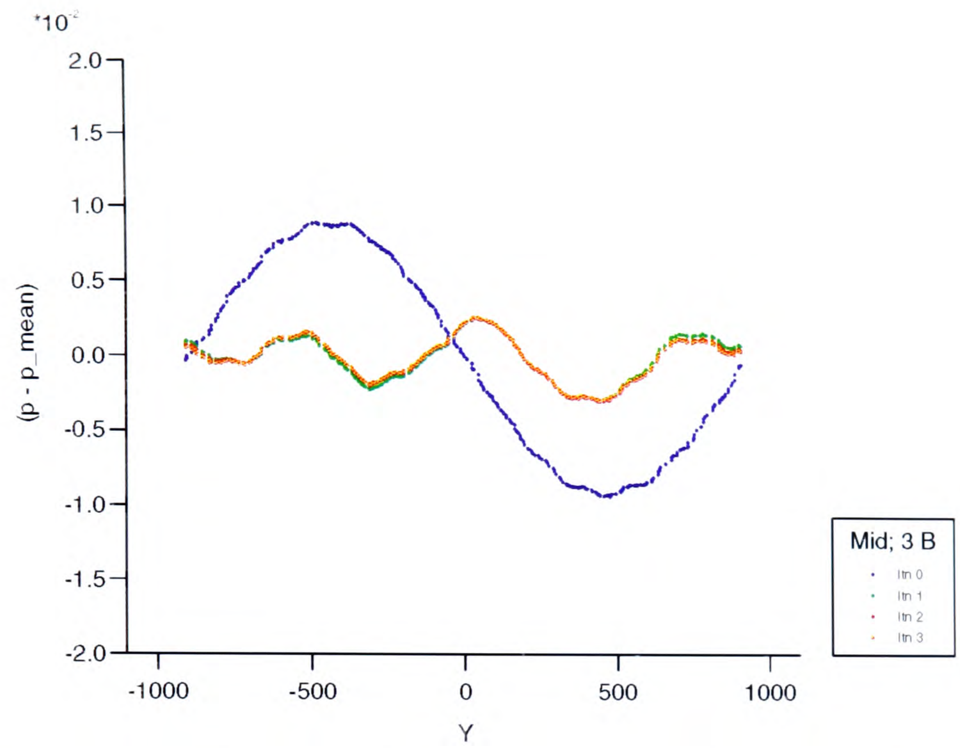

Figure 6.22: 3D Design: Circumferential pressure variation at **mid** for 3 blade case.

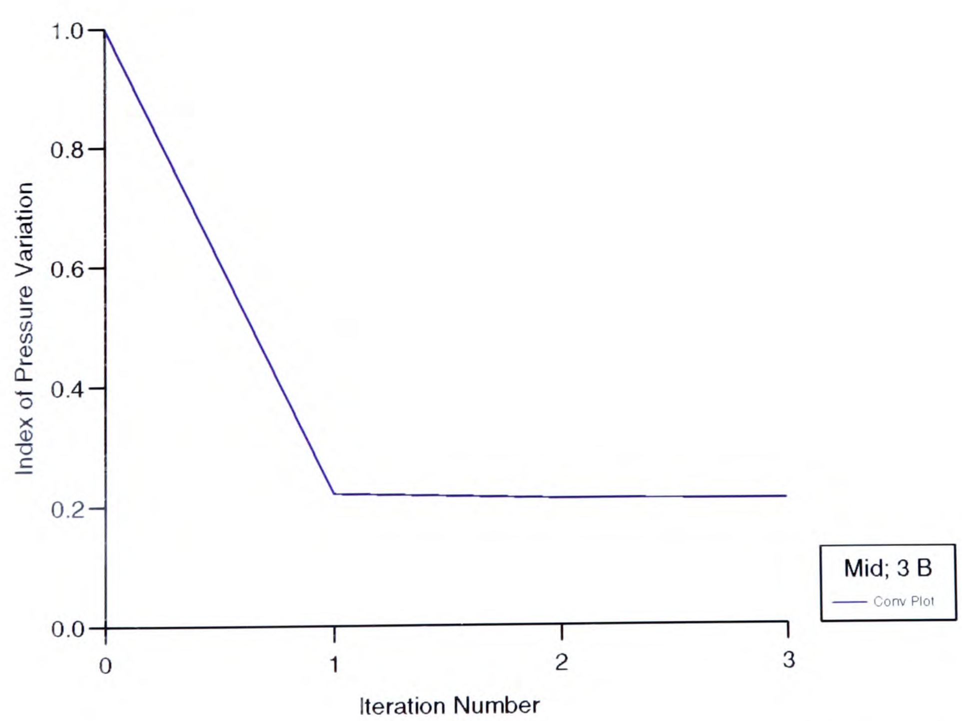

Figure 6.23: 3D Design: History of pressure variation at **mid** for the 3 blade cas

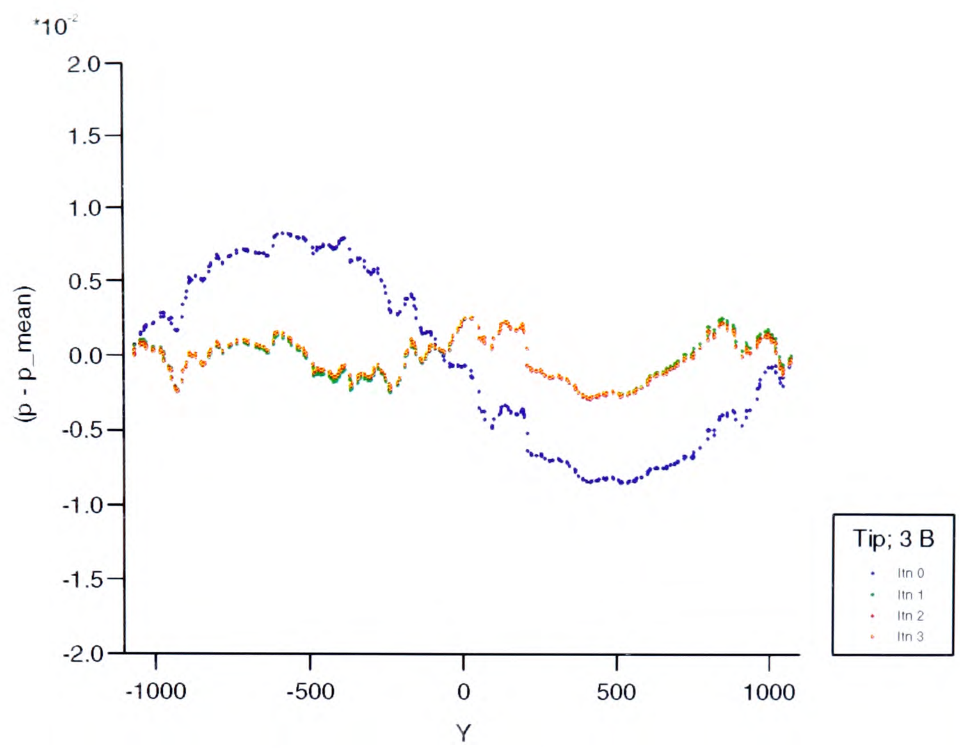

Figure 6.24: 3D Design: Circumferential pressure variation at **tip** for 3 blade case.

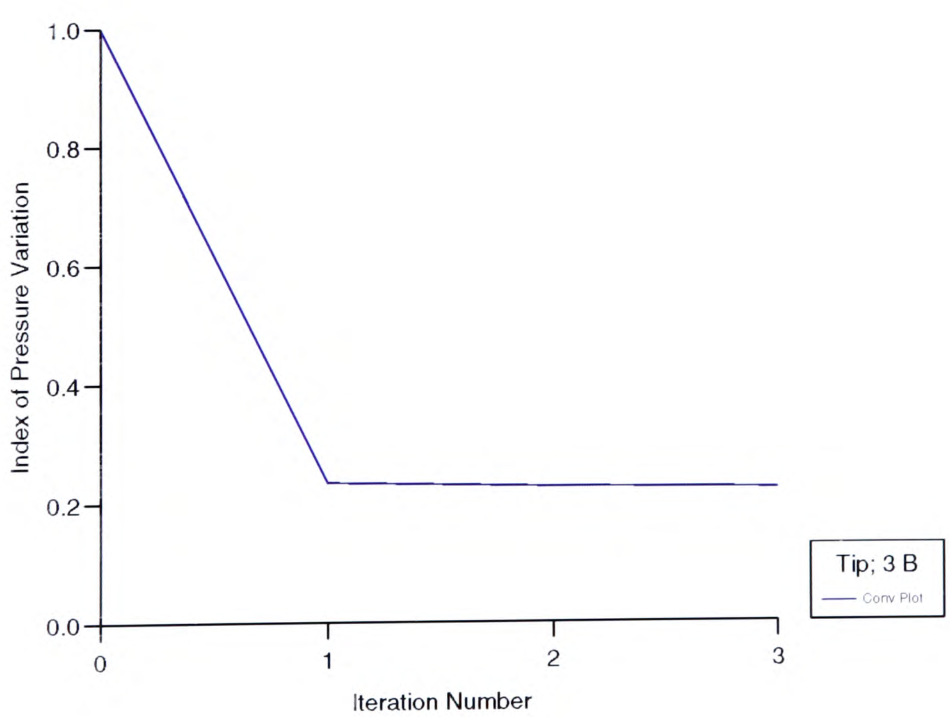

Figure 6.25: 3D Design: History of pressure variation at **tip** for the 3 blade case.

6.5 Concluding Remarks

Having presented numerical experiments with different approaches it is necessary now to compare and contrast these methods. Tables 6.2 (pg 115) and 6.3 (pg 116) present relevant design data for the different design approaches. Table 6.3 presents the magnitude of the design variable while table 6.2 presents the magnitude of the pressure integral. The aim of the redesign was to minimise this integral. Therefore the best design has the lowest pressure integral along the blade span (therefore, all three stations ie. hub, mid and tip, need to be considered).

Looking at table 6.3 it is evident that the 3D design method has produced "twisted" blades (the design variables for the hub and tip differ in sign). It is also notable that this leads to the lowest pressure integrals along the blade span. This can be interpreted as the success of the design method in tackling a three dimensional design problem. It indicates that the flow field was indeed three dimensional and thus needed a three dimensional design. However, the quasi-3D and the 2D approaches are not very far behind. Thus, it can be concluded that the three dimensionality of the flow field is small.

The design method discussed in this thesis is capable of performing 2D, quasi-3D and fully 3D redesign on the pylon-OGV problem. The computing time for the different methods is identical. However, the choice of approach used in an industrial framework is left to the designer. The choice could be influenced my many criterion including, manufacturing costs, which may prohibit the use of twisted blades, thus forcing the designer to rely on the 2D method. Otherwise, a full 3D approach is merited.

Chapter 7

Concluding Discussion

The main thrust of this thesis has been to identify issues that will influence the development of computational optimal design methods (CODM). CODM will increasingly dominate the industrial design environment and thus merits close scrutiny. The CFD community needs an understanding of these issues so that future developments (in CFD) are guided by an end aim of contributing to a CODM. Additionally, recent trends in CFD indicates a move towards 2D-3D inverse shape design by GB and NGB methods. However, in a comprehensive CODM there will remain a need for tailoring and redesign to alter existing shapes to match new design criteria. Some criteria can be externally imposed as geometric constraints in a shape design exercise, but constraints involving material properties are much harder to model. Further, unforeseen interactions may require tailoring to achieve target performance. It is in this realm that an optimisation driven design approach such as the one presented in this thesis will be crucial. Thus, in our view a comprehensive CODM will include the following subsystems:

- Inverse shape design methods,
- Robust and fast CFD analysis,
- GB and NGB Optimization driven redesign methods,
- Graphics user interface (GUI).

The course of design will be:

1 Basic shape design by inverse CFD methods,

2 Redesign/tailoring to suit individual requirements.

The redesign component of the CODM will be used most often over a broad range of problems and will involve considerable user interaction to allow an accurate specification of the design problem (cost function and constraints). Therefore, a suite of optimization methods and design tools are required to assist the designer.

GB methods in redesign can be divided into adjoint based and finite difference based methods. Finite difference based methods perform very well only for a small number of design variables. Cost functions in finite difference methods can be easily modified to suit the current design problem. Adjoint methods continue to perform very well even when a large number of design variables are used, but, altering cost functions is not trivial (it involves changing the boundary conditions of the code). Additionally, there are complexities in linearisation of such methods. In this thesis much emphasis has been laid on issues related to redesign. To make such a study tractable, a "typical" design problem was selected. The pylon-OGV-fan interaction (our test problem) is encountered sufficiently often to merit attention and is sufficiently well understood to serve as a test problem. Additionally, the basic shapes of the OGV's and pylon have already been defined to meet performance and structural requirements. The tailoring seeks to ameliorate interactions that were not anticipated during the shape design phase and achieve the initially specified performance. It should be emphasised here that the design method is independent of the flow solver (viscous or inviscid). The quasi-Newton method makes no assumption about the type of flow solution available and only seeks to evaluate the cost function at a particular location. The same can be said about other optimization driven methods. Two different approaches to design were evaluated on the test problem. This is in keeping with our aim to provide a suite of tools to tackle different design problems. Their merits, shortcomings and results are discussed in subsequent sections (7.2.1,7.2.2).

7.1 Basic Tools

There are many components to a CODM. They can be broadly categorised into:

Grid Generator The need for a robust and fast grid generator has always been appreciated. However, it is often the case that interfaces with grid generators leave a lot to be desired. Grid generators require two kinds of inputs, (a) the shape definition and (b) distribution of nodes. In most cases, shape definition is either obtained from a CAD package or an inverse shape design method and does not pose a problem. However, controlling the distribution of nodes in a grid can be a bottleneck. The grid generator determines internode distances at any point from the background grid and/or the strength of sources. The placement and strengths of such sources is crucial in determining the quality of the grid and success of the grid generation exercise. The interplay and influence of different sources is not very obvious in 3D and requires user "experience" and several attempts. This is clearly the bottleneck in a grid generation exercise. In our study, we resorted to generating 3D tetrahedral grids from a 2D triangular grid which simplified the entire grid generation process. This approach is feasible as long as the hub and tip configurations are similar. If the hub and tip configurations are very different (here "different" excludes changes in shape of components) then the grid generation will have to be performed by a regular 3D grid generator and will need much greater effort.

Flow Solver Robustness of a flow solver was found to be a very important criterion. From a CODM perspective the CFD code should not be too sensitive to numerical input parameters (dissipation, CFL number etc). CODMs will be hard to develop without such robust flow solvers. It is assumed that flow solvers make use of acceleration techniques and parallel processing to reduce the wall clock time taken for each run.

Grid Movement Method A crucial component of our design method has been the grid movement algorithm. The GMM has contributed to (a) grid generation and (b) implementing geometric perturbations on the datum grid. The ease of grid movement has made it possible to implement different geometric design modes. The GMM is an integral part of any optimization driven design system. In the present method, the GMM was used to implement the geometric perturbations and also during the evaluation of the gradients. In NGB optimization methods, GMM is used to alter the shapes before each flow solve. A robust, fast grid movement algorithm is essential for any CODM.

Graphic Interface A graphics interface is a future research topic. It should be possible to create a graphical front-end that interacts with the GMM, flow solver and optimization routines. Such a front-end should allow the user to alter the cost function and other parameters in the design run.

The graphics interface will also present the variation of the cost function with respect to the design variables and the history of the current design exercise. However, further work needs to be done on identifying the set of parameters to be presented to the designer. It is possible for a local redesign to lead to an overall degradation. The effect of any design change will have to be evaluated over a basket of parameters and should be available to the designer to judge the success of the current design exercise. This is necessary to avoid convoluted cost functions and constraints.

7.2 Gradient Based Design Methods

In the course of our work, we experimented with two different methods. Both these methods were based on widely available CFD techniques. Such an approach demonstrated the ease of developing CODMs and also avoided the need for long validation exercises (associated with new CFD methods). Experiences with two approaches are discussed here.

7.2.1 The Linear Approach

The linear approach involved using a linear perturbation Euler method to determine the sensitivity of upstream pressure to camber perturbations. This method is inviscid and can be applied to a limited class of problems. However, it can be very fast and useful in investigating new design concepts and obtaining approximate solutions.

One problem with the design procedure as applied in section 5.5 is that it generates a set of OGV's each of which is unique. This leads to unacceptable additional costs both in the manufacture of the OGV's and in the airlines' costs of maintaining stocks of spare parts. A practical compromise is to use a limited number of different OGV's; for example three, one with the datum exit flow angle, one with overturning and one with underturning. These can then be grouped and collectively designed to completely cancel the first circumferential harmonic of the pressure field generated by the pylon. The design can still be performed using the linear procedure (described in chapter 3). The OGV trailing edge flow angle is now a square wave function, corresponding to the different groups of blades. This square wave can be decomposed into a sum of circumferential harmonics, each of which can be analyzed separately with its own steady interblade phase angle. By linear superposition the results can then be combined to give the overall perturbation flow field. Linear scaling of the geometric perturbation will then lead to cancellation of the first harmonic of the upstream pressure perturbation. Additional harmonics can also be eliminated using a larger number of different blades. However, this may be unnecessary since these higher harmonics decay axially at a faster rate and so are less likely to adversely affect the fan.

The use of a linear perturbation code to determine sensitivities and redesign and OGV row was demonstrated. The redesign was successful in that it achieved more than 70% reduction in the static pressure variation that was exciting the fan. A feedback coupling between the pylon and OGV's was identified as the reason that even better reduction was not obtained.

7.2.2 The Non-Linear Approach

Redesign of the OGV row was performed using a quasi-Newton method. Here the sensitivities were evaluated by a finite difference procedure. The Newton method was used in a redesign involving (a) continuously varying camber and (b) a practical redesign using a limited number of different blades. Significant pressure reduction was achieved in both cases, indicating an acceptability in the industrial design process. Additionally, the same method was applied to a three dimensional problem with success. The present quasi-Newton method is seen to be very efficient for redesigns involving minimisation of a quadratic functional.

7.3 Suggestions for Future Work

GUI As discussed in section 7.1, the functionality of a Graphics User Interface (GUI) has to be carefully specified. Besides providing an easy-to-use front-end for the CODM, it should also provide tools to probe and analyze the entire flow field and retain a global perspective of the design and the associated costs.

Optimization Routines In the present thesis we used some of the simplest optimization methods. Of course, our study was also limited to simple cost functions. However, this may not be the case in many design exercises. For instance, in the OGV row, cost and structural reasons may require that different materials be used in the manufacture of different blades. For example all load-bearing OGV's could be metallic while non-load-bearing blades could be composites. To determine the blade-material combination one has to perform an optimization which seeks to minimise the total manufacturing cost of the blade row. However, this function is not "smooth" and a gradient based optimiser is inappropriate. A NGB method is required to determine the correct blade-material combination. Such problems that require NGB methods arise often in engineering design and necessitate the inclusion of NGB methods in the suite of optimisers made available to the designer. It will be at the designer's discretion to select the most appropriate optimiser for the problem. However, NGB methods can be expensive and further work needs to be performed to investigate how NGB methods and coarse grids can be coupled to reduce the CPU time. It might also be possible to link NGB-GB methods to achieve maximum performance for some design applications. Here, the NGB method is used to determine the region of the minimum while the GB method performs the final descent. Additionally, an attempt to develop and incorporate an adjoint based method to determine sensitivities in the present flow code is desirable.

An Integrated Approach In developing an integrated approach one has to link together inverse design methods and redesign methods in a CODM. The inverse shape design tool has to be made available to the designer throughout the design process. It is possible that a new shape design might be preferable to extensive tailoring. While the concept is fairly straight forward, the actual implementation needs some attention to ensure that grid formats, flow parameters and non-dimensionalisations are consistent across these different computational methods.

References

[1] S. Aly, F. Marconi, M. Ogot, R. Pelz, and M. Siclari. Stochastic Optimization Applied to CFD Shape Design. AIAA paper 95-1647-CP, 1995. Presented at the 12th AIAA Conference on Computational Fluid Dynamics, San Diego, CA. 1995.

[2] T. J. Barber and H. D. Weingold. Vibratory Forcing Functions Produced by Nonuniform Cascades. *ASME Journal of Turbomachinery*, 100(77-GT-57):82–88, January 1978.

[3] J. T. Batina. Unsteady Euler Algorithm with Unstructured Dynamic Mesh for Complex-Aircraft Aerodynamic Analysis. *AIAA Journal*, 29(3):327–333, 1991.

[4] O. Baysal and M. E. Eleshaky. Aerodynamic Design Optimization Using Sensitivity Analysis and Computational Fluid Dynamics. *AIAA Journal*, 30(3):718–725, 1992.

[5] M. O. Bristeau, O Pironneau, R. Glowinski, J. Periaux, P. Perrier, and G. Poirier. On the Numerical Solution of Nonlinear Problems in Fluid Dynamics by Least Squares and Finite Element Methods (II). Application to Transonic Flow Simulations. In *Proceedings-3rd International Conference on Finite Elements in Nonlinear Mechanics, FENOMECH 84, Stuttgart, Germany, 1984. Ed: J. St. Doltsinis*, 1985.

[6] D. A. Burgess, P. I. Crumpton, and M. B. Giles. A Parallel Framework for Unstructured Grid Solvers. In *Proceedings of the Second European Computational Fluid Dynamics Conference, September 1994, Stuttgart, Germany. Ed: S. Wagner et al*, 1994.

[7] R. L. Campbell. An Approach To Constrained Aerodynamic Design With Application To Airfoils. NASA TP 3260, 1992.

[8] R. L. Campbell and L. A. Smith. A Hybrid Algorithm for Transonic Airfoil and Wing Design, 1987. AIAA paper 87-2552, also published in "A Collection of Technical Papers–AIAA 5th Applied Aerodynamics Conference".

[9] R. L. Campbell and L. A. Smith. Design of Transonic Airfoils and Wings Using a Hybrid Design Algorithm, 1987. SAE Tech Paper 871756.

[10] G. Cerri and W. F. O'Brien. Sensitivity Analysis and Optimum Design Method for Reduced Rotor-Stator-Strut Flow Interaction. *ASME Journal of Turbomachinery*, 111(88-GT-310):401–408, October 1989.

[11] H. Cohen, G.F.C Rogers, and H.I.H Saravanamuttoo. Gas Turbine Theory. Longman Scientific & Technical, 1972.

[12] P. I. Crumpton. An Efficient Cell Vertex Method for Unstructured Tetrahedral Grids. Technical Report 95/19, Numerical Analysis Group, Oxford University Computing Laboratory, Oxford OX1 3QD, England, October 1995. Presented at the ICFD Conference, 1995.

[13] P. I. Crumpton and M. B. Giles. Aircraft Computations Using Multigrid and an Unstructured Parallel Library. AIAA Paper 95–0210, 1995.

[14] P. I. Crumpton and M. B. Giles. Implicit Time Accurate Solutions on Unstructured Dynamic Grids. 12th AIAA Conference on Computational Fluid Dynamics 1995, San Diego, CA. AIAA Paper 95–1671, 1995.

[15] M Drela. Viscous and Inviscid Schemes Using Newton's Method. In *Special Course on Inverse Methods for Airfoil Design for Aeronautical and Turbomachinery Applications.* AGARD Report No. 780, 1990.

[16] M. Drela. Design and Optimization Method for Multi-Element Airfoils. In *Aerospace Design Conference, Irvine, CA*, February 16-19 1993. AIAA 93-0969.

[17] M. Drela and M.B. Giles. ISES: A Two-Dimensional Viscous Aerodynamic Design and Analysis Code, Jan 1987. AIAA-87-0424.

[18] O. E. Ed: Lancaster. Jet Propulsion Engines. Oxford University Press, London, 1959. Volume XII of High Speed Aerodynamics and Jet Propulsion Series.

[19] MPI Forum. MPI: A Message-Passing Interface MPI Forum. Technical Report CS/E 94-013, Department of Computer Science, Oregon Graduate Institute, March 94.

[20] A. Geist, A. Beguelin, J. Dongarra, W. Jiang, R. Mancheck, and V. Sunderam. PVM 3 User's Guide and Reference Manual, 1994.

[21] M. B. Giles. Calculation of Unsteady Wake/Rotor Interaction. *AIAA Journal of Propulsion and Power*, 4(4):356–362, July/August 1988.

[22] M. B. Giles. Non-Reflecting Boundary Conditions for Euler Equations. Technical Report 88-1, MIT Computational Fluid Dynamics Laboratory, 1988.

[23] M. B. Giles. UNSFLO: A Numerical Method for the Calculation of Unsteady Flows in Turbomachinery. Technical Report GTL-Report #205, Gas Turbine Laboratory, MIT Mass., May 1991.

[24] M. B. Giles. An Approach for Multi-Stage Calculations Incorporating Unsteadiness. ASME paper 92-GT-282, 1992. Presented at the International Gas Turbine and Aeroengine Congress and Exposition, Cologne, Germany.

[25] M. B. Giles, M. Drela, and W.T. Thompkins. Newton Solution of Direct and Inverse Transonic Euler Equations. In *AIAA 7th Computational Fluid Dynamics Conference*. Cincinnati, Ohio, July 1985. AIAA paper 85-1530.

[26] M. B. Giles and Haimes R. Validation of a Numerical Method for Unsteady Flow Calculations. *ASME Journal of Turbomachinery*, 115(91-GT-271):110–117, January 1993.

[27] M. B. Giles and R. R. Haimes. Advanced Interactive Visualisation for CFD. *Computing Systems in Engineering*, 1(1), 1990.

[28] S. Goel and S. Lamson. Automating the Design Process for 3D Turbine Blades. In *CFD for Design and Optimization Published by ASME as FED-Vol 232, Ed: O. Baysal*, 1995.

[29] D. E. Goldberg. GENETIC ALGORITHMS in Search Optimization and Machine Learning. Addison-Wesley Publishing Company Inc., 1989.

[30] Y. Gong and R. Cai. 3D Mean-Stream-Line Method–A New Engineering Approach to the Inverse Problem of 3D Cascade. ASME paper 89-GT-48 presented at the Gas Turbine and Aeroengine Congress and Exposition, Toronto, Canada, June 4-8, 1989.

[31] E. Greff, K. Becker, M. Karwin, and S. Rill. Integration of High Bypass Ratio Engines on Modern Transonic Wings for Regional Aircraft. *Aeronautical Journal*, pages 1–13, January 1993.

[32] C. Gu and Y. Miao. Blade Design of Axial-Flow Compressors by the Method of Optimal Control Theory – Application of Pontryagin's Maximum Principles, a Sample Calculation and its Results. ASME paper 86-GT-182 presented at the 31st International Gas Turbine Conference and Exhibition, Dusseldorf, Germany, June, 1986.

[33] C. Gu and Y. Miao. Blade Design of Axial-Flow Compressors by the Method of Optimal Control Theory - Physical Model and Mathematical Expression. ASME paper 86-GT-183 presented at the 31^{st} International Gas Turbine Conference and Exhibition, Dusseldorf, Germany, June, 1986.

[34] R. Haimes. pV3: A distributed System for Large Scale Unsteady CFD Visualisation. AIAA paper 94-0321, 1994.

[35] R. Haimes. Concurrent Distributed Visualisation and Solution Steering. In *Proceedings of Parallel CFD 95*, September 1995.

[36] R. Haimes and M. B. Giles. VISUAL3: Interactive Unsteady Unstructured 3D Visualisation. AIAA paper 91-0794, 1991.

[37] K. C. Hall and E. F. Crawley. Calculation of Unsteady Flows in Turbomachinery using Linearized Euler Equations. *AIAA Journal*, 27(6):777–787, June 1989.

[38] J. H. Holland. Genetic Algorithms and the Optimal Allocations of Trials. *SIAM Journal of Computing*, 2(2):88–105, 1973.

[39] W. P. Huffman, R. G. Melvin, D. P. Young, F. T. Johnson, J. E. Bussoletti, M. B. Bieterman, and C. L. Hilmes. Practical Design and Optimization in Computational Fluid Dynamics. AIAA paper 93-3111, 1993. Presented at the AIAA 24th Fluid Dynamics Conference, Orlando, Florida.

[40] A. Jameson. Aerodynamic Design via Control Theory. *Journal of Scientific Computing*, 3:233–260, 1988.

[41] A. Jameson. Optimum Aerodynamic Design Using CFD and Control Theory. AIAA paper 95-1729-CP, 1995. Presented at the 12th AIAA Conference on Computational Fluid Dynamics, San Diego, CA. 1995.

[42] A. Jameson. Automatic Design of Transonic Airfoils to Reduce the Shock Induced Pressure Drag. In *31st Israel Annual Conference on Aviation and Aeronautics*, Feb 21-22, 1990.

[43] I. K. Jennions and P. Stow. A Quasi Three-Dimensional Turbomachinery Blade Design System. Part II - Computerised System. ASME 84-GT-27, 1984.

[44] I. K. Jennions and P. Stow. A Quasi Three-Dimensional Turbomachinery Blade Design System. Part I - Through Flow Analysis. ASME 84-GT-26, 1984.

[45] W. Joo. Intake/Engine Flowfield Coupling in Turbofan Engines, April 1994. PhD Thesis, University of Cambridge.

[46] T. R. Kingston. Internal Report, 1995. Rolls-Royce.

[47] H. Kodama. Performance of Axial Compressor With Nonuniform Exit Static Pressure. *ASME Journal of Turbomachinery*, 108(85-IGT-43):76–81, July 1986.

[48] H. Kodama and S. Nagano. Potential Pressure Field by Stator/Downstream Strut Interaction. *ASME Journal of Turbomachinery*, 111(88-GT-54):197–203, April 1989.

[49] G. Kuruvila, S. Ta'asan, and M.D. Salas. Airfoil Design and Optimization. AIAA paper 95-0478, 1995. Presented at the 33rd Aerospace Sciences Meeting and Exhibit, Reno, January 1995.

[50] J. C. Lewis, G. P. Peters, and R. K. Agarwal. Airfoil Design via Control Theory using Euler Equations. In *Proceedings of the 1991 ASME Winter Annual Meeting, Atlanta, in ASME FED - Vol 129, December,*, 1991.

[51] W.F. Lin, A.W. Chen, and E.N. Tinoco. 3D Transonic Nacelle and Winglet Design. AIAA paper 90-3064. also published in "A Collection of Technical Papers", Part 2–AIAA 8th Applied Aerodynamics Conference, pp 582-591, 1990.

[52] D. R. Lindquist and M. B. Giles. Generation and use of unstructured grids for turbomachinery, April 1990. Proceedings of Computational Fluid Dynamics Symposium on Aeropropulsion, NASA CP-10045.

[53] D. R. Lindquist and M. B. Giles. On the validity of linearized unsteady Euler equations with Shock Capturing, 1991. AIAA Paper 91-1958.

[54] J.B. Malone, J.C. Narramore, and L.N. Sankar. An Efficient Airfoil Design Method Using the Navier-Stokes Equation. In *Computational Methods for Aerodynamic Design(Inverse) and Optimization.* AGARD CP 463, 1990.

[55] D. J. Mavriplis. Three-Dimensional Unstructured Multigrid for the Euler Equations. *AIAA Journal*, 30(7):1753–1761, 1992.

[56] R. Miller and J. Reed. The Oxford BSP Library Users' Guide, version 1.0, 1993.

[57] R. H. Ni. A Multiple Grid Scheme for Solving the Euler Equations . *AIAA Journal*, 20:1565–1571, 1982.

[58] R. H. Ni and F. Sisto. Numerical Computation of Nonstationary Aerodynamics of Flat Plate Cascades in Compressible Flow. ASME paper 75-GT-5, 1975.

[59] J. Peraire, J. Peiro, and K. Morgan. Finite Element Multigrid Solution of Euler Flows Past Installed Aero-Engines. *Computational Mechanics*, 11:433-451, 1993.

[60] O. Pironneau. Optimal Shape Design for Elliptic Systems. Springer Verlag, New York, 1984.

[61] D. P. Raymer. Aircraft Design - A Conceptual Approach. AIAA.

[62] Rolls-Royce. The Jet Engine. Rolls-Royce, Derby, 1986.

[63] P. Rubbert and M. Goldhammer. CFD in Design: An Airframe Perspective. AIAA paper 89-0092, Presented at the 27th Aerospace Sciences Meeting, Reno, Nevada, USA. January 1989.

[64] Kirkpatrick S., C. D. Gelatt, and M. P. Vecchi. Optimization by Simulated Annealing. *Science*, 220(4598):671–680, 1983.

[65] C. T. Savell and W. R. Wells. Rotor Design to Attenuate Flow Distortion: Part 1 – A Semiactuator Disc Analysis. *ASME Journal of Engineering for Power*, 97, Jan 1975.

[66] C.T. Savell and W.R. Wells. Rotor Design to Attenuate Flow Distortion: Part I – A Semi Actuator Disk Analysis. *ASME Journal of Engineering for Power*, 97, Jan 1975.

[67] B.S. Seidel, M.D. Matawey, and J.J. Adamczyk. Inlet Flow Distortions in Turbomachinery. *ASME Journal for Engineering for Power*, 102, Oct 1980.

[68] L.A. Smith and R.L. Campbell. A Method for the Design of Transonic Flexible Wings. NASA TP-3045, 1990.

[69] P. Stow. Navier-Stokes Methods Applied to Turbomachinery Blade Design. Rolls-Royce Report TSG0447, 1989. Presented at the IX ISABE Conference, Athens, September 4-9, 1989.

[70] A. Suddhoo. By Personal Communication, May 1992.

[71] S. Ta'asan. Trends in Aerodynamics Design and Optimization: A Mathematical Viewpoint. AIAA paper 95-1731-CP, 1995. Presented at the 12th AIAA Conference on Computational Fluid Dynamics, San Diego, CA. 1995.

[72] Y. Tanida. Inlet Distortion and Blade Vibration in Turbomachinery. In *International Symposium on Air Breathing Engines*, March, 1974.

[73] E. Torenbeek. Synthesis of Subsonic Airplane Design. Delft University Press, Delft, 1988.

[74] J. A. Van Egmond. Numerical Optimization of Target Pressure Distributions for Subsonic and Transonic Airfoil Design. In *Computational Methods for Aerodynamic Design(Inverse) and Optimization.* AGARD-CP-463, 1990.

[75] N. P. Weatherill and O. Hassan. Efficient Three-Dimensional Grid Generation using the Delauney Triangulation. In *Proceedings of the First European Computational Fluid Dynamics Conference, Brussels, Ed. Ch. Hirsch,* September 1992.

[76] Y.S. Wie, F.S. Collier, and R.D. Wagner. Application of Laminar Flow Control to High-Bypass-Ratio Turbofan Engine Nacelles, 1991. SAE Technical Paper 912114.

[77] C. Wu and C.A. Brown. A Theory of the Direct and Inverse Problems of Compressible Flow Past Cascade of Arbitrary Airfoils. *J.A.S.*, 19(3):183–196, March 1952.

[78] Z. Xiaolu and Q Lisen. An Approximate 3-D Aerodynamic Design Method of Centrifugal Impeller Blades. ASME paper 89-GT-73 presented at the Gas Turbine and Aeroengine Congress and Exposition, Toronto, Canada, June 4-8, 1989.

[79] D. P. Young, W. P. Huffman, R. G. Melvin, M. B. Bieterman, C. L. Hilmes, and F. T. Johnson. Inexactness and Global Convergence in Design Optimization. AIAA paper 94-4386, 1994. Presented at the 5th AIAA/NASA/USAF/ISSMO Symposium on Multidisciplinary Analysis and Optimisation, Panama City Beach, Florida.

[80] W. Zhengming. A Method of Aerodynamic Design of Blades in Quasi-Three-Dimensional Calculation of Turbomachine. ASME paper 86-GT-192 Presented at the International Gas Turbine Conference and Exhibit, Dusseldorf, W. Germany, June 8-12, 1986.